

**CONTINUOUS IRRADIATIONS IN PROTON THERAPY:
BALANCING RISKS AND BENEFITS**

Grischa Klimpki

DISS. ETH NO. 25078

**CONTINUOUS IRRADIATIONS IN PROTON THERAPY:
BALANCING RISKS AND BENEFITS**

A thesis submitted to attain the degree of
DOCTOR OF SCIENCES of ETH ZURICH
(Dr. sc. ETH Zurich)

presented by
GRISCHA MORITZ KLIMPKI

M.Sc. University of Heidelberg

born on 28.05.1989

citizen of Germany

accepted on the recommendation of

Prof. Dr. Antony Lomax
Prof. Dr. Klaus Kirch
Prof. Dr. Oliver Jäkel

2018

Grischa Klimpki

Continuous irradiations in proton therapy: balancing risks and benefits

© 2018

DOI: 10.3929/ethz-b-000258251

Acknowledgments

I would like to thank Prof. Weber for giving me the opportunity to carry out my dissertation at the PSI Center for Proton Therapy. He prioritized the line scanning project and provided the required resources, for which I am very grateful. I also wish to thank my academic supervisor, Prof. Lomax. I highly appreciate his encouraging support, which always helped to improve the quality of my scientific work, and I sincerely hope to have adopted some of his outstanding teaching and presentation skills. Furthermore, I thank Prof. Kirch and Prof. Jäkel for co-examining this dissertation and carefully questioning the findings of this thesis.

I am particularly grateful to my technical supervisor Dr. Meer, who opened the door to the technology behind proton therapy. I value how he guided me through the past years without ever compromising the space for exploration and development beyond the scope of this project. It was a great pleasure to be part of the line scanning team lead by Dr. Psoroulas. I wish to acknowledge their dedication to and motivation for the project. All implementations mentioned in this thesis were only possible because of the help of very knowledgeable software and electronics engineers. I wish to extend my gratitude to Dr. Pedroni and all technical experts for their work on the Gantry 2 beamline and to Dr. Schippers and his group for improvements on the accelerator side.

Last but not least, I wish to express my sincere gratitude to the Giuliana and Giorgio Stefanini Foundation for creating the prerequisites for an independent and successful dissertation. The foundation promotes projects in cancer research, visual arts and classical music. I feel honored and privileged to have been supported by them.

Grischa Klimpki

Villigen PSI | April 2018

CONTENTS

1	Introduction	1
1.1	The advantages of proton beam therapy	3
1.2	The pencil beam scanning technique	4
1.3	The problem of organ motion	5
1.4	The multitude of solutions to organ motion	6
1.5	The need for fast, dynamic scanning and dedicated safety measures	10
1.6	The scope and role of this thesis	11
2	Materials and methods	15
2.1	The Gantry 2 pencil beam scanning system at PSI	16
2.1.1	Actuators	17
2.1.2	Detectors	18
2.1.3	Variants of pencil beam scanning	20
2.2	Treatment plan conversion	23
2.3	The CCD imaging system	27
2.3.1	Geometric distortions	27
2.3.2	Intensity distortions	28
2.3.3	Quenching correction	29
2.4	Data acquisition and analysis	31
2.4.1	Experimental setup	31
2.4.2	Data analysis tools	32
3	A beam monitoring and validation system for line scanning	33
3.1	Introduction	35
3.2	Materials and methods	36
3.2.1	Beam delivery modes	36
3.2.2	Beam monitoring requirements	37
3.2.3	Gantry 2 beam monitors	39
3.2.4	Line profile prediction	41
3.2.5	Metrics for line profile comparison	44
3.2.6	Dose measurements at iso-center	45

3.3	Experiments and results	45
3.3.1	Safety level 1	45
3.3.2	Safety level 2	47
3.4	Discussion and outlook	50
3.5	Conclusion	53
4	Real-time beam monitoring in scanned proton therapy	55
4.1	Introduction	57
4.2	Materials and methods	58
4.2.1	Proton therapy beamline	58
4.2.2	Beam delivery and monitoring	59
4.2.3	Control software	61
4.2.4	FPGA firmware of the monitoring system	62
4.2.5	Gantry 2 test system	64
4.2.6	Verifying software and firmware enhancements	65
4.3	Experiments and results	65
4.3.1	Logging functionality	65
4.3.2	Error in beam position	66
4.3.3	Error in instantaneous beam current	67
4.3.4	Error in integrated beam current	68
4.4	Discussion and conclusion	69
5	Safety tolerances for real-time beam monitoring	73
5.1	Introduction	75
5.2	Derivation of safety tolerances	76
5.2.1	Definition of erroneous delivery	76
5.2.2	Maximum dose deposition of a proton beam	77
5.2.3	Tolerance for dose deposition	79
5.2.4	Tolerances for instantaneous beam current	80
5.2.5	Tolerance for beam position	80
5.3	Discussion of safety tolerances	81
5.3.1	Definition of erroneous delivery	82
5.3.2	Maximum dose deposition of a proton beam	82
5.3.3	Tolerance for dose deposition	82
5.3.4	Tolerance for instantaneous beam current	82
5.3.5	Tolerance for beam position	83
5.4	Conclusion	83
6	The impact of PBS techniques on rescanning moving targets	85
6.1	Introduction	87
6.2	Materials and methods	88
6.2.1	Beam delivery techniques	88
6.2.2	Patient cases and treatment plans	89
6.2.3	Rescanning strategy	90

6.2.4	Treatment plan conversion	91
6.2.5	4D dose calculation	92
6.2.6	Measurement devices and setup	94
6.2.7	Quantification metrics	94
6.3	Experiments and results	94
6.3.1	Experimental validation of the timing model	95
6.3.2	Experimental validation of the plan converter	95
6.3.3	Experimental validation of the 4D dose calculation engine . .	96
6.3.4	Results of 4D dose calculations	96
6.3.5	Experimental validation of effectiveness and efficiency	99
6.4	Discussion and outlook	101
6.5	Conclusions	103
7	Discussion and outlook	105
7.1	Overall results	105
7.1.1	The design of a beam monitoring system	105
7.1.2	The hardware and firmware implementations	107
7.1.3	The compliance with safety regulations	108
7.1.4	The application of line scanning in the context of moving target treatments	110
7.2	Strengths and weaknesses of the underlying methods	111
7.2.1	The choice of beam monitors	111
7.2.2	The look-up table approach for safety level 2	112
7.2.3	The firmware limitations	113
7.2.4	The assumption of rare interlocks	113
7.2.5	The treatment plan converter	114
7.2.6	Resuming irradiations after level 1 interlocks	115
7.3	Future perspectives of line scanning	116
7.3.1	Open issues before clinical operation	116
7.3.2	The evolution of proton therapy: a methodological comparison	119
8	Concluding remarks	123

APPENDIX

A	List of publications	i
B	List of abbreviations	iii
C	List of figures	v
D	List of tables	vii

Bibliography

ix

Curriculum vitae

xxiii

Abstract

Pencil beam scanning (PBS) is becoming the standard of care for most cancer patients treated with proton therapy. It offers high dose conformity to the tumor and reduced integral dose to the healthy tissues compared to conventional radiation therapy. However, due to the pronounced sensitivity of PBS treatments to motion during irradiation they are mostly restricted to static anatomical sites. A moving or deforming target can create undesired cold spots inside the tumor volume or harmful hot spots in neighboring critical structures. Numerous mitigation techniques have been proposed in the literature, but only a few of them have found their way into clinical practice. In most of the cases, and especially for rescanning, machine performance represents a major bottleneck to clinical implementation. Faster PBS irradiations, beyond current step-and-shoot approaches, would enable viable motion mitigation.

The next-generation scanning system at Paul Scherrer Institute – so-called Gantry 2 – was designed for faster patient treatments by steering the proton pencil beam continuously across the target. While developers have already demonstrated feasibility, clinical usage has been on hold due to missing safety measures. As such, it was the scope of this dissertation to develop and implement a dedicated beam monitoring system that minimizes the risks of fast and continuous irradiations on Gantry 2 without compromising the gain in performance. The monitoring system is required to supervise the treatment at all times and detect inaccuracies or errors that could potentially compromise the clinical outcome. As such, and because of accelerated machine performance, novel safety measures must be highly responsive and able to terminate the irradiation with marginal latencies.

A first conceptual study analyzes the risks associated with fast and continuous beam scanning on Gantry 2. Inaccuracies in the proton beam current and transverse beam position were identified as major sources of error requiring enhanced monitoring. The proton beam energy was considered equally critical in terms of dosimetric accuracy, however sufficient monitoring tools are already provided through the supervision of numerous beamline settings. Hence, the beam monitoring system was designed to detect beam current and position errors quickly and reliably. For this purpose, a two-stage safety system was introduced: Safety level 1 acts in real-time during the irradiation and samples ionization chambers in the gantry nozzle (beam current monitoring) and Hall probes in the beam-scanning magnets (beam position monitoring) every 10 μs . Interlocks can be triggered as soon as the difference between measured values and nominal setpoints exceeds a critical threshold. Safety level 2 is active whenever the scan sequence exhibits a planned interruption (e.g. to change the beam energy). It compares integrated dose profiles recorded with a strip monitor to nominal predictions and can also interrupt the treatment in case of clinically unacceptable deviations.

Both safety levels were successfully implemented and thoroughly tested on the Gantry 2 scanning system, which required substantial software and firmware enhancements. Since level 1 comparisons run on a 100 kHz clock in parallel to the irradiation, they must be performed in hardware. For this purpose, the field-programmable gate array of the beam monitoring system was equipped with sample predictor and comparator units as documented in the second study. Given clinically acceptable tolerances for the beam current and position derived from international norms and guidelines (third study), safety level 1 is able to restrict the differences between planned and delivered dose distributions in case of machine-related errors to ± 36 mGy (equivalent to 2% of a typical fraction dose). Deviations of this magnitude are expected to be free from any clinical consequences for the patient.

With the risk aspects being addressed in studies one to three, the final study investigates the clinical benefits of continuous irradiations in the context of moving target treatments under rescanning. Three liver tumors varying in size and shape have been considered. In over 1500 4D dose calculations, validated through numerous benchmarking measurements, a significant gain in performance could be confirmed, especially for the larger targets (~ 300 cm³ or more). Consequently, continuous scanning is able to deliver more rescans in any given time window compared to discrete PBS irradiations, maximizing the mitigation strength. Furthermore, increased flexibility in beam delivery enables higher rescanning capability for continuous irradiations adding to their effectiveness. The study concludes that rescanning represents a viable mitigation strategy for motion amplitudes smaller than ~ 10 mm when performed using continuous beam scanning.

This accelerated form of patient treatment has matured through the work presented in this thesis, and now represents a safe alternative to step-and-shoot irradiations. Combined with treatment planning software that optimizes both target coverage and machine performance, continuous scanning could help to broaden the window of indications that benefit from proton therapy and make this technique available to a much larger number of cancer patients.

Zusammenfassung

In der Protonentherapie kristallisiert sich das Abtasten des Tumors mit Nadelstrahlen – kurz PBS – zunehmend als Behandlungsstandard heraus. Dosisverteilungen können mithilfe dieser Bestrahlungsart eng auf das Tumolvolumen beschränkt werden. Die Gesamtdosis im umliegenden Gewebe ist dabei deutlich reduziert gegenüber konventioneller Radiotherapie. Bislang sind Behandlungen jedoch hauptsächlich auf statische Bereiche der Anatomie beschränkt, da sich bewegende oder deformierende Zielvolumina lokale Über- bzw. Unterdosierungen hervorrufen können. In der Literatur sind zahlreiche Ansätze beschrieben, wie diese Bewegungseffekte zu minimieren sind. Allerdings werden nur wenige davon klinisch angewendet. Grund dafür ist in den meisten Fällen die mangelnde Leistungsfähigkeit des Bestrahlungsapparates. Dies gilt im Besonderen für das wiederholte Bestrahlen des Tumors, um Bewegungseffekte auszuschmieren. Schnellere PBS-Bestrahlungsanlagen könnten daher maßgeblich dazu beitragen, die Protonentherapie auch für bewegte Tumore praktikabel zu machen.

Am Paul Scherrer Institut wurde zu diesem Zweck eine neue PBS-Bestrahlungsanlage entwickelt – die Gantry 2. Sie bewegt den Protonenstrahl kontinuierlich (und nicht wie herkömmlich in diskreten Schritten) durch das Zielvolumen und kann Dosisverteilungen daher schneller applizieren. Die technische Umsetzung von kontinuierlichen Bestrahlungen auf Gantry 2 ist bereits weit fortgeschritten. Allerdings fehlt noch immer ein geeignetes Sicherheitssystem, das die Bestrahlungsparameter kontinuierlich überwacht, um den Weg hin zur klinischen Anwendung zu ebnen. Dies ist das Ziel dieser Arbeit. In der Entwicklung des Sicherheitssystems wurde besonders darauf geachtet, die Risiken verbunden mit kontinuierlichen Bestrahlungen weitestgehend zu minimieren, ohne dabei die Vorteile einzuschränken. Nichtsdestotrotz müssen Ungenauigkeiten und Fehler in der Behandlung verlässlich detektiert werden, um Beeinträchtigungen des klinischen Ergebnisses zu verhindern. Aufgrund der hohen Leistungsfähigkeit der Gantry 2 müssen die neuen Sicherheitsmaßnahmen derart reaktionsschnell sein, dass die Bestrahlung im Falle eines Fehlers innerhalb verschwindend geringer Latenzzeiten abgebrochen werden kann.

In einer ersten, konzeptionellen Studie wurden die Risiken verbunden mit den schnellen, kontinuierlichen Bestrahlungen auf Gantry 2 analysiert. Der Strahlstrom und die transversale Strahlposition konnten dabei als Hauptfehlerquellen identifiziert werden. Die Protonenenergie ist ein ebenso kritischer Parameter. Sie wird jedoch durch das Auslesen der Strahlführungseinstellungen bereits effektiv überwacht. Daher ist es die Hauptaufgabe des neuen Sicherheitssystems, Fehler im Strahlstrom und der Strahlposition schnell und verlässlich zu detektieren. Zu diesem Zweck wurden zwei Sicherheitsebenen eingeführt: Ebene 1 läuft in Echtzeit und fragt Ionisationskammern am Ende der Strahllinie (Stromüberwachung) sowie Hall-Sonden in den Ablenkmagneten (Positionsüberwachung) alle 10 μ s ab. Falls die Differenz zwischen Mess-

und Sollwert einen kritischen Toleranzwert überschreitet, wird ein Abbruchsignal an das Kontrollsystem gesendet. Ebene 2 ist während vorgesehener Unterbrechungen in der Bestrahlung (z.B. durch Energiewechsel) aktiv und vergleicht integrale Dosisprofile aus Streifenkammermessungen mit nominellen Vorausberechnungen. Die Behandlung wird nur dann fortgesetzt, wenn die Abweichungen innerhalb klinisch akzeptabler Grenzwerte liegen.

Zahlreiche Software- und Firmware-Erweiterungen waren nötig, um beide Sicherheitsebenen erfolgreich auf Gantry 2 zu implementieren und zu testen. So laufen Mess- und Sollwertvergleiche der Ebene 1 beispielsweise in einem integrierten Schaltkreis (FPGA) im 100 kHz-Takt parallel zur Bestrahlung. Entsprechende Vergleichsfunktionalität musste zunächst bereitgestellt werden, wie in der zweiten Studie beschrieben. Es konnte gezeigt werden, dass Ebene 1 mithilfe adäquater Toleranzen – abgeleitet aus internationalen Normen und Richtlinien (dritte Studie) – die Differenzen zwischen applizierter und geplanter Dosisverteilungen im Fehlerfall auf ± 36 mGy beschränkt. Dieser Wert entspricht 2% einer typischen Fraktionsdosis. Bei Abweichungen dieser Größenordnung werden für den Patienten keinerlei klinische Konsequenzen erwartet.

Die Studien eins bis drei behandeln die Risikoaspekte verbunden mit kontinuierlichen Bestrahlungen. Die finale Studie erörtert schließlich ihren klinischen Nutzen im Hinblick auf wiederholte Bestrahlungen bewegter Tumore. Dazu wurden drei Leberkarzinome unterschiedlicher Form und Größe betrachtet. In über 1500 4D-Dosisberechnungen – validiert anhand zahlreicher Messungen – konnte der erwartete Leistungsgewinn nachgewiesen werden. Für Tumorumfängen größer als ~ 300 cm³ ist dieser besonders ausgeprägt. Infolgedessen können in einem beliebigen Zeitfenster stets mehr kontinuierliche als diskrete Bestrahlungswiederholungen ausgeführt werden, was das Ausschmieren von Über- und Unterdosierungen begünstigt. Die erhöhte Flexibilität der kontinuierlichen Tumorbestrahlung wirkt sich ebenfalls positiv auf ihre Wirksamkeit aus. Für Bewegungsamplituden kleiner als ~ 10 mm bilden kontinuierliche Bestrahlungswiederholungen somit einen praktikablen Lösungsansatz zur Unterdrückung von Bewegungseffekten.

Im Rahmen dieser Arbeit wurden kontinuierliche Bestrahlungen auf Gantry 2 maßgeblich weiterentwickelt. Sie stellen nun eine sichere Alternative zu herkömmlichen, diskreten PBS-Bestrahlungen dar. Mithilfe kontinuierlicher Bestrahlungen und spezieller Therapieplanungssoftware, die die Abdeckung des Zielvolumens und die Schnelligkeit der Bestrahlung gleichzeitig optimiert, ließen sich die behandelbaren Indikationen ausweiten, um zukünftig mehr Krebspatienten Protonentherapie anbieten zu können.

1

Introduction

Risk is more than failure probability. Based on personal concerns, familiarities, level of knowledge, and available control measures, we form our own perception of risk, often decoupled from the underlying factual probabilities (Slovic, 1987). Consequently, our unconscious behavior may exhibit irrational twists, as demonstrated by Monat et al. (1972). The authors tested the stress reactions of university students to anticipated electric shocks and found that a decrease in shock probability from 100% to 50% and eventually to 5% did not trigger a significant decrease in anticipatory stress. In fact, students facing an electric shock and those likely to avoid one (5% group) showed very similar physical arousal. Despite the overwhelming reduction in shock probability, their perception of risk was comparable. Only when the risk was reduced to 0% did the students start to show significantly different behavioral patterns. This *probability neglect* has been confirmed in numerous follow-up studies (e.g. Rottenstreich and Hsee (2001) or Suter et al. (2016)).

Benefit is the natural balance to risk. It determines our willingness to accept certain risks. Our rational perception of this counterpart is equally biased: Viscusi et al. (1987) confronted consumers with an insecticide that is known to cause injuries when touched or inhaled. They asked the customers how much more they were willing to pay for a safer product. Reducing the risk of injury from 15 to 10 incidents per 10,000 bottles was worth an average surcharge of 10.4%; reducing the risk down to five incidents worth 13.7% surcharge. Astonishingly, customers were willing to pay an extra 37.8% for a completely risk-free product, which is far beyond the linear cost extrapolation. The so-called *zero-risk bias* twists our perception of the associated benefit. Influenced by anxiety or social norms, we value risk reductions disproportionately higher the closer to certainty they are (Schneider et al., 2017).

1 Introduction

Under the circumstances of *probability neglect* and *zero-risk bias*, modern radiation therapy must pursue rigorous risk management to guarantee patient comfort and safety. Any residual risk in case of technical failures can result in fatal consequences and is, hence, associated with direct responsibility. As such, manufacturers of irradiation devices implement multi-level safety systems that rely on redundant measures to detect any kind of failure during the irradiation and restore a safe state. But how safe is safe enough? Self-evidently, a treatment with zero risk can only mean no treatment at all, which is not an option for many cancer patients. In the context of this dilemma, the International Electrotechnical Commission (2014) recently answered this fundamental question. They request at least two independent safety stages for particle therapy installations in their norm. Furthermore, they specify tolerances for deviations from the prescribed irradiation that are expected to have marginal impact on the clinical outcome of the treatment. The absolute range uncertainty of the beam must be smaller than 1 mm and the excess dose in case of technical failures must stay below 250 mGy¹. Respecting these tolerances facilitates low-risk irradiations from a machine point-of-view, which may help to promote the doctor's confidence in the treatment and diminish the patient's concerns about it.

The primary goal of this thesis is to enhance the current patient safety system at the Center for Proton Therapy (CPT) of the Paul Scherrer Institute (PSI) to be able to supervise fast and highly dynamic irradiations. Researchers at CPT are investigating such advanced forms of patient treatment and have already been able to demonstrate promising results (Zenklusen et al., 2010; Schätti et al., 2014; Fattori et al., 2016; Psoroulas et al., 2016b). However, to enable clinical integration, norms and regulations require enhancing the current safety system with functionality dedicated to fast and dynamic treatments. For this purpose, novel developments were designed, implemented and tested as reported in this thesis. By following a strict approach towards risk-minimization, it was possible to satisfy the official requirements while addressing the subjective perceptions of *probability neglect* and *zero-risk bias*. Having a multitude of safety measures running in parallel to the irradiation will hopefully diminish concerns by conveying a zero-risk feeling to patients as well as to the legal authorities.

This introduction provides background information on the rationale of proton therapy and the need for faster irradiation techniques. Section 1.1 compares conventional radiotherapy with photons to treatments using proton beams. Their generation and transport to the patient is briefly outlined in section 1.2. Section 1.3 introduces the problem of organ motion during treatment and section 1.4 lists the mitigation techniques currently practiced or investigated. The benefit of fast irradiations and the need for dedicated safety measures are motivated in section 1.5. The final section 1.6 explains the role of this thesis in the context of fast and dynamic irradiations

¹250 mGy is the minimum value. The actual tolerance can be higher depending on the prescribed dose of the treatment.

in proton therapy. Furthermore, it portrays an overview of the different chapters of this thesis and their contribution to the achievement of the research goals.

1.1 The advantages of proton beam therapy

Ionizing radiation sterilizes cells: the higher the ionization density, the higher the local sterilization probability. Thus, it is desired to irradiate tumors to high doses of radiation, whilst sparing the surrounding healthy tissues as much as possible. Proton beam therapy offers one clear advantage in this regard: when selecting the correct kinetic energy, the beam will stop completely inside the tumor volume, leaving tissues a few millimeters behind the target unaffected. Moreover, the energy deposition reaches a localized maximum, the so-called Bragg peak (Bragg and Kleeman, 1905), near the end of the proton range which leverages damage localization within the tumor. By superimposing individual Bragg peaks through successive beam energy adaptation according to the tumor size and location in the body, one can deliver confined and homogeneous dose distributions to the target. The resulting spread-out Bragg peak (SOBP) is shown figure 1.1 below (blue curve).

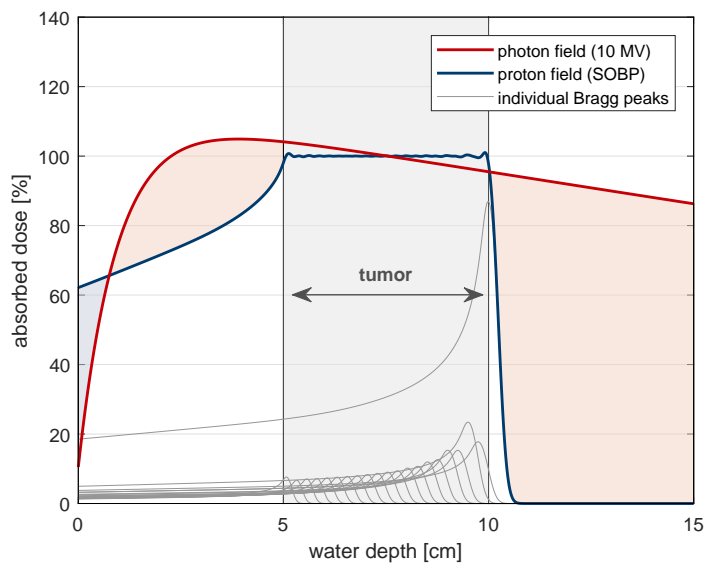


Figure 1.1: A dosimetric comparison of conventional radiotherapy (red curve) and proton beam therapy (blue curve). The broad 10 MV photon field was optimized to deliver an average dose of 100% to the tumor region. The SOPB consists of 21 individual Bragg peaks (gray lines) optimized in weight to deliver a flat dose distribution to the target when superimposed. The two areas shaded in red demonstrate how the photon field deposits much more dose outside of the tumor volume compared to proton field. However, its skin and entrance dose in the first 7 to 8 mm are significantly higher.

When comparing the SOBP to the depth-dose distribution of a large 10 MV photon field (red curve), one observes a significant difference in dose deposition outside of

the target. In this example case – the dimensions are typical for a tumor situated near the brain stem – photon radiation delivers 2.2 times more dose to the surrounding healthy brain compared to proton radiation as indicated by the two areas shaded in red. Only the skin and entrance doses are higher for protons (area shaded in blue). Lomax et al. (1999) compared dose distributions of proton and intensity-modulated photon radiotherapy in a treatment planning study and predicted that “*the use of protons could lead to a reduction of the total integral dose by [...] a factor two compared to intensity-modulated photon plans.*” Chang et al. (2006) and Steneker et al. (2006) concluded similar values for lung and head-and-neck tumors, respectively.

Non-target dose can be linked to secondary cancer risk (ICRP, 1991), which is of pronounced concern for pediatric patients. Miralbell et al. (2002) demonstrated how a reduction in integral dose through proton beam therapy can potentially reduce the incidence of radiation-induced secondary cancers. As such, proton therapy can be regarded as the preferred irradiation technique for pediatric patients although published clinical data on long-term (side) effects are still sparse (Chung et al., 2013; Leroy et al., 2016).

1.2 The pencil beam scanning technique

Proton therapy is a mature technique offered by more than 50 centers around the world. By the end of 2016, nearly 150,000 patients have received proton therapy (Particle Therapy Co-Operative Group, 2016). Centers and their commercial vendors mainly utilize two techniques to deliver protons to the tumor: *passive scattering* (Koehler et al., 1977) and *pencil beam scanning* (PBS) (Renner et al., 1989). Both of them require an accelerator (e.g. a cyclotron or synchrotron) that creates a monoenergetic and narrow proton beam of a few mm width in air. The passive scattering technique spreads the narrow beam using scatter foils and shapes it to the outline of the target using patient-specific collimators and compensators. The SOBP is created by inserting range-shifting material into the beam path. This simple technique looks back on more than 40 years of clinical experience. However, it requires hardware in the beamline – in close proximity to the patient – which generates significant neutron background dose (Hälg et al., 2014). PBS, on the other hand, works without patient-specific collimators and compensators. A pair of scanner magnets deflects the beam in the transverse plane to cover the entire lateral extent of the tumor. Energy modulation is typically done far upstream from the patient if not by the accelerator itself. As such, the proton beam maintains its narrow shape when entering the patient. Combined with precise control measures and accurate treatment planning, PBS features superior dose conformity to the target in the cranium (Urie and Goitein, 1989), opens up the possibility of in-field dose modulation (Lomax, 1999), and uses the beam more efficiently (e.g. no losses at collimators).

1.3 The problem of organ motion

In the framework of this thesis, we shall focus on one major drawback of PBS: its sensitivity to intra-fractional anatomical variations such as breathing, heartbeat or intestinal activity (Bert and Durante, 2011). What is commonly referred to as organ motion during treatment has a threefold effect on the delivered dose distribution:

- (1) Due to variations in the range, the proton beam may over- or undershoot resulting in target miss. Mori et al. (2008) showed that this effect is especially pronounced in the treatment of lung tumors because of large density variations in the beam path (e.g. differences between lung and tumor tissue).
- (2) Furthermore, organ motion blurs dose gradients yielding compromised penumbras and, consequently, less conformal dose distributions (Bortfeld et al., 2004). Blurring effects also occur in case of inter-fractional anatomical variations due to e.g. setup errors, weight loss or tumor shrinkage.
- (3) In addition to target miss and dose blurring, a third effect is pronounced in PBS – the interference of the beam-scanning dynamics with the motion of the patient anatomy (Phillips et al., 1992). Deteriorated dose distributions arise exhibiting undesired hot and cold spots as shown in figure 1.2 below. The so-called interplay effect has been quantified in numerous studies (e.g. Lomax (2008), Bert et al. (2008), Seco et al. (2009), Zhang et al. (2012) or Grassberger et al. (2013)). In summary, it depends on the amplitude and type of motion, on the outline of the target and its location in the body, on the beam delivery characteristics, and on the formulation of the treatment plan.

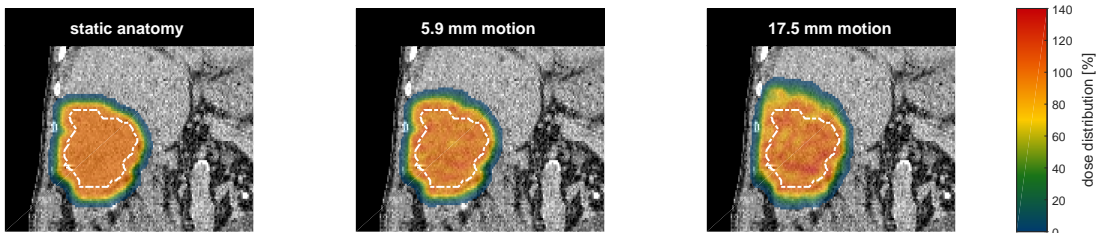


Figure 1.2: Interplay effect in a moving liver target. The static plan (left plot) shows a clinically acceptable dose distribution with homogeneous coverage of the clinical target volume (dashed white line). In presence of motion, hot and cold spots arise. Their magnitude and frequency increases with increasing motion amplitude. In both cases, inhomogeneities are clinically unacceptable and call for effective means of mitigation. 17.5 mm peak-to-peak motion (right plot) yields additional dose blurring outside of the target contour. Sufficient coverage can only be guaranteed through significant expansion of the target volume resulting in increased healthy tissue damage.

Considering target miss, dose blurring, as well as the interplay effect and its dependencies, Bert and Durante (2011) conclude that *“in the case of scanned beam delivery,*

the presence of organ motion requires more complex mitigation procedures". A brief summary of the approaches applied in clinical practice and under investigation is provided in the following section.

1.4 The multitude of solutions to organ motion

Cardiac and respiratory motion impede the accuracy and precision of radiation therapy, especially for gastrointestinal cancers (Abbas et al., 2014). Periodic variations in the patient anatomy must be quantified prior to the treatment, e.g. through four-dimensional computed tomography (4D CT) or four-dimensional magnetic resonance imaging (4D MRI). The fourth dimension refers to time-resolved data acquisition in this context. Ideally, motion is also monitored during the treatment using e.g. fluoroscopy, ultrasound, implanted radio-frequency transponders or surface tracking (Evans, 2008). These imaging modalities are key to successful mitigation of organ motion using either of the following approaches.

Up-front planning

The design of the treatment plan offers sufficient degrees of freedom to incorporate various motion mitigation techniques: One can enlarge the target volume to encompass the entire motion envelope. As such, acceptable coverage can be granted by addressing target miss and dose blurring effects (Knopf et al., 2013). However, increasing the irradiated volume in such a fashion also increases the integral dose to healthy tissues or organs at risk and, as such, substantially compromises the main advantage of proton beam therapy. A second option is to incorporate range uncertainties in the treatment plan optimizer in order to be robust against induced range variations. Unkelbach et al. (2009) demonstrated this approach mainly for systematic setup and CT uncertainties, but the concept could be expanded to mitigate for undesired interplay effects (Bernatowicz et al., 2017). This approach – often referred to as (robust) 4D optimization in the literature – requires very detailed prospective knowledge of the motion curve and the beam delivery characteristics and, hence, lacks clinical viability. Last but not least, it could be beneficial to accumulate the daily delivered dose distributions on a reference CT and adapt the subsequent plan according to observed inaccuracies (Lomax, 2014). This strategy requires precise knowledge of the anatomical variations that occurred during the irradiation of the day in order to recalculate the delivered dose distribution correctly. Furthermore, daily imaging would be beneficial to account for weight loss, cavity fillings or tumor shrinkage in the daily plan. While this approach offers the possibility to account for inter-fractional motion, dosimetric effects arising from anatomical variations during the treatment remain unaddressed.

Anatomical immobilization

One of the most universal motion management techniques is to freeze the patient anatomy as much as possible during irradiation. A temporarily stationary anatomy allows for targeted irradiations with minimal margins, mitigates for interplay effects and exhibits little dose blurring, providing it is reproducible (Engelsman et al., 2013). The following three options for temporary immobilization are currently in clinical practice: Abdominal compression can be applied to limit diaphragmatic expansion and induced organ motion. Heinzerling et al. (2008) showed that lung and liver tumor motion can be kept below 10 mm when using a compression plate. However, the example in figure 1.2 demonstrates that motion amplitudes of this magnitude can still produce significant interplay patterns in PBS. As such, supplementary mitigation is required. Breath-hold control represents an alternative to abdominal compression. The tumor is only irradiated during e.g. deep inspiration, which limits the amount of residual motion. Dueck et al. (2016) conclude that *“the breath-hold approach is a realistic clinical option for treating lung tumors with PBS proton therapy.”* However, small targets with comparably large baseline shifts remain problematic due to irreproducible tumor positions. Furthermore, irradiation times need to be short to demand only very few breath-holds from the patient during each treatment. A third option for temporary immobilization is beam gating (Ohara et al., 1989). Widely used in Japan, this technique limits the beam-on intervals to certain phases of the breathing cycle. Real-time (surface) imaging of the patient is required to follow the tumor in case of irregular motion curves. The technical demands on the irradiation system are equally high: frequent beam on/off commands must be executed with minimal latency to ensure accurate beam delivery. A significant drawback of this technique is the increased treatment time due to the introduction of dead time outside of the gating window.

It is worth indicating that all three motion mitigation strategies mentioned above address respiration-induced effects only. Cardiac and intestinal motion cannot be mitigated using abdominal compression, breath-hold or gating.

Tumor tracking

Tumor tracking is in principle the most comprehensive of all motion mitigation techniques. The idea is to image the patient continuously during the treatment and to adapt delivery parameters in real-time according to the detected changes in the anatomy (Keall et al., 2001). As such, tracked treatments nominally deliver the most precise dose distribution with minimal range, blurring or interplay effects and eliminate the need for additional margins. In conventional radiotherapy, tumor tracking is an available mitigation technique, for instance on CyberKnife[®] (Accuray) or vero4DRT (Mitsubishi) systems, and potentially on TrueBeam[™] (Varian) or Versa HD[™] (Elekta) systems as well. However, proton therapy imposes much stronger demands on the irradiation technology than conventional radiotherapy (e.g. real-time

1 Introduction

plan adaptation, instantaneous pencil beam control) (Riboldi et al., 2012). It is not only required to adapt the beam position in the transverse plane, but also in depth, which necessitates an energy modulation system with short latencies. Although Grözinger et al. (2008) presented a technical feasibility study almost ten years ago, the accuracy reached today is still insufficient to consider clinical application.

Rescanning

In contrast to tumor tracking, rescanning is a motion mitigation technique with low technical hurdles. As the name suggests, rescanning describes repeated irradiations of the same field. Each irradiation carries only a fraction of the prescribed dose such that, in superposition, the delivered dose distribution will equal the prescribed one (Phillips et al., 1992). Provided asynchronous beam delivery, each rescan will produce different interplay patterns in the target volume. When applying sufficient number of rescans, their superposition will have an averaging effect yielding a homogenized dose distribution inside the target and blurred dose gradients within the expanded margins. Figure 1.3 exemplifies this principle.

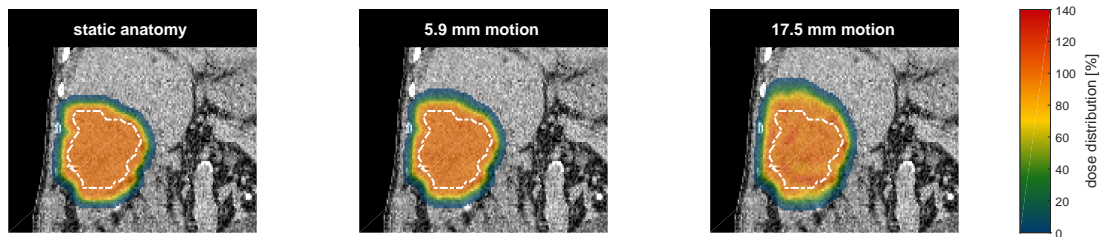


Figure 1.3: Rescanning a moving liver target. The static plan (left plot) shows the prescribed dose distribution to the clinical target volume (dashed contour). After applying ten scaled, volumetric rescans to the moving liver target, interplay effects observed in figure 1.2 are averaged out to a large degree. The effectiveness of mitigation is higher for smaller motion amplitudes (middle plot). In case of larger amplitudes (right plot), residual interplay patterns remain. The amount of healthy tissue irradiated is also increased in this example due to larger margins.

Rescanning can be performed in two different modes: *layered* or *volumetric* (Rietzel et al., 2005). In layered mode, each iso-energy slice is rescanned multiple times before moving to the next layer. As such, the entire energy sequence, as given by the treatment plan, is only executed once. This is an advantage for therapy systems using synchrotrons, since the time it takes to switch the beam energy can easily amount to several seconds. In volumetric mode, the entire energy sequence is repeated multiple times according to the number of rescans. This mode increases the amount of energy changes substantially and it may be a viable solution only for systems with short energy switching times (e.g. cyclotrons in combination with mechanical degraders) (Bernatowicz et al., 2013).

Scaling the field dose can also be done in two different ways as suggested by Zenklusen et al. (2010). The authors refer to *scaled* rescanning when proportionally reducing the dose delivered by each pencil beam according to the number of rescans. This approach can result in a multitude of very low-weighted dose elements, which may not necessary be deliverable by the scanning system. On the other hand, it guarantees a fixed and uniform number of rescans. The counter-approach, so-called *iso-layered* rescanning, splits every pencil beam in fractions of equal weight. Setting the fraction size above machine constraints guarantees that every rescan can be delivered. However, iso-layered rescanning yields varying number of rescans for every pencil beam contained in the plan. Highly weighted pencil beams will be re-irradiated impractically often, whereas low-weighted ones may not be rescanned at all.

The PSI Center for Proton Therapy applies volumetric rescanning in combination with hybrid dose scaling in clinical routine. Each pencil beam is proportionally scaled according to the number of desired rescans. However, when falling below the minimum deliverable threshold, the number of rescans is decreased successively for that particular pencil beam until the lower limit is satisfied (Zhang et al., 2016). As such, not all pencil beams contained in the plan may receive the full number of rescans, but the spectrum is narrower compared to pure iso-layered dose scaling. In 2017, the first six patients with moderately moving targets (amplitudes < 5 mm) were treated under rescanning. The indications have been neuroblastoma (five) and non-small cell lung carcinoma (one). All of the patients were pediatric.

Although being comparably easy to implement, the effectiveness of motion mitigation achieved by rescanning is rather difficult to predict. Previous studies identified dependencies on motion amplitude (Bert et al., 2008; Schätti et al., 2013), motion estimation (Zhang et al., 2012), beam width (Grassberger et al., 2013), tumor size (Zenklusen et al., 2010), rescanning type (Schätti et al., 2013; Bernatowicz et al., 2013; Grassberger et al., 2015) and performance parameters of the delivery system (Bernatowicz et al., 2013; Dowdell et al., 2013). Another obstacle are so-called resonance effects, in which the rescanning sequence partially synchronizes with the motion curve decreasing the averaging capability. Irregularities in the breathing pattern (Zhang et al., 2016), random pauses in the irradiation (Rietzel and Bert, 2010) or strict phase control (Furukawa et al., 2007) proved to decrease the likelihood of resonances. Ultimately, rescanning prolongs the overall treatment time due to accumulation of dead times in the irradiation sequence (e.g. when switching pencil beam positions or energies). The amount of extra time needed varies drastically across different beam delivery systems (Furukawa et al., 2010a; Schätti et al., 2014) and also depends on the actual integration of rescanning into the clinical workflow (Mori et al., 2014a,b).

1.5 The need for fast, dynamic scanning and dedicated safety measures

Pencil beam scanning can be considered fast, when the time it takes to switch energies is minimized (~ 100 ms) and the scanning speeds in the transverse plane are of the order of ~ 1 cm/ms. In addition, a high beam current at the patient (~ 5 nA) will help to decrease irradiation times even further. But most importantly, all dead times in the irradiation sequence must be minimized in order to guarantee a high duty cycle (optimally $> 75\%$). However, irradiations need to be not only fast but also highly dynamic to be able to accurately deliver the prescribed treatment plan. Ideally, one could steer the beam to any point in the transverse plane while modulating the scanning speed and beam current. In case of static targets (e.g. brain or head-and-neck tumors), fast and dynamic irradiations of that kind may only offer minimal gains compared to regular, state-of-the-art treatments (Schätti et al., 2014). But in the case of moving targets, the gains could be substantial:

- The beam gating and breath-hold approach leave only short windows in which the irradiation can be carried out. Efficient beam delivery minimizes the amount of windows required for treatment (Fattori et al., 2016). As such, it provides more comfort for the patient and avoids significant dead time between irradiation windows. In the case of beam gating or breath-hold, a high beam current is a clear advantage.
- Tumor tracking requires short reaction times to changes in the anatomy. Hence, it can only be performed on scanning systems that can adapt the transverse beam position and energy within milliseconds. A highly dynamic system is much more important in this case than high beam currents or duty cycles.
- When rescanning moving targets, fields of (very) low dose will be irradiated numerous times. As such, continuous irradiation, minimized dead times and fast scanning speeds are of profound importance. Furthermore, flexibility in lowering the beam current at any point in the target provides a decisive advantage: the lower the beam current, the lower the applicable field dose and the higher the number of possible rescans. And as indicated in section 1.4 above, frequent rescans average out interplay patterns more effectively than fewer rescans.
- Combinations of gating and rescanning or breath-hold and rescanning could be a possibility to tackle large-amplitude motions. In this case, the need for a fast and dynamic scanning system becomes even more obvious.

Ultimately, therapy centers would like to offer treatment to many patients each day rather than a few with moving targets. To meet these demands, researchers at

CPT have developed a second-generation scanning system – Gantry 2 – dedicated to fast and dynamic irradiations (Pedroni et al., 2004, 2011; Safai et al., 2012). Besides regular, state-of-the-art treatments, Gantry 2 features irradiations in an accelerated mode of operation called *line scanning* (Zenklusen et al., 2010). This irradiation technique steers the proton beam continuously along straight lines across the target drastically reducing dead times in the treatment (Schätti et al., 2014) and potentially increasing flexibility in dose modulation (Pedroni et al., 2011). In line scanning, beam delivery is based on trajectory tables allowing for fast and frequent modulation of the beam scanning speed. The beam current follows similar delivery tables enabling twofold dose modulation. As such, line scanning comprises many of the features described in the list above, but its current beam monitoring and safety system cannot supervise them adequately. For instance, it cannot cope with the wide range of accessible beam currents, it cannot monitor continuous irradiations over extended time periods, it fails to validate arbitrary scan patterns in the transverse plane and it prohibits frequent modulations of the scanning speed and beam current all together. In other words, desirable fast and dynamic patient treatments in line scanning mode are not permitted, yet, for they are still lacking dedicated safety measures.

1.6 The scope and role of this thesis

It is the scope of this thesis to identify and implement the required safety measures that enable safe irradiations in line scanning mode. For this purpose, four principle research questions have been formulated, each addressed in a separate publication. Preprints of these publications are included as individual chapters in this thesis. This section summarizes the role of each paper in answering the different research questions. Furthermore, it explains my contributions to the published work and, as such, serves as a basis for the discussion chapter.

The first principle research question concerns the conceptual design of an adequate safety system for line scanning:

\mathcal{Q}_1 How can irradiations using the line scanning technique be monitored reliably?

The first publication (see chapter 3) summarizes the conceptual aspects of this dissertation. It assesses the risks associated with the line scanning technique and deduces the safety requirements. Furthermore, it investigates the performance of the diagnostic elements along the beamline in order to ascertain which of the risks they could minimize. This paper ends with the formulation of a two-stage monitoring strategy by assigning specific safety tasks to each of the diagnostic devices. The working principle is exemplified based on the irradiation of a single line scan. I contributed to this publication by assessing the risks, defining the safety strategy, testing the hardware response in numerous experiments, and developing algorithms that model beam parameters and detector response based on empirical data.

1 Introduction

The second principle research question addresses the technical implementation of the safety system and related novelties:

\mathcal{Q}_2 How can real-time beam monitoring be implemented on the current hardware topology?

The second publication (see chapter 4) focuses on the real-time aspects of the line scanning safety system. It describes the entire signal flow during irradiation from control system to detectors and their corresponding readout electronics. Moreover, it specifies required software and firmware enhancements to enable real-time beam monitoring on the Gantry 2 scanning system. Their functionality was tested based on three exemplary error scenarios. I contributed to this publication by specifying and developing required software and firmware enhancements, testing their functionality, and demonstrating their efficacy when confronted with failures.

The third principle research question targets compliance with international protection norms and guidelines:

\mathcal{Q}_3 Which safety tolerances apply to the individual parameters monitored during line scanning irradiations?

Having designed and implemented a safety system, it is important to demonstrate compliance with the norms and guidelines provided by the International Electrotechnical Commission (2014) and the International Commission on Radiation Units and Measurements (2007). As such, the third publication (see chapter 5) derives a set of acceptable safety tolerances for line scanning that guarantee minimal compromise on the clinical outcome of the treatment in case of unforeseen technical failures. I derived these tolerance from first principles, compared them against values reported in the literature and demonstrated that the implemented safety system is able to respect them in case of erroneous irradiations.

The fourth and final principle research question goes beyond safety aspects by examining the clinical use case of the line scanning technique in the context of motion mitigation:

\mathcal{Q}_4 How effective and how efficient is the line scanning technique when trying to mitigate interplay patterns using rescanning?

The fourth publication (see chapter 6) answers this question by investigating the dosimetric coverage of moving targets in the liver when approached using the rescanning strategy combined with the line scanning irradiation technique. This paper includes a large set of 4D dose calculations validated by a smaller set of benchmarking measurements. I contributed to this final publication by designing the study, selecting patient cases, identifying the parameters to be investigated, performing all measurements, analyzing the data, and drawing the statistically valid conclusions.

In addition to this introduction and the four publications mentioned above, this dissertation contains the following three chapters: *Materials and methods* (see chapter 2) describes the Gantry 2 scanning system including actuators for beam delivery and diagnostic devices for beam monitoring. Furthermore, it provides an overview on the detectors used and tools developed within the framework of this thesis concerning data acquisition and analysis. *Discussion and outlook* (see chapter 7) reviews these methods critically. It brings the results of the different publications together, compares them to the literature, and provides future perspectives of the line scanning technique. *Conclusion* (see chapter 8) summarizes the key findings of this thesis and answers the four principle research questions.

2

Materials and methods

Answering the four principle research questions of this dissertation requires a comprehensive set of tools and methods. Each of the four publications includes a brief summary of those mentioning the most important devices and algorithms only. This chapter expands these descriptions to provide a more detailed overview on the relevant materials and methods. As such, it follows the structure laid out by the four principle research questions: Q_1 asks how line scanning could be monitored reliably. For this purpose, the Gantry 2 pencil beam scanning system needs to be understood in great detail. Actuators delivering the beam to the patient and detectors supervising their actions are described in section 2.1 of this chapter. This system review also represents the starting point for research question Q_2 targeting the implementation of real-time monitoring on the current hardware topology. The description of the scanning system is followed by a mathematical characterization of discrete and continuous pencil beam scanning (see section 2.2). Quantifying the differences is necessary in order to model the response of the system to continuously scanned beams and derive adequate safety margins (see research question Q_3). Furthermore, these mathematical considerations enabled converting discrete treatment plans to continuous ones of similar quality. This converter was used for all measurements, especially those analyzing the effectiveness and efficiency of line scanning in clinical applications (see research question Q_4). In most of the measurements conducted, delivered dose distributions were recorded with an imaging system assembled by Schätti et al. (2013). Section 2.3 describes the calibration of this system and introduces required corrections. Section 2.4 outlines the typical experimental setup and data analysis tools.

2.1 The Gantry 2 pencil beam scanning system at PSI

The Gantry 2 pencil beam scanning system, as depicted in figure 2.1, offers state-of-the-art proton therapy treatments. In addition, it was designed to serve as a research platform to facilitate developments such as faster irradiations. Gantry 2 supports iso-centric rotations around the patient from -30° to $+180^\circ$ and operates clinically since November 2013 using discrete irradiations commonly referred to as spot scanning (Pedroni et al., 1995). Additionally, Gantry 2 features an accelerated mode of operation – continuous line scanning (Zenklusen et al., 2010; Pedroni et al., 2011; Safai et al., 2012) – which is at a pre-clinical stage. Because of the complexity of the scanning system, only those beamline elements with direct relevance for this dissertation will be mentioned here¹. As such, subsections 2.1.1 and 2.1.2 focus on selected actuators for beam delivery and detectors for beam monitoring only. Their location along the beamline is visualized in figure 2.1. Subsection 2.1.3 discusses the qualitative differences between spot and line scanning and additionally introduces a hybrid form of the two.

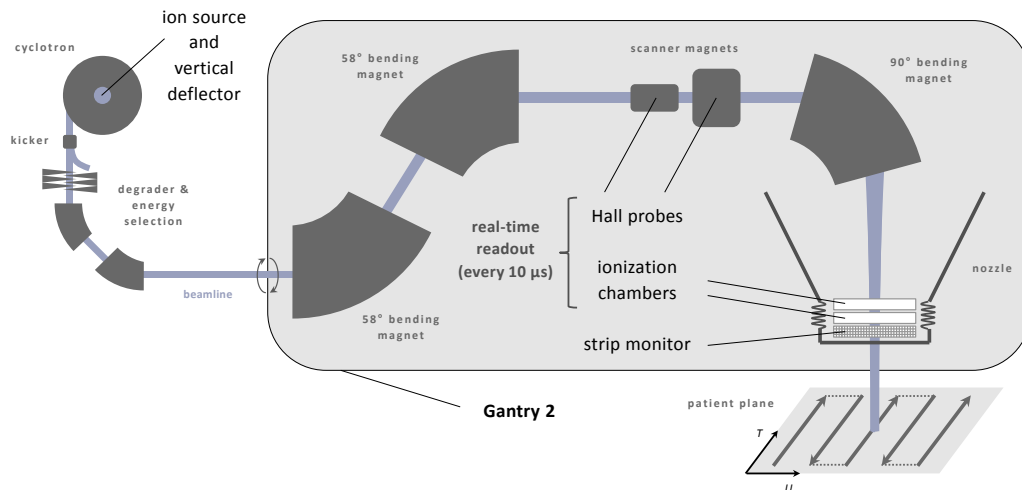


Figure 2.1: Vastly simplified sketch of the Gantry 2 beamline. A cyclotron provides a monoenergetic proton beam of 250 MeV that is decelerated by opposing carbon wedges (degrader unit). A subsequent double-bend achromat determines the momentum band transmitted to the gantry, on which the beam is deflected transversally by two scanner magnets. A final 90° dipole directs the proton beam towards the patient. Various sensors and monitors along the beamline and in the gantry nozzle (e.g. Hall probes and ionization chambers) supervise the irradiation. Missing elements such as collimators, slits, quadrupoles or sextupoles have been described in great detail by Pedroni et al. (2011).

¹Pedroni et al. (2011) provide a complete overview on the Gantry 2 scanning system including magnet and transport design, properties of beam optics, and commissioning results.

2.1.1 Actuators

The beamline actuators described in the following are controlled by the therapy delivery system (TDS). According to the steering file, the TDS sends out signals that ultimately define the energy, position and dose deposition of the proton beam. As such, it communicates with the machine control system to steer the accelerator, the degrader wedges, and the beam-scanning magnets. In addition, the TDS opens and closes the beamline by setting the kicker magnet and driving various beam blockers.

Cyclotron and vertical deflector

A superconducting 3.8 T cyclotron generates a continuous proton beam of 250 MeV. Extracted beam currents can be as high as 1 μ A with an extraction efficiency of up to 80% (Schippers et al., 2007a). To regulate the extracted beam current, two electrostatic plates are installed near the ion source in the center of the cyclotron. Powering these plates deflects the proton beam vertically off its plane of spiral orbit. Induced losses at collimators decrease the extracted beam current. The voltage on the deflector plates can be changed within less than 100 μ s allowing for frequent beam current regulation during irradiation. Residual fluctuations around the setpoint are aimed to be below 2% Gaussian σ (Schippers et al., 2007b). In continuous irradiations, the so-called vertical deflector is directly controlled by the TDS. Prior to the treatment, the voltage on the plates is calibrated against the beam current I measured at iso-center. As such, any value between 0% and 100% can be set during irradiation. The modulation of the beam current is feedback-controlled to achieve the required accuracy for patient treatments (Psoroulas et al., 2016a).

Kicker magnet

One of the first elements in the beamline is a dynamic dipole magnet that is able to deflect the beam away from a collimator hole, hence completely suppressing any transmission into the treatment room. The so-called kicker magnet has a beam-off reaction time of 50 μ s at up to 1 kHz repetition rate (Pedroni et al., 2011). In spot scanning irradiations, the kicker magnet is used to turn the beam on and off. In line scanning irradiations, the vertical deflector takes on this task and the kicker magnet functions as a redundant safety element. In case of detected interlocks, it is used to terminate the irradiation and guarantee a safe state of the machine. Including all system delays originating from monitors, readout electronics, and cabling, the reaction time to errors is less than 300 μ s.

Degrader

In order to adjust the penetration depth of the proton beam to the size and location of the tumor, its energy E needs to be modulated. For this purpose, two

opposing pairs of carbon wedges can be driven in and out of the beam path decelerating traversing protons. Clinically accessible energies are discretized and range from 230 MeV down to 70 MeV. When requesting an energy change of a few MeV, the mechanical movement of the wedges occurs in ~ 50 ms. However, it requires 106 ms on average to change the settings of all magnets downstream of the degrader including settling times. Self-evidently, material in the beam path introduces scattering that broadens the phase space. To counteract, the degrader unit is followed by two collimators that restore the beam size and angular divergence. Additionally, the proton beam passes through a double-bend achromat redefining the momentum band. These measures come at the cost of substantial beam current losses.

Scanner magnets and 90° dipole

Gantry 2 is an upstream scanning system. As such, the two dipoles that deflect the beam transversally across the (T, U) -plane at iso-center are positioned upstream of the final 90° bending magnet. Specifications of the T and U -scanners are given in table 2.1 below. To avoid eddy currents and enable rapid changes in field strength, the smaller T -scanner is equipped with a ferrite core. As such, line scanning is performed along the T -axis, which is perpendicular to the elevated beamline on the gantry (see figure 2.1 for a graphical representation of the coordinate system).

Table 2.1: Specifications of the Gantry 2 scanner magnets.

	T -scanner	U -scanner
length [cm]	20	40
gap [cm]	6	9
maximum field strength [T]	0.2	0.4
displacement at iso-center [cm]	± 6	± 10
maximum scan speed [mm/ms]	20	5

The subsequent 90° bending magnet hosts a large gap to accommodate for transverse deflections of the beam. It directs the beam towards the patient and enables parallelism across the scan area due to specifically tailored entrance and exit angles. These regions are also critical in terms of eddy currents counteracting changes in the magnetic field. Consequently, the lamination scheme had to be customized to preserve fast energy changes (Gabard et al., 2010).

2.1.2 Detectors

The control system is equipped with an independent monitoring system that supervises the actuators of the beamline to terminate the irradiation as soon as a

malfunction has been detected. As such, the therapy verification system (TVS) acts as a counterpart to the TDS by checking whether measured samples fluctuate within clinically acceptable tolerances. Interlocks are triggered upon tolerance violation and the beam is turned off. The proton beam energy is monitored indirectly by verifying the position of the degrader wedges with potentiometers and measuring the field strength of all beamline magnets with Hall probes. The proton beam current and dose deposition can be monitored directly with the help of two ionization chambers in the gantry nozzle. The transverse position of the proton beam is recorded by a strip monitor.

Potentiometers

The mechanical settings of collimators, phase slits and degrader wedges define the beam energy and momentum band transmitted to the coupling point of the gantry. High-resolution potentiometers from Genge & Thoma AG (5 k Ω and 150 mm measurement range) are mounted at these devices to supervise their position. The beam tune verification system compares the readout of the potentiometers against expected values obtained from the respective tune file. Interlocks are issued if the comparison fails.

Hall probes

The scanner magnets control the pencil beam position in the transverse plane: the higher the field strength, the larger the transverse deflections of the beam. Because of this correlation, the actual beam position at iso-center can be monitored indirectly by measuring the field strength inside the scanner magnets. For this purpose, a one-axis Hall probe from SENIS (type A) is placed inside each of the two scanner magnets. These Hall probes measure the magnetic field along the axis perpendicular to the probe plane (here y) utilizing an integrated single-chip. According to specifications, the field sensitive volume measures $(x, y, z) = (0.40 \times 0.01 \times 0.04) \text{ mm}^3$. Both Hall probes are connected to their F1 magnetic field transducers via 8 m long calcium hydride cables. They have an equal range of differential output. However, the Hall probe in the T -scanner magnet spans a measurement range of $\pm 0.2 \text{ T}$ with a sensitivity of 50 T/V, whereas the Hall probe in the U -scanner magnet has double the range but only half the sensitivity. Translating the noise on both probes to beam position at iso-center yields an uncertainty of less than 10 μm .

Ionization chambers

The Gantry 2 nozzle (see figure 2.1) hosts two plane-parallel ionization chambers, which will synonymously be referred to as dose monitors 1 and 2 in this thesis. Their performance has been investigated by Lin et al. (2009). Both dose monitors are filled with air at ambient temperature and pressure and operated in proportional counting mode ($U = 2 \text{ kV}$ chamber voltage). The two high voltage planes (anodes) consist of 20 μm thick Mylar foils coated with less than 0.1 μm aluminum. They

2 Materials and methods

are separated by a 20 μm thick aluminum foil serving as the cathode. The distance between the cathode and anode planes measures $d_1 = 5 \text{ mm}$ ($d_2 = 8 \text{ mm}$) in dose monitor 1 (2). Assuming an average ion mobility μ_{mobil} of $136 \text{ mm}^2/(\text{V s})$ in air (Hörrak et al., 2000) yields an average drift velocity of

$$v_{\text{drift}} = \mu_{\text{mobil}} \frac{U}{d} \quad (2.1)$$

and an average charge collection time of

$$t_{\text{coll}} = \frac{d}{v_{\text{drift}}} = \frac{d^2}{\mu_{\text{mobil}} U}. \quad (2.2)$$

These simple considerations result in average charge collection times of approximately 92 μs for monitor 1 and 235 μs for monitor 2.

Strip monitor

Situated upstream of the vacuum exit window to the patient, a position-sensitive strip monitor serves as the final diagnostic device in the Gantry 2 beamline. It is also filled with ambient air and consists of two anode planes on 1.8 kV separated by a grounded cathode plane – a 20 μm thick Mylar foil coated with 20 nm of aluminum on both sides. The anodes are made of 50 μm thick Kapton[®] foils carrying 17 μm thick copper strips of 2 mm width. The air gap between the cathode and anode planes measures 10 mm yielding an average charge collection time of 408 μs (see equation 2.2). The 88 strips in the T -cathode are oriented perpendicular to the 128 strips in the U -cathode to provide readings of the beam profile in both directions. The measured current of each strip is converted to a frequency and integrated on a TERA 06 board (La Rosa et al., 2008) comprising two 64-channel chips (Mazza et al., 2005). As such, time-resolved sampling of the strip monitor is not supported. Actis et al. (2014) provide a more detailed description of the strip monitor and associated readout technology. The design was taken over by DE.TEC.TOR Devices & Technologies Torino who now offer the device commercially.

2.1.3 Variants of pencil beam scanning

Flanz (2011) defines pencil beam scanning (PBS) as the act of moving a particle beam from one point in the target to another while changing its parameters (e.g. current, energy, position, size). Most implementations of PBS cut the target in iso-energy slices corresponding to identical penetration depths of the beam in water. However, due to density heterogeneities in the beam path and the curvature of the patient's surface, these iso-energy slices can be rather deformed in patient geometry. For every slice or energy setting, the scanner magnets spread the proton beam transversally according to the outline of the target. The treatment plan defines the

fluence distribution to be delivered across the iso-energy slice. Upon completion of a transverse scan, the beam energy is decreased and the next slice is irradiated. By alternating transverse scans and changes in the beam energy, protons can be delivered to the entire target volume.

Beam scanning in the transverse plane comes in mainly three different variants: discrete spot scanning (Pedroni et al., 1995), quasi-continuous raster scanning (Haberer et al., 1993), and fully continuous line scanning (Zenklusen et al., 2010). For experimental purposes, Gantry 2 supports irradiations using any of the three techniques. Implemented at various centers around the world and offered by a number of commercial vendors, spot, raster and line scanning differ in performance due to varying amounts of dead time accumulated during each transverse scan. The main differences are qualitatively summarized in figure 2.2 and in the following three paragraphs. A mathematical description is provided in section 2.2 below.

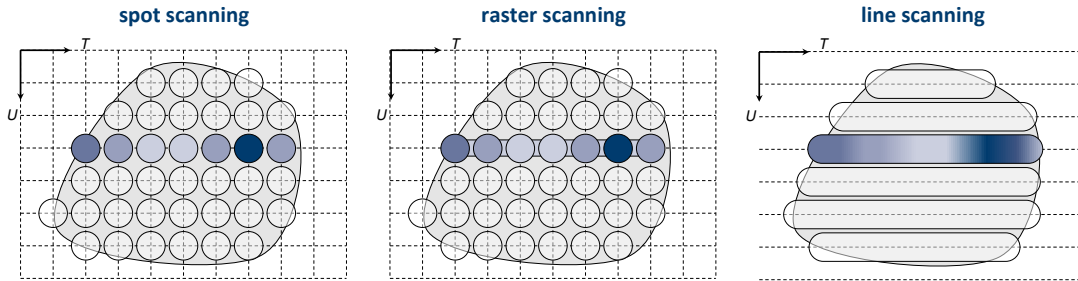


Figure 2.2: Schematic comparison of the three beam delivery techniques: spot scanning (left), raster scanning (center) and line scanning (right). Areas shaded in dark blue correspond to a high concentration of protons, light blue areas indicate a low proton concentration.

Spot scanning

In spot scanning, a rectilinear grid of thousands of discrete pencil beam positions is superimposed onto the target. The grid is regular in homogeneous media but may be deformed in patient anatomy. Every grid point represents a unique combination of beam energy E , transverse T -position, transverse U -position and number of prescribed protons N_p . The Gantry 2 actuators are controlled according to those parameters. The number of protons delivered to each grid point is determined by the local dwell time τ and beam current I :

$$N_p = \frac{1}{e} \int_0^\tau I(t) dt, \quad (2.3)$$

with the elementary charge e . To be robust against fluctuations in the beam current, most installations of spot scanning follow a dose-driven irradiation scheme: The

2 Materials and methods

number of delivered protons N_p is accumulated over time on a running counter and a beam-off command is issued upon reaching the prescribed value. As such, the local dwell time τ can vary dynamically depending on the actual beam current $I(t)$. In the interest of performance, I is maximized during irradiation ($I_{\max} \sim 0.5$ nA) and lowered only for spots prescribed to very low doses ($N_p \lesssim 5 \times 10^5$) using the vertical deflector. The values in brackets are specific to the Gantry 2 scanning system. As depicted in figure 2.2 above, the beam is turned off completely by the kicker magnet when transiting from one grid point to the next. The beam off period is used to analyze retrospectively that the correct amount of protons has been delivered to the correct position. Performing these verification tasks and adjusting the beamline settings according to the next grid point in the iso-energy slice amounts to roughly 3 ms dead time on Gantry 2.

Raster scanning

Raster scanning follows the same grid constraint as spot scanning, but the beam remains on during transitions. Beam-off commands need to be issued only when changing energies or facing large gaps ($\gtrsim 10$ mm) in the transverse scan path. As such, dead time can be minimized at the cost of transient dose contributions between grid points. They have to be taken into account by the treatment planning system and the weights of neighboring grid points have to be reduced accordingly. As in spot scanning, the scan sequence is determined by the amount of locally deposited protons N_p . Actuators change settings upon delivery of N_p . Smaller fluctuations in the beam current I simply shorten or lengthen the dwell time τ without compromising the accuracy of the irradiation.

Line scanning

In contrast to spot and raster scanning, line scanning is a time-driven form of patient irradiation. As shown in table 2.2, the motion of the proton beam along the T -axis is characterized by trajectories based on timestamps t_i as well as nodes for the beam position T_i and current I_i . Consequently, the requirements on stability are much higher than in spot and raster scanning, especially for the beam current.

Table 2.2: Generalized delivery table of a single line scan.

timestamp	T -position	beam current
t_1	T_1	I_1
t_2	T_2	I_2
\vdots	\vdots	\vdots
t_n	T_n	I_n

The beam delivery unit interpolates these tables linearly. Hence, each of the $(n - 1)$ line segments is scanned at constant speed

$$v_i = \frac{|T_{i+1} - T_i|}{t_{i+1} - t_i}. \quad (2.4)$$

The number of protons delivered during each segment is given by

$$N_{p,i} = \frac{(I_{i+1} + I_i)(t_{i+1} - t_i)}{2e} = \frac{(I_{i+1} + I_i)}{2e} \frac{|T_{i+1} - T_i|}{v_i}. \quad (2.5)$$

As such, line scanning is fully continuous in the T -direction with the possibility to modulate the delivered proton fluence through changes in the beam current I and scan speed v . Beam-off commands are issued upon reaching t_n .

2.2 Treatment plan conversion

Discrete and continuous beam scanning result in different transverse fluence profiles. Describing the differences mathematically is important in order to model the response of various detectors to scanned lines. Moreover, the considerations provided in this section allow for calculating dose distributions delivered with raster and line scanning and creating treatment plans for these two techniques similar in quality to optimized spot scanning plans.

In discrete scanning, the proton beam is stationary during beam-on at one fixed location in the (T, U) -plane. Hence, the delivered proton fluence d is only determined by the transverse shape of the beam. In first order approximation, the T and U -dependencies can be decoupled yielding

$$d_{\text{spot}}(T, U) = N_p \eta_T(T) \eta_U(U), \quad (2.6)$$

with the one-dimensional proton density functions η_T and η_U in T and U -direction, respectively. When scanning the beam continuously along straight lines, the dynamics of the irradiation additionally influence the delivered proton fluence. Changes in the scan speed v and beam current I modulate d continuously. These dynamic effects can be characterized by a kernel function κ convolved with the stationary beam shape d_{spot} :

$$d_{\text{line}}(T, U) = (d_{\text{spot}} * \kappa)(T, U) \quad (2.7a)$$

$$\Leftrightarrow d_{\text{line}}(T, U) = \int_{-\infty}^{+\infty} \int_{-\infty}^{+\infty} d_{\text{spot}}(T', U') \kappa(T - T', U - U') dT' dU' \quad (2.7b)$$

As table 2.2 indicates, each line scan is composed of a multitude of segments varying in delivery dynamics. Hence, κ represents the sum of all segment-specific kernel

2 Materials and methods

functions κ_i :

$$\kappa(T - T', U - U') = \sum_{i=1}^{n-1} \kappa_i(T - T', U - U'). \quad (2.8)$$

During the irradiation of each segment, the beam is scanned a certain distance $\Delta T_i = T_{i+1} - T_i$ while the current changes linearly from I_i to I_{i+1} . The modulation of the beam current can be characterized by

$$I_{\text{mod},i}(T - T') = \frac{I_{i+1} - I_i}{\Delta T_i} (T - T') + \frac{I_i + I_{i+1}}{2}, \quad (2.9)$$

such that $I_{\text{mod},i}(-\Delta T_i/2) = I_i$ and $I_{\text{mod},i}(+\Delta T_i/2) = I_{i+1}$. For simplification purposes, it will be convenient to express the modulation of the beam current in relative terms:

$$\iota_i(T - T') := \frac{2}{I_i + I_{i+1}} I_{\text{mod},i}(T - T') = m_i(T - T') + 1, \quad (2.10)$$

with

$$m_i := \frac{2}{\Delta T_i} \frac{I_{i+1} - I_i}{I_{i+1} + I_i}, \quad (2.11)$$

As such, $\iota_i = 1$ for $T = T'$. Because of the fixed boundary conditions of each line segment, the individual kernel functions are given by

$$\kappa_i(T - T', U - U') = \frac{\iota_i(T - T')}{\Delta T_i} \Pi \left(\frac{T - T'}{\Delta T_i} \right) \delta(U - U'), \quad (2.12)$$

where Π denotes the rectangular function

$$\Pi \left(\frac{T - T'}{\Delta T_i} \right) = \begin{cases} 0 & \text{for } |T - T'| > |\Delta T_i/2| \\ 1/2 & \text{for } |T - T'| = |\Delta T_i/2| \\ 1 & \text{for } |T - T'| < |\Delta T_i/2| \end{cases} \quad (2.13)$$

Inserting equation 2.12 in equation 2.7b yields:

$$d_{\text{line}}(T, U) = \eta_U(U) \sum_{i=1}^{n-1} \frac{N_{p,i}}{\Delta T_i} \int_{T-\Delta T_i/2}^{T+\Delta T_i/2} (m_i(T - T') + 1) \eta_T(T') dT'. \quad (2.14)$$

As such

$$d_{\text{line}} \longrightarrow d_{\text{spot}} \quad (n = 2 \text{ and } \Delta T \longrightarrow 0). \quad (2.15)$$

The number of protons $N_{p,i}$ delivered during each segment is stated in equation 2.5 above.

Gaussian beam shape

In case of a Gaussian beam profile, the integral of equation 2.14 can be computed analytically. For demonstration purposes, the following calculation considers a line composed of one single segment only. As such, the scan stretches from T_1 to T_2 and the mid-position is given by

$$\mu_T = \frac{T_1 + T_2}{2}. \quad (2.16)$$

In Gaussian approximation, η_T takes the following form:

$$\eta_T(T) = \frac{1}{\sigma_T \sqrt{2\pi}} \exp \left[-\frac{1}{2} \left(\frac{T - \mu_T}{\sigma_T} \right)^2 \right], \quad (2.17)$$

with the beam size in T -direction σ_T . Evaluating equation 2.14 yields

$$d_{\text{line}}(T, U) = \eta_U(U) \frac{N_p}{\Delta T} \left(\frac{m\sigma_T}{\sqrt{2\pi}} [\exp(-\xi_1^2) - \exp(-\xi_2^2)] + \frac{1}{2} (m(T - \mu_T) + 1) [\text{erf}(\xi_1) - \text{erf}(\xi_2)] \right), \quad (2.18)$$

where

$$\xi_1 \equiv \xi_1(T) := \frac{T - \mu_T + \Delta T/2}{\sigma_T \sqrt{2}} \quad (2.19)$$

and

$$\xi_2 \equiv \xi_2(T) := \frac{T - \mu_T - \Delta T/2}{\sigma_T \sqrt{2}}. \quad (2.20)$$

At constant beam current ($I_1 = I_2$ and $m = 0$), the expression of equation 2.18 simplifies to:

$$d_{\text{line}}(T, U) = \eta_U(U) \frac{N_p}{2\Delta T} [\text{erf}(\xi_1) - \text{erf}(\xi_2)]. \quad (2.21)$$

Fluence matching

The clinical use of the line scanning technique is bound to the constraint that it is able to deliver superior or at least equivalent dose distributions compared to spot scanning irradiations. For demonstration purposes, an experimental plan converter was developed within this dissertation that imports fully optimized spot scanning treatment plans and translates them into deliverable (raster and) line scanning plans of similar quality. In a first step, the converter tool groups discrete beam spots located on identical T -lines and calculates their combined fluence profile:

$$d_{\text{spot,nom}}(T, U) = \sum_{i=1}^n d_{\text{spot},i}. \quad (2.22)$$

2 Materials and methods

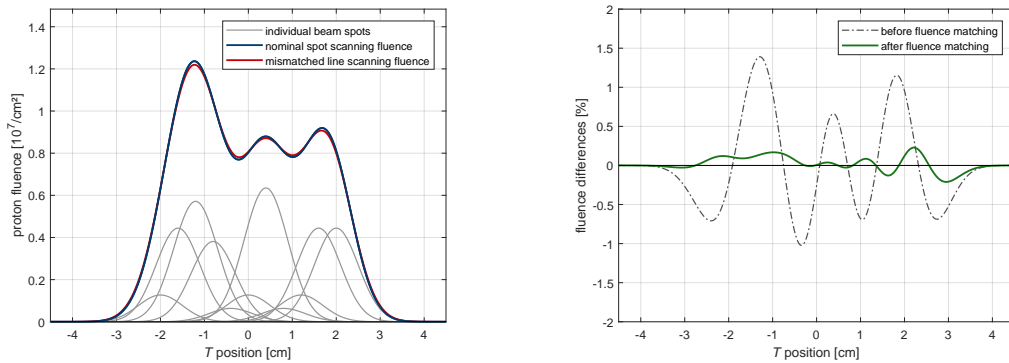
In a second step, the converter assures continuous motion of the proton beam by replacing single spots with line segments that connect the midpoints between two spots. Each segment is assigned a constant beam current I and scan speed v according to the weight of the spot it replaces. In the interest of performance, the beam current is decreased only if $v > v_{\max}$ would be required to lower the delivered number of protons sufficiently. The fluence profile of resulting line segments can be calculated using equation 2.21. Their superposition determines the delivered fluence profile:

$$d_{\text{line,act}}(T, U) = \sum_{i=1}^n d_{\text{line},i}. \quad (2.23)$$

In case of raster scanning, transient dose contributions are computed that arise from moving the proton beam from one grid point to the next using equation 2.21. These transient raster segments must be added to the overall fluence profile yielding

$$d_{\text{raster,act}}(T, U) = \sum_{i=1}^n d_{\text{spot},i} + \sum_{i=1}^n d_{\text{raster},i}. \quad (2.24)$$

In a final step, the converter optimizes the weights of individual line and raster segments in order to match the actual delivered fluence profiles (see equations 2.23 and 2.24) to the nominal one obtained from the spot scanning plan (see equation 2.22). This matching procedure is based on the method of least squares. Its impact is shown in figure 2.3 below. In this example case, the nominal fluence profile is determined by 11 beam spots placed on a 4 mm grid. Fluence matching reduces the deviations between line and spot scanning irradiations from $\pm 1.5\%$ to $\pm 0.3\%$.



(a) In this example, the fluence profile of the spot scanning plan is composed of 11 beam spots spaced 4 mm apart ($E = 151$ MeV).

(b) The differences in the spot and line scanning fluence distributions could be decreased to less than $\pm 0.3\%$ (in air).

Figure 2.3: Illustration of the impact of fluence matching in the treatment plan converter on delivered fluence distributions. When translating spot to line scanning plans, iterative fluence matching helps to reduce differences in the delivered profiles.

Spots with zero weight prescription cause gaps in the scan path. With the help of the vertical deflector, the beam current can be suppressed entirely in those regions. The T -scanner magnet moves with maximum speed across such gaps and the voltage on the deflector plates is decreased again when reaching the next line segment. As such, an interruption of the line can be avoided. The treatment plan converter considers three subsequent line segments without gaps as a continuous T -line. Due to superior precision and performance, lines with less segments are irradiated as discrete beam spots.

2.3 The CCD imaging system

The treatment plan converter and related mathematical models were validated against measurements taken with a high-resolution imaging system assembled by Schätti et al. (2013), which is able to resolve transverse fluence profiles on a sub-millimeter scale. In addition to validation measurements, the imaging system was used to assess the general quality of delivered spot, raster and line scans and quantify interplay patterns in case of target motion. It consists of five main components: (1) an Apogee Alta U6 camera; (2) a Nikon AF Nikkor 50 mm F/1.8 D lens (aperture $f/8$); (3) a mirror tilted 45° ; (4) a scintillating screen and (5) a light-tight sealed housing. The image sensor of the Apogee camera is a 1024×1024 Kodak KAF-1001E charge-coupled device (CCD) with a pixel size of $(24 \times 24) \mu\text{m}^2$ typically operated at -20°C . Exposed to proton beams, the scintillating screen emits light rays which are reflected onto the lens by the tilted mirror. When focused onto the two-dimensional CCD sensor array, these light rays produce a signal proportional to their intensity, which is typically saved in units of pixel counts.

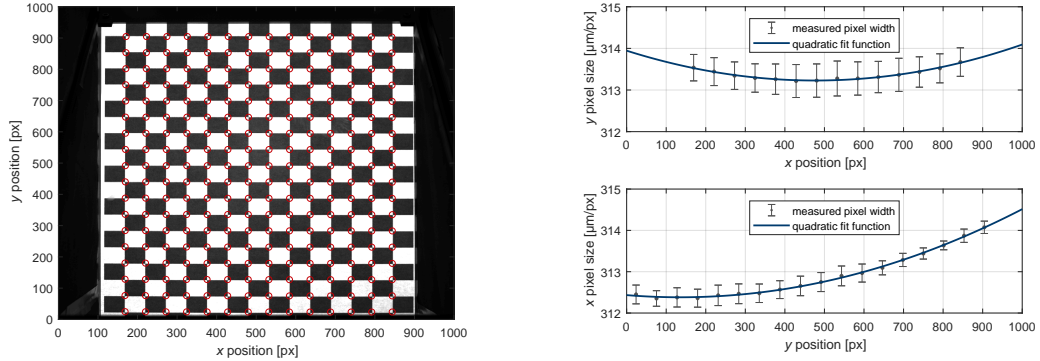
The CCD imaging system was completely recalibrated to meet the high precision requirements arising from the scope of this work. Three main sources of error were identified: geometric and intensity distortions, as well as quenching-related non-linearities. The following three subsections quantify their magnitude and introduce adequate correction algorithms if necessary.

2.3.1 Geometric distortions

Due to the short distance between mirror and lens ($\sim 50\text{ cm}$), one could suspect systematic distortions of acquired images caused by non-linear projections of the CCD pixel array onto the image plane. As a consequence, straight lines may appear curved. To quantify the magnitude of such geometric distortions, the scintillating screen was replaced by a checker board pattern and imaged multiple times (see figure 2.4(a)). The size of each checker board was measured on the image and compared to the nominal value of the print out (16.23 mm). Figure 2.4(b) reveals a position dependence of the pixel size in the image plane. The pixel width in y -direction reaches a minimum at the center of the image, whereas the pixel width in

2 Materials and methods

x -direction increases quadratically from $312.4 \mu\text{m}/\text{px}$ to $314 \mu\text{m}/\text{px}$ along the y -axis. Small deviations from the nominal 45° mirror tilt may explain this observation. The position dependence of the projected pixel size indicates so-called barrel distortions with optical axes around $x = 476.7 \text{ px}$ and $y = 135.3 \text{ px}$ (minima of the quadratic fits). By restricting data acquisition to the lower part of the image ($y < 512 \text{ px}$), their influence could be minimized and corrections became obsolete. Instead, a constant (average) pixel size of $(313 \pm 1) \mu\text{m}$ was assumed across the entire image plane.



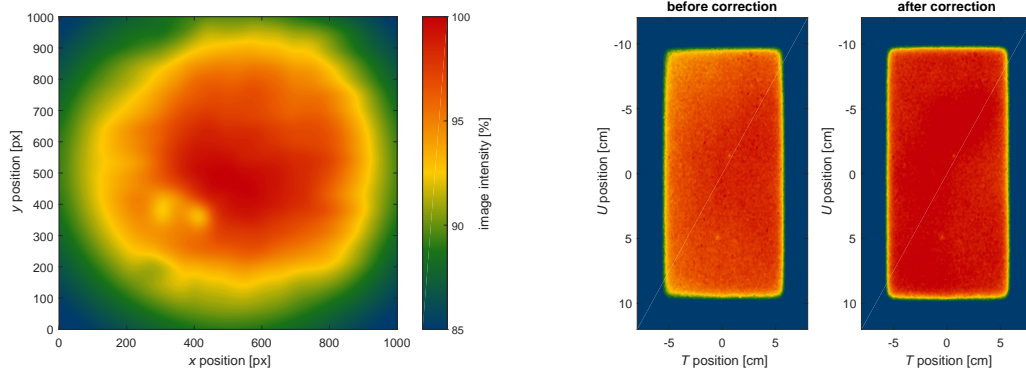
(a) Image of a checker board replacing the scintillating screen. Red circles mark the detected corner points. Their distance on the actual board measures 16.23 mm.

(b) Position dependence of the projected pixel size in x (top) and y -direction (bottom). The quadratic fit lines (blue curves) indicate barrel distortions.

Figure 2.4: Quantification of geometric distortions by imaging a regular checker board of well-known dimensions. Barrel distortions are small in the lower part of the image ($y < 512 \text{ px}$).

2.3.2 Intensity distortions

Lens limitations cause a reduction of the image intensity towards the periphery commonly referred to as optical vignetting. Homogeneous exposure of the lens revealed that this effect can result in up to 15% differences between nominal and actual brightness (see figure 2.5(a)). Measurements were taken via the 45° mirror to include potential reflexions off the housing walls. To compensate for these intensity distortions, every image acquired is background-corrected and divided by the flat-field displayed in figure 2.5(a). The two spots observed in the lower left quadrant of the flat-field originate from impurities on the mirror. Figure 2.5(b) demonstrates the effectiveness of such corrections. The residual intensity variations in a homogeneous $(20 \times 12) \text{ cm}^2$ field (Gantry 2 scan area) are Gaussian distributed after flat-field correction with a width of $\sigma_{\text{int}} = 1.62\%$.



(a) Flat-field of the CCD imaging system including vignetting and mirror impurities (two spots in the lower left quadrant).

(b) Image of a homogeneous fluence distribution before (left) and after (right) flat-field correction.

Figure 2.5: Intensity distortions of the CCD imaging system. Vignetting decreases peripheral brightness by up to 15%. Flat-field corrections can restore homogeneous exposure with residual intensity variations of the order of $\pm 1.62\%$ (Gaussian σ).

2.3.3 Quenching correction

The light output L of the scintillator is proportional to the proton fluence impinging on it. However, it quenches with increasing linear energy transfer (LET). As such, measured depth-dose distributions $D(z, E)$ – products of fluence and LET – will exhibit decreased maxima. Birks' quenching law (Birks, 1951) models this effect:

$$L(z, E) = \frac{q_1(E)D(z, E)}{1 + q_2(E)D(z, E)}, \quad (2.25)$$

with the quenching parameters

$$q_1(E) = q_{1,1}(E/E_{\text{mid}})^2 + q_{1,2}(E/E_{\text{mid}}) + q_{1,3} \quad (2.26)$$

and

$$q_2(E) = q_{2,1}(E/E_{\text{mid}})^2 + q_{2,2}(E/E_{\text{mid}}) + q_{2,3}. \quad (2.27)$$

In order to determine the coefficients $q_{i,j}$ experimentally, the light output L of monoenergetic and homogeneous proton fields was measured in various different water depths and compared to the corresponding integral depth-dose D . For this purpose, varying amounts of poly(methyl methacrylate) (PMMA) were placed on top of the scintillator. Its water-equivalent path length was assumed to be 1.1635 (Lourenço et al., 2017), which is in agreement with a value of 1.165 ± 0.013 reported earlier by Jäkel et al. (2001). The water-equivalent thickness of the housing and scintillator was estimated to be 4 mm. This procedure was executed for eleven different beam energies ranging between 70 MeV and 230 MeV. The results for six of those are displayed in figure 2.6.

2 Materials and methods

Equation 2.25 was fitted to all measured depth-intensity curves simultaneously with $q_{i,j}$ as free fit parameters. Setting $E_{\text{mid}} = 150$ MeV, the optimizer returned the following quenching coefficients:

$$q_{1,1} = +3.24 \times 10^{-6} \text{ counts/nGy} \quad (2.28a)$$

$$q_{1,2} = -3.87 \times 10^{-6} \text{ counts/nGy} \quad (2.28b)$$

$$q_{1,3} = +1.78 \times 10^{-5} \text{ counts/nGy} \quad (2.28c)$$

$$q_{2,1} = +7.26 \times 10^{-2} \text{ protons/(nGy cm}^2\text{)} \quad (2.28d)$$

$$q_{2,2} = -1.01 \times 10^{-1} \text{ protons/(nGy cm}^2\text{)} \quad (2.28e)$$

$$q_{2,3} = +6.01 \times 10^{-2} \text{ protons/(nGy cm}^2\text{)} \quad (2.28f)$$

Resulting depth-intensity curves $L(z, E)$ are shown as solid blue lines in figure 2.6 below. Non-quenched curves ($q_2(E) = 0$) are shown as dashed lines to emphasize the necessity of quenching corrections.

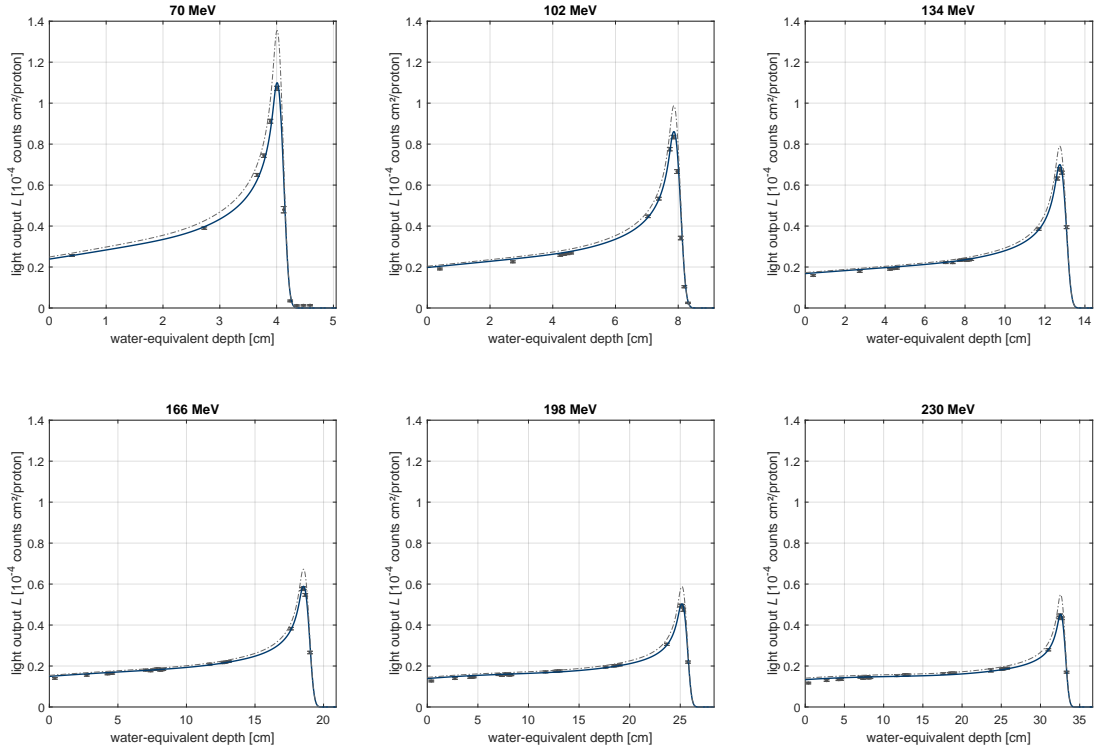


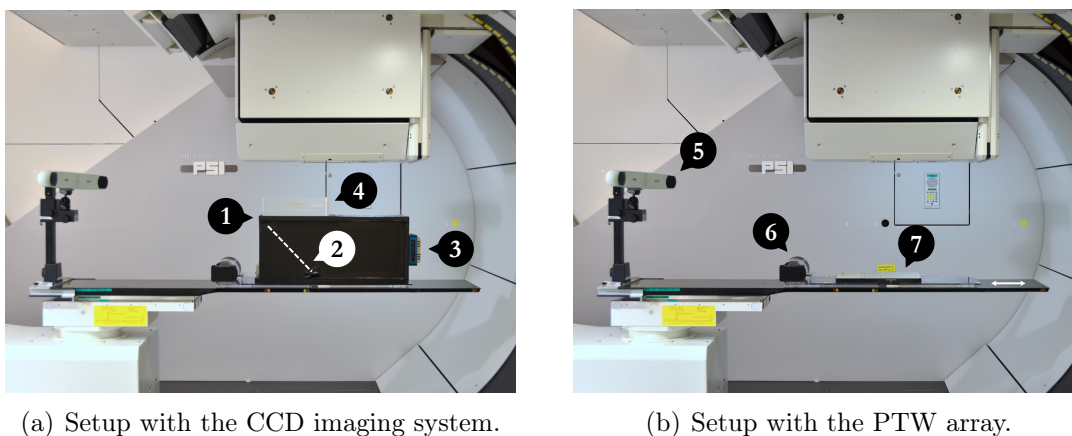
Figure 2.6: Quenching model of the CCD imaging system. The measured light output L is accurately described by Birks' quenching model (solid blue curves). For higher beam energies ($E \gtrsim 200$ MeV), differences in the plateau region arise. Dashed lines represent non-quenched depth-intensity curves ($q_2(E) = 0$).

2.4 Data acquisition and analysis

A substantial amount of work included in this dissertation is of experimental nature. All measurements were conducted on Gantry 2. Acquired data originate from various sources (e.g. machine log files, diagnostic devices, dosimeters). Hall probes, dose monitors and the strip chamber are among the predominantly used diagnostic devices (see section 2.1.2). The dosimeters of choice were the CCD imaging system described in section 2.3 above and a 2D array of vented ionization chambers (PTW *seven29*). The typical experimental setup is described in subsection 2.4.1 and the most important analysis tools are briefly summarized in subsection 2.4.2.

2.4.1 Experimental setup

The CCD imaging system was placed at iso-center whenever high-resolution measurements of the transverse dose profile were required (e.g. validation of plan converter, quantification of interplay effects). The typical setup is depicted in figure 2.7(a). The scintillating screen was aligned at iso-center and PMMA slabs were placed on top of the housing to shift the water-equivalent depth of the imaging plane. To measure absolute dose distributions (in units of Gy), the CCD imaging system was replaced by the PTW *seven29*² as seen in figure 2.7(b).



(a) Setup with the CCD imaging system.

(b) Setup with the PTW array.

Figure 2.7: Typical setup for experiments on Gantry 2 using (a) the CCD imaging system or (b) the PTW array. The circle numbers represent: ① the scintillating screen of the CCD imaging system aligned at iso-center; ② the mirror tilted 45°; ③ the air-cooled CCD camera; ④ slabs of PMMA to shift the water-equivalent depth; ⑤ the optical tracking system interfaced to the TDS; ⑥ the motor of the sliding QUASAR™ table; ⑦ the PTW ionization chamber array *seven29*.

²The two-dimensional array consists of 27×27 individual ionization chambers, each of which has a sensitive volume of $(5 \times 5 \times 5) \text{ mm}^3$. The center of individual chambers is placed on a regular $(1 \times 1) \text{ cm}^2$ grid.

An output-scaling factor of 2% was applied to all measured doses to correct for systematic deviations from the treatment plan (Pedroni et al., 2005). Both dosimeters could be moved along one axis when placed on the QUASAR™ Respiratory Motion Platform. An optical tracking system (Fattori et al., 2017) was installed to record the iso-center motion and synchronize the irradiation precisely to any chosen starting phase.

2.4.2 Data analysis tools

All data were analyzed in MATLAB® version R2015b or later (MATLAB, 2015). Fits and models are based on the method of least squares. Statistical significance was determined using the analysis of variance in combination with paired *t*-tests. Dose distributions were evaluated according to clinical metrics derived from dose-volume-histograms and two-dimensional γ -analyses (Low et al., 1998).

3

A beam monitoring and validation system for continuous line scanning in proton therapy

**G. Klimpki^a, S. Psoroulas^a, C. Bula^a, U. Rechsteiner^a, M. Eichin^a,
D.C. Weber^{a,b}, A. Lomax^a, D. Meer^a**

^a Paul Scherrer Institute (PSI), Center for Proton Therapy,
5232 Villigen PSI, Switzerland

^b University of Zurich, UniversityHospital,
Rämistrasse 100, 8091 Zurich, Switzerland

Physics in Medicine and Biology **62** (2017) 6126–6143
submitted on February 09 (2017) and published on July 12 (2017)

preprint

Abstract

Line scanning represents a faster and potentially more flexible form of pencil beam scanning than conventional *step-and-shoot* irradiations. Combined with fast energy changes (~ 100 ms), it could enable time-efficient treatments of mobile targets under repetitive or interruptive motion mitigation techniques (e.g. rescanning, gating, breath-hold). Our second generation proton gantry features irradiations in line scanning mode, but it still lacks a dedicated monitoring and validation system that guarantees patient safety throughout beam delivery. We report on its design and implementation in this paper.

In line scanning, we steer the proton beam continuously along straight lines while adapting the speed and/or current frequently to modulate the delivered dose. We intend to prevent delivery errors that could be clinically relevant through a two-stage system: Safety level 1 monitors the beam current and position every $10\ \mu\text{s}$. We demonstrate that direct readings from Hall probes in the scanner magnets and dose monitors in the gantry nozzle provide required information. Interlocks will be raised when measured signals exceed their predefined tolerance bands. Even in case of an erroneous delivery, safety level 1 restricts hot and cold spots of the physically delivered fraction dose to $\pm 36\ \text{mGy}$ ($\pm 2\%$ of $2\ \text{Gy}$ biologically). In safety level 2 – an additional, partly redundant validation step – we compare the integral line profile measured with a strip monitor in the nozzle to a forward-calculated prediction. The comparison is performed between two line applications to detect amplifying inaccuracies in speed and current modulation. This level can be regarded as an online quality assurance of the machine.

Both safety levels use devices and functionalities already installed along the beamline. Hence, the presented monitoring and validation system preserves full compatibility of discrete and continuous delivery mode on a single gantry, with the possibility to switch between modes during field application.

3.1 Introduction

Proton therapy currently experiences a transition from utilizing passively scattered to actively scanned beams (Meer and Psoroulas, 2015). The former technique irradiates the entire tumor volume nearly simultaneously, while the latter successively scans the beam in all three dimensions. This process requires (1) adapting the energy of the protons to cover the entire depth of the tumor and (2) deflecting them to scan over its lateral extent. Almost all clinically operating centers conduct active scanning in a discretized *step-and-shoot* fashion. Studies by Phillips et al. (1992) or Bert et al. (2008) showed that the time structure of such a scan interferes with the motion of the target yielding deteriorated dose distributions. Hence, the use of active scanning is currently restricted to relatively immobile target volumes (Bert and Durante, 2011).

Faster scanning – analogous to the *sliding window* approach introduced by Brahme (1988) and Convery and Rosenbloom (1992) – would open up the possibility to efficiently treat tumors under various motion mitigation techniques. Especially the combinations of rescanning and gating or rescanning and breath-hold add substantial dead-time to the treatment and, thus, call for fast, yet flexible ways to deliver protons to the tumor. Pedroni et al. (2011) and Safai et al. (2012) reported on a cyclotron-fed proton gantry that meets this demand: It features energy switching times of about 100 ms, fast lateral scan speeds of up to 2 cm/ms and two modes of operation – discrete scanning (Pedroni et al., 1995) and continuous line scanning (Zenklusen et al., 2010; Inoue, 2014). Both of them make use of the short energy switching time, but only line scanning is dedicated to continuous lateral scanning.

The gantry operates clinically since 2013 in discrete scanning mode. Eventual clinical operation in line scanning mode requires a suitable beam monitoring system to ensure safe irradiation of the patient at the level of discrete scanning. Given the dynamic and continuously varying delivery parameters of line scanning mode, this amounts to a non-trivial problem. In this publication, therefore, we report on the conceptual design and technical implementation of a clinically acceptable monitoring strategy for continuous line scanning. By doing so, we wish to answer the following principal questions:

- How can we safely monitor dose during beam delivery?
- Do additional monitoring requirements arise from the continuous and dynamic character of line scanning?
- Are dedicated hardware elements required to ensure effective monitoring of line scanning?

In answering these questions, we have followed the guidelines and recommendation given by the International Commission on Radiation Units and Measurements (2007) and the International Electrotechnical Commission (2014).

3.2 Materials and methods

3.2.1 Beam delivery modes

Gantry 2 at the Paul Scherrer Institute can operate in both discrete and continuous line scanning mode. In both cases, protons are distributed throughout the entire tumor volume by (1) adjusting the beam energy E step-wise (scanning in depth) and (2) by deflecting the beam laterally using scanner magnets. As such, discrete and continuous scanning differ in the mode of lateral deflection only. For both forms of beam delivery, usable beam energies range between 70 and 230 MeV and the maximum field dimension measures $(12 \times 20) \text{ cm}^2$ (in the $T \times U$ directions respectively following our nomenclature¹).

Discrete scanning

With discrete scanning, we refer to a dose-driven form of proton pencil beam scanning based on a discrete, rectilinear scan grid (see upper part of figure 3.1). As such, the beam is turned only on at fixed grid points. When the prescribed number of protons N_p has been applied, a beam-off command is issued that deflects the beam far upstream to prevent it from passing through the beamline. The settings of the scanner magnets change according to the subsequent spot position (roughly 3 ms of dead time). The transition period is also used to validate the position of the delivered beam spot in the (T, U) plane. This *step-and-shoot* process is repeated until all spots with identical beam energy have been delivered. To cover the entire tumor extent in depth, multiples of such iso-energy layers have to be applied.

Line scanning

Line scanning is a continuous and time-driven form of delivery. As such, lateral scanning is discretized in only one dimension (here U) and quasi-continuous in the other (here T) (see lower part of figure 3.1). Modulating the number of delivered protons along T is achieved by quickly changing the scan speed v and/or beam current I . For this purpose, the machine steering files contain separated time tables for the T position and beam current with minimal time steps of $10 \mu\text{s}$. Both tables are limited to 512 entries due to restricted memory capacity. The control system interpolates them linearly, which yields constant scan speeds between two specified T positions. The flexibility in adapting the beam current while scanning lines allows for lowering the delivered dose even further when scanning at maximum speed. Beam-off commands are only issued after a complete line has been applied to allow for changes in U position and/or beam energy. Although the mode of delivery of line scanning along the T direction is different to that of discrete scanning, the

¹For coplanar treatments under a gantry angle of $\alpha = 0^\circ$, the T and U axes coincide with the transverse and longitudinal axes of the coronal plane.

measured dose distributions in figure 3.1 indicate that, at least at a qualitative level, both modes deliver equivalent profiles along this axis.

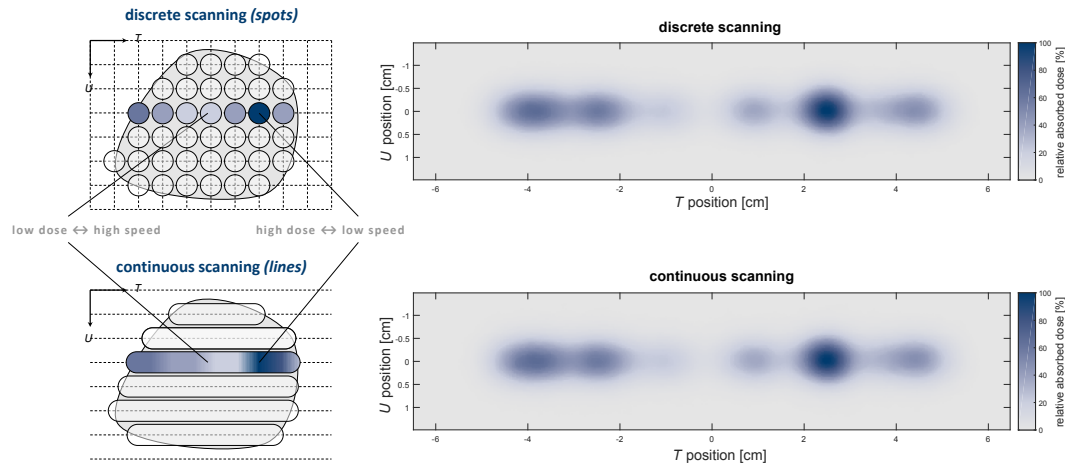


Figure 3.1: In discrete scanning, the proton beam is steered to fixed positions on the scan grid. The irradiation is stationary and a beam-off command is issued as soon as the number of prescribed protons per beam spot is reached. Dark blue spots in the upper left schematic represent spots that receive a high number of protons. In continuous line scanning, the proton beam is scanned along straight lines while quickly modulating the scan speed and/or beam current (lower left schematic). The two relative dose distributions (upper right and lower right plot) show slices in the lateral (T, U) plane acquired with the CCD imaging system (screen placed in air at iso-center). A total number of 2.7×10^8 protons was delivered in both discrete and continuous scanning mode ($E = 150$ MeV). For the former, dose modulation was achieved by superimposing 41 equally spaced spots of different weight; for the latter, scan speed and beam current were adapted while scanning from $(T_1, U) = (-5, 0)$ cm to $(T_2, U) = (+5, 0)$ cm. Both dose distributions were normalized to the maximum light output of the discrete scanning measurement.

3.2.2 Beam monitoring requirements

All considerations on monitoring requirements for line scanning are based on the fundamental assumption that this delivery mode operates precisely and accurately. However, errors to be detected by the monitoring system can occur at any time, even though their probability is very low (less than once per treatment under normal operation conditions). The task of the monitoring system then is to detect unforeseen delivery inaccuracies, which yield significant dosimetric fluctuations, fast and reliably. All systematic over- or underdosages as well as all systematic position offsets must be corrected prior to patient irradiation (quality assurance, plan verification etc.).

The guidelines and recommendations given by the International Commission on Radiation Units and Measurements (2007) and the International Electrotechnical Commission (2014) specify that delivery-related errors during a single fraction should not cause hot or cold spots larger than $\pm 2\%$ of the fraction dose (typically 2 Gy(RBE) and 1.8 Gy physical dose). Delivery errors of this magnitude are expected to have no significant impact on the clinical outcome of the treatment, provided that all other fractions will be (or have been) delivered correctly. The French Nuclear Safety Authority (2010) would classify such errors as grade one radiation events. Based on our experience with treatments in discrete scanning mode, we estimate radiation events to occur randomly and less than once per treatment. Thus, the constraint for a dose error in a single line can be set to $\pm 2\%$ of the fraction dose or ± 36 mGy physically.

To translate this constraint to requirements and margins for the line scanning monitoring system, we identified three features that are unique to this delivery mode:

1. Line scanning introduces fewer beam-off intervals than discrete scanning because of its continuous and uninterrupted scan sequences in T direction.
2. Changes of scanning speed and beam current during the delivery of a single line can be exceptionally high (e.g. changes from zero to maximum current in 100 μ s).
3. The delivery is time-driven and, therefore, relies on an accurate response of both scanner magnets and the beam current regulator.

In our opinion, these three features necessitate supervising the beam current and its position at iso-center frequently during the application of a line to ensure that all possible errors are harmless for the patient. For this purpose, we designed a two-level monitoring system for continuous line scanning on Gantry 2, depicted in figure 3.2. Both levels are connected to the patient safety system and able to issue interlocks whenever an unsafe state has been detected. Depending on the source of the interlock, the treatment will either be aborted (level 1) or paused (level 2). In addition, however, and in order to resume the treatment correctly after all errors have been resolved, instantaneous values of beam position and current must be logged at the time of the interlock.

Level 1 (real-time monitoring)

Safety level 1 is active *during* beam-on, hence while a line is being applied, to prevent grade two radiation incidents (French Nuclear Safety Authority, 2010). To guarantee short reaction times even when beam-off intervals are less frequent (see line scanning feature 1), monitors in the gantry nozzle and sweeper magnets are read out in real-time (see subsection 3.2.3 below). Data are sampled every 10 μ s, saved in logging tables and compared in hardware against predefined tolerances. If they are outside

these, interlocks are raised and the patient safety system is informed. This design allows for a fast, decoupled supervision of speed and intensity modulation within safety level 1 (see line scanning feature 2). To guarantee sufficient homogeneity of the delivered dose distribution, the beam position should be within ± 1.5 mm of its prescription at any time. Due to an energy-dependent signal of the dose monitor, the tolerance for the beam current is energy dependent, too. The reaction time for detecting errors in the beam current is, however, universal and should be below 2.5 ms – the time it takes to deliver 36 mGy to a standard treatment planning voxel² placed in the Bragg peak of a proton beam at maximum, authorized current. These margins are in agreement with our present implementation for discrete scanning treatments on Gantry 1 and Gantry 2.

Level 2 (online monitoring)

Safety level 2 is active *after* the complete delivery of a single T line (e.g. in between the application of two lines). As such, a strip monitor in the gantry nozzle measures integral dose profiles in both T and U directions (see subsection 3.2.3 below), with the shape of the T profile being determined by the combined effects of scanning speed and intensity modulation. In this regard, safety level 2 is partly redundant to safety level 1, but relies on a different, independent monitor. Furthermore, safety level 2 is capable of detecting small errors of individual actuators that amplify dosimetrically, e.g. combination of a slightly higher beam current together with a slightly slower scan speed can yield a considerable increase in the delivered fluence (see line scanning feature 3). On completion of a line, the recorded T profile is compared to a forward-calculated prediction (described in detail in subsection 3.2.4 below). For the U profile, a simple position and width check is sufficient. Interlocks are raised whenever any tolerances defined for the comparison remain unsatisfied.

3.2.3 Gantry 2 beam monitors

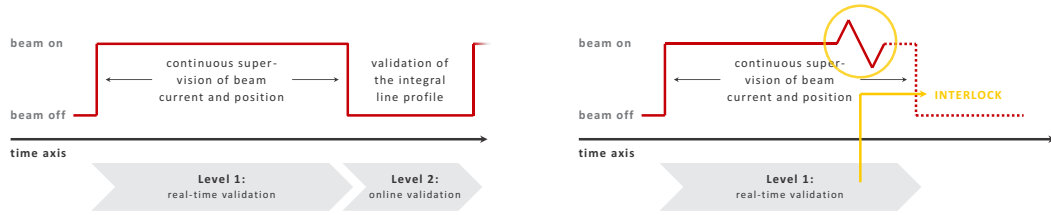
For clinically controlling the delivered beam in discrete scanning mode, the following monitoring devices have been installed in Gantry 2. It is our intention to use the same monitors also for the supervision of line scanning.

Hall probes

The magnetic field strength of the scanner magnets determines the lateral beam position in the (T, U) plane: the larger the magnitude of the field, the larger the deflection towards the edges of the plane. This direct correlation allows for monitoring the actual beam position at iso-center by measuring the magnetic field inside the scanner magnets. For this purpose, both scanner magnets on Gantry 2 are equipped with commercially available, type A Hall probes from SENIS. They measure the

²Our standard treatment planning voxel has a lateral extent of (4.0×4.0) mm² and an extent in depth of 2.5 mm.

3 A beam monitoring and validation system for line scanning



(a) Irradiation of a line *without* interlock.

(b) Irradiation of a line *with* interlock.

Figure 3.2: Flowcharts of the line scanning monitoring and validation system. During beam-on, information on beam current and position are continuously sampled (every 10 μs) to prevent grade two radiation incidents in case of erroneous delivery. Interlocks are raised as soon as predefined tolerances are exceeded. This real-time validation (safety level 1) is followed by an online validation, performed between the application of two lines (e.g. when the U and/or energy changes). This second safety level validates the accuracy of the delivery by comparing measured dose profiles to a forward-calculated prediction. Interlocks can again be raised if metrics of comparison remain unsatisfied.

magnetic field utilizing an integrated single-chip. The measurement range for the Hall probe in the T scanner magnet spans $\pm 0.2\text{ T}$; the one for the Hall probe in the U scanner magnet spans $\pm 0.4\text{ T}$. The noise on both probes translates into a position error of less than 10 μm . Both Hall probes are equipped with real-time readout functionality (sampled every 10 μs).

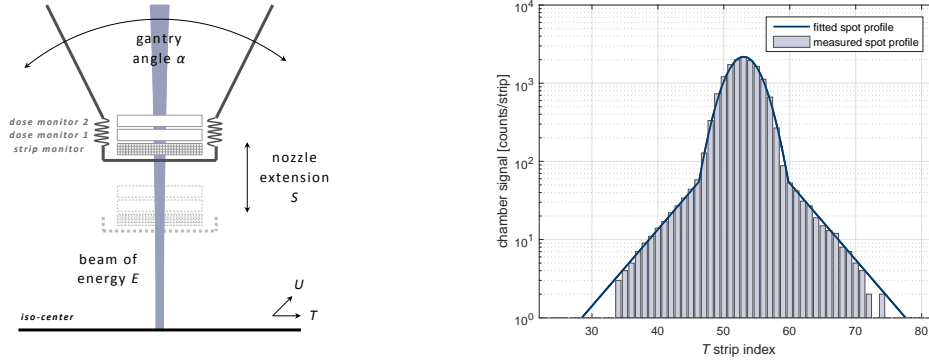
Dose monitors

The Gantry 2 nozzle contains two parallel plate ionization chambers, which will be referred to as dose monitors 1 and 2 in the following (see figure 3.3(a)). Their performance has been investigated by Lin et al. (2009). Both dose monitors are filled with air at ambient temperature and pressure and operate in proportional counting mode (2 kV chamber voltage). The distance between the cathode and anode planes measures 5 mm (8 mm) in dose monitor 1 (2), which results in a maximum charge collection time of approximately 90 μs (240 μs). Dose monitors and Hall probes are synchronized in their real-time readout.

Strip monitor

The final diagnostic device in the Gantry 2 beamline is a position-sensitive strip monitor. It measures integrated dose profiles in T and U direction for every line. This monitor is also filled with ambient air and consists of two cathode planes on 1.8 kV separated by a grounded anode plane. The T cathode carries 88 Copper strips of 2 mm width, whereas the U cathode carries 128 perpendicularly oriented strips. The measured current of each strip is integrated on a TERA 06 board (La Rosa et al., 2008) comprising two 64-channel chips (Mazza et al., 2005). Actis et al.

(2014) provide a more detailed description of the strip monitor and its readout. The design was commercialized by DE.TEC.TOR Devices & Technologies Torino.



(a) Schematic of the Gantry 2 nozzle. Specifications and descriptions of the three monitors (dose 1, dose 2 and strip) are given in subsection 3.2.3.

(b) Exemplary fit for a static spot profile recorded with the strip monitor ($\alpha = 0^\circ$, $E = 90$ MeV, $S = 7.5$ cm, $T = 2$ cm and $U = 8$ cm).

Figure 3.3: The shape of the pencil beam – measured with the strip monitor in the Gantry 2 nozzle – depends on five parameters (α, E, S, T, U). Their meaning is explained in the left schematic. To model mutual dependencies, we fitted the response function of the strip monitor (see equation 3.15) to 52,360 individual spot profiles covering the entire parameter space and saved all fit parameters in a five-dimensional look-up table. The right plot displays an exemplary fit. For each configuration of (α, E, S, T, U), we can interpolate the look-up table smoothly using the method presented in subsection 3.2.4.

3.2.4 Line profile prediction

A key aspect of safety level 2 monitoring, as described in subsection 3.2.2 above, is the ability to accurately predict the profiles of individual lines as they will be recorded in the strip monitor. Two factors will affect this prediction: (1) the cumulative dose in the strip monitor elements resulting from the correct delivery of a modulated line and (2) the lateral beam shape in the nozzle, which can vary as a function of gantry angle α , beam energy E , nozzle extension S as well as T and U position. As such, a mathematical formulation of the line scanning process and beam width variations has to be developed, as described in detail in the following subsection.

Line scanning model

In describing the line scanning process mathematically, we follow the concepts introduced by Trofimov and Bortfeld (2003). The basis of this description is the shape of the proton pencil beam in the lateral (T, U) plane – denoted as $B(T, U)$. The two-dimensional proton distribution (or density) $n(T, U)$ is given by the convolution

3 A beam monitoring and validation system for line scanning

of B with the kernel function κ , which is specific to the scan mode:

$$n(T, U) = N_p(B * \kappa)(T, U) \quad (3.1a)$$

$$\Leftrightarrow n(T, U) = N_p \int_{-\infty}^{+\infty} \int_{-\infty}^{+\infty} B(T', U') \kappa(T - T', U - U') dT' dU' \quad (3.1b)$$

Delivery in line scanning mode is based on time tables for the T position and beam current of the form³

$$\{(t_1 = 0, T_1), \dots, (t_n, T_n)\} \text{ and } \{(t_1 = 0, I_1), \dots, (t_n, I_n)\} \quad (3.2)$$

In other words, the beam is steered over a distance $\Delta T = T_{i+1} - T_i$ during the time interval $\Delta t = t_{i+1} - t_i$. While scanning, the beam current may change linearly from I_i to I_{i+1} . The total number of delivered protons during the scan from (T_i, U) to (T_{i+1}, U) is given by

$$N_p = \frac{(I_{i+1} + I_i)\Delta t}{2e}, \quad (3.3)$$

where e is the elementary charge. We characterize the modulation of the beam current by

$$\iota(T - T') = \frac{2}{\Delta T} \frac{I_{i+1} - I_i}{I_{i+1} + I_i} (T - T') + 1, \quad (3.4)$$

such that $\iota = 1$ for $T = T'$. The kernel function is given by

$$\kappa_{\text{line}}(T - T', U - U') = \frac{\iota(T - T')}{\Delta T} \Pi\left(\frac{T - T'}{\Delta T}\right) \delta(U - U'), \quad (3.5)$$

where Π denotes the rectangular function, which yields a 2D proton distribution of

$$n_{\text{line}}(T, U) = \frac{N_p}{\Delta T} \int_{T-\Delta T/2}^{T+\Delta T/2} \iota(T - T') B(T', U) dT'. \quad (3.6)$$

Beam shape parameterization

During treatments, we measure the shape of the proton pencil beam B with the strip monitor (see figure 3.3(a)). Since this monitor is located in the nozzle plane (and not at iso-center, where the patient is positioned), B depends on the following five parameters: gantry angle α , beam energy E , nozzle extension S as well as T and U position. These dependencies are specific to our upstream scanning gantry design and we model them by interpolating within a five-dimensional look-up table.

³Note that the time steps of the position and current table are independent of one another. However, one can always define small segments with constant scan speed and linear beam current modulation when merging the two tables.

We can generalize this interpolation method to a k -dimensional space. ξ_i shall refer to individual data points (scalars) characterizing the beam shape function and \mathbf{x} is the position vector of that k -dimensional space. We construct the interpolating function $f_k(\mathbf{x}, \boldsymbol{\lambda})$ from permutations of the entries of \mathbf{x} weighted by 2^k scalar coefficients λ_i . We would like to clarify this definition based on three examples:

$$f_{k=1}(\mathbf{x}, \boldsymbol{\lambda}) = \lambda_0 + \lambda_1 x_1 \quad (3.7a)$$

$$f_{k=2}(\mathbf{x}, \boldsymbol{\lambda}) = \lambda_0 + \lambda_1 x_1 + \lambda_2 x_2 + \lambda_3 x_1 x_2 \quad (3.7b)$$

$$f_{k=3}(\mathbf{x}, \boldsymbol{\lambda}) = \lambda_0 + \lambda_1 x_1 + \lambda_2 x_2 + \lambda_3 x_3 + \lambda_4 x_1 x_2 + \lambda_5 x_1 x_3 + \lambda_6 x_2 x_3 + \lambda_7 x_1 x_2 x_3 \quad (3.7c)$$

This interpolating function is continuous and differentiable. The determination of coefficients λ_i will be demonstrated for the exemplary case of $k = 2$. The formalism is analogous for all other dimension:

- In the first step, one needs to identify all 2^k data points ξ_i surrounding the position \mathbf{x} , for which the interpolation is to be conducted. This necessitates finding the upper and lower bounds in each dimension that correspond to those neighboring data points:

$$\ell_{x_1} \leq x_1 \leq u_{x_1} \text{ and } \ell_{x_2} \leq x_2 \leq u_{x_2}, \quad (3.8)$$

- In the second step, f_k is evaluated for each combination of upper and lower bounds:

$$f_{k=2}(\mathbf{x} = \{u_{x_1}, u_{x_2}\}, \boldsymbol{\lambda}) = \xi_1 \quad (3.9a)$$

$$f_{k=2}(\mathbf{x} = \{u_{x_1}, \ell_{x_2}\}, \boldsymbol{\lambda}) = \xi_2 \quad (3.9b)$$

$$f_{k=2}(\mathbf{x} = \{\ell_{x_1}, u_{x_2}\}, \boldsymbol{\lambda}) = \xi_3 \quad (3.9c)$$

$$f_{k=2}(\mathbf{x} = \{\ell_{x_1}, \ell_{x_2}\}, \boldsymbol{\lambda}) = \xi_4 \quad (3.9d)$$

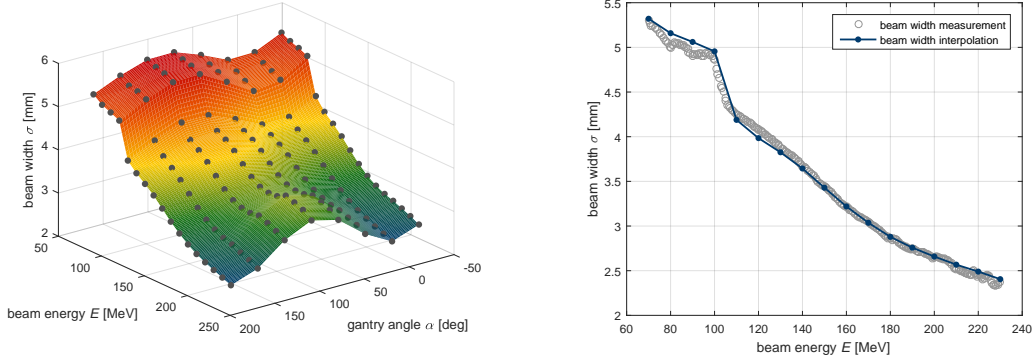
- The coefficient vector can then be calculated in the final step via

$$\boldsymbol{\lambda} = \mathcal{P}^{-1} \boldsymbol{\xi}, \quad (3.10)$$

with the matrix of permuted bounds

$$\mathcal{P} = \begin{pmatrix} 1 & u_{x_1} & u_{x_2} & u_{x_1} u_{x_2} \\ 1 & u_{x_1} & \ell_{x_2} & u_{x_1} \ell_{x_2} \\ 1 & \ell_{x_1} & u_{x_2} & \ell_{x_1} u_{x_2} \\ 1 & \ell_{x_1} & \ell_{x_2} & \ell_{x_1} \ell_{x_2} \end{pmatrix}. \quad (3.11)$$

Figure 3.4 shows an exemplary interpolation surface for measured pencil beam widths in the nozzle plane. The gray data points are smoothly connected by $f_{k=2}(\mathbf{x} = \{\alpha, E\}, \boldsymbol{\lambda})$. It also shows a comparison of measured and interpolated beam widths for the entire range of therapeutic energies.



(a) Two-dimensional surface interpolating the pencil beam width measured with the nozzle strip monitor for $(S, T, U) = (1, 0, 0)$ cm. Displayed data points are stored in the five-dimensional look-up table.

(b) Interpolated (blue line) and measured beam width (gray circles) in the nozzle plane as a function of beam energy for $\alpha = 0^\circ$ and $(S, T, U) = (1, 0, 0)$ cm. Blue dots represent look-up table data points.

Figure 3.4: The beam width measured in the nozzle plane depends on five parameters: gantry angle α , beam energy E , nozzle extension S as well as T and U position. The dependencies are coupled. Our suggested interpolation method is smooth in all these five dimensions. Note that the beam width σ decreases towards iso-center and measures roughly 95% of the one presented here.

3.2.5 Metrics for line profile comparison

The comparison of measured and predicted line profiles in the T direction shall ensure that the overall dose, position and modulation of the line are within acceptable tolerance. In our opinion, the following metrics of comparison are suitable measures to fulfill this aim: integral counts D_{tot} , center of gravity (COG) T_{COG} , line symmetry S , coefficient of determination R^2 and the pass rate of a one-dimensional γ -analysis P_γ (Low et al., 1998). They are defined as:

$$D_{\text{tot}} = \sum_{i=1}^{N_{\text{strips}}} d_i \quad (3.12a)$$

$$T_{\text{COG}} = \sum_{i=1}^{N_{\text{strips}}} i d_i / D_{\text{tot}} \quad (3.12b)$$

$$S = (D_{\text{left}} - D_{\text{right}}) / (D_{\text{left}} + D_{\text{right}}) \quad (3.12c)$$

$$R^2 = 1 - \sum_{i=1}^{N_{\text{strips}}} (d_i - \hat{d}_i)^2 / \sum_{i=1}^{N_{\text{strips}}} (d_i - D_{\text{tot}}/N_{\text{strips}})^2 \quad (3.12d)$$

$$\gamma_i = \min_j \left\{ \sqrt{(d_i - \hat{d}_j)^2 / \varepsilon^2 + (T_i - \hat{T}_j)^2 / \rho^2} \right\} \quad (3.12e)$$

$$P_\gamma = \dim\{\gamma \mid \gamma_i \leq 1\} / N_{\text{strips}}, \quad (3.12f)$$

where d_i refers to measured and \hat{d}_i to predicted strip counts. D_{left} and D_{right} denote the integrated strip counts on each side of the profile about the COG position. Lines scanned in T direction appear as spot-like profiles in the U plane of the strip monitor. Hence, we chose to simply assess their width and position using root-mean-squared (RMS) σ_{RMS} and COG U_{COG} , respectively. The RMS is defined as

$$\sigma_{\text{RMS}}^2 = \sum_{i=1}^{N_{\text{strips}}} i^2 d_i / D_{\text{tot}} - U_{\text{COG}}^2. \quad (3.13)$$

3.2.6 Dose measurements at iso-center

In order to test the reliability of the beam monitoring strategy described above, various dose profiles, for both nominal and well-defined error scenarios, have been directly measured at iso-center. For this, we used the imaging system assembled by Schätti et al. (2013) to (qualitatively) record dose distributions at iso-center (see figure 3.1). It consists of three main components: (1) a scintillating screen, (2) a mirror tilted 45° and (3) a camera with a charge-coupled device (CCD) image sensor. The spatial resolution of the imaging system at the image plane (scintillating screen) was measured to be $(313 \pm 1) \mu\text{m}$. Images acquired with the CCD camera were processed using version 1.49q of the public domain Java program ImageJ (Schneider et al., 2012). All offline data analysis was performed in MATLAB[®] R2015b with the help of the curve fitting and optimization toolboxes (MATLAB, 2015).

3.3 Experiments and results

Presented data originate from a prototype installation of the beam monitoring and validation system. Its design is outlined in subsection 3.2.2. The principle of operation is illustrated by monitoring the application of an exemplary line.

3.3.1 Safety level 1

Example case

Figure 3.5 shows measured signals and predefined tolerance bands for both Hall probes and dose monitors during the application of an example line. The tolerance bands are calculated by the control system prior to irradiation based on the information contained in the delivery tables (see equation 3.2). We observed that direct, unfiltered signals from the dose monitors and Hall probes are accurate enough to supervise the beam current and position. In this example with 150 MeV beam energy, the tolerance for the instantaneous beam current (direct signal of dose monitor 1) was set to $\pm 40 \text{ pA}$, which is equivalent to $\pm 2.5 \times 10^5$ protons per ms. In addition, we allow a reaction time lag of $\pm 2.5 \text{ ms}$ in the tolerance bands. The resulting upper and

3 A beam monitoring and validation system for line scanning

lower limits were satisfied throughout the entire scan of the line. The corresponding dose distribution at iso-center delivered by this line is displayed in figure 3.1.

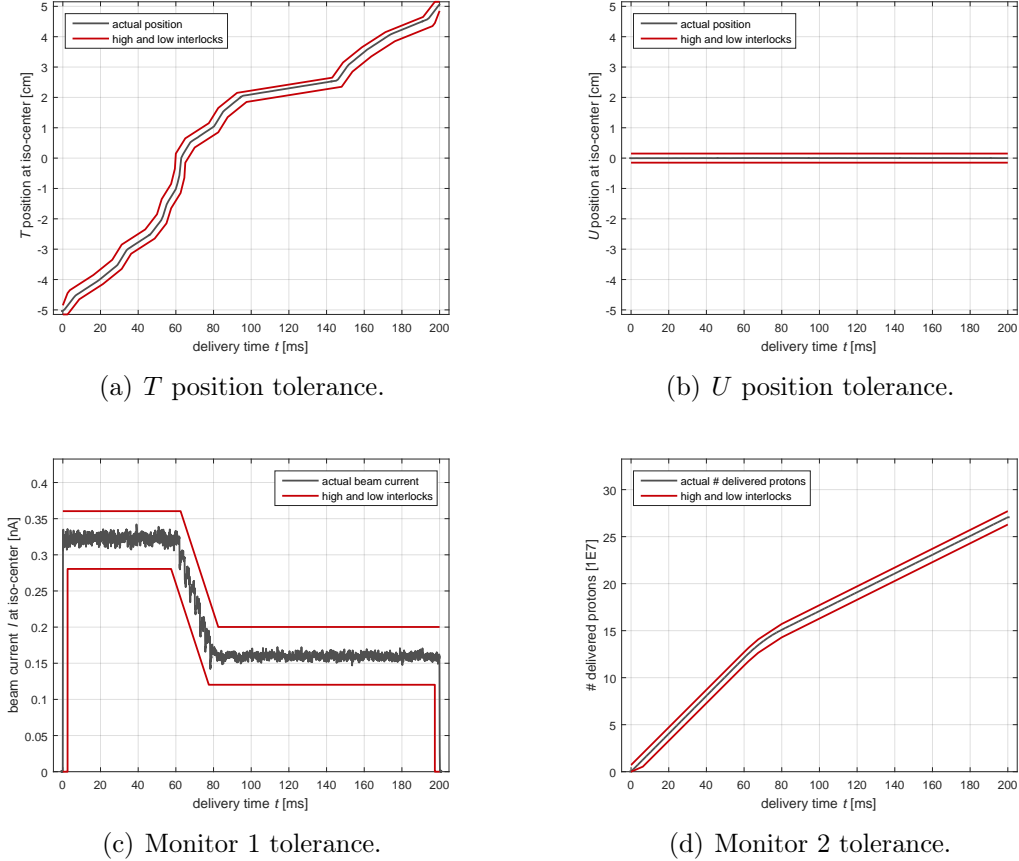


Figure 3.5: Tolerance bands for the beam position (upper plots) and beam current (lower plots) at iso-center. The tolerance for the T and U position measures ± 1.5 mm. Additional time lags of ± 2.5 ms are introduced to allow for marginal latencies of the scanner magnets when changing the scan speed drastically (e.g. at $t = 145.5$ ms in the upper left plot). A systematic shift of the line of $+1.0$ mm in T direction and -1.9 mm in U direction was applied to match the given tolerances. An identical procedure is also applied to all discrete scanning plans before patient irradiation. The measured signal (gray line) originates from Hall probes in the scanner magnet. It was translated to actual spot position at iso-center using our machine calibration functions and stays within ± 1.5 mm at all times. The lower plots show tolerances for the instantaneous (integrated) beam current at iso-center measured with dose monitor 1 (2). Measured curves stay within their limits of ± 40 pA and $\pm 7 \times 10^6$ protons, respectively. The time lag of ± 2.5 ms allows for rapid changes in instantaneous beam current (e.g. at $t = 0$ ms in the lower left plot). Figure 3.1 shows the corresponding dose distribution at iso-center of this line scan.

Simulated error scenario

For the same line, let us now assume a severe regulation error, e.g. the current is not decreased after $t = 60$ ms but remains constant. As a consequence, we would hit the tolerance band after 7.5 ms delivering an excess of 1.4×10^6 protons. With a maximum dose deposition of 3.5 nGy per 150 MeV proton in a standard treatment planning voxel, this leads to a potential dose error of:

$$1.4 \times 10^6 \times 3.5 \text{ nGy} \cong 5 \text{ mGy}, \quad (3.14)$$

which is well within our dose constraint of ± 36 mGy.

3.3.2 Safety level 2

Strip monitor response

To consider all dependencies of the pencil beam shape B on the scan configuration, we measured 52,360 individual profiles of stationary pencil beams throughout the five-dimensional (5D) parameter space. These measurements include all possible combinations of 8 different gantry angles ranging from $\alpha_{\min} = -30^\circ$ to $\alpha_{\max} = +180^\circ$, 17 different beam energies ranging from $E_{\min} = 70$ MeV to $E_{\max} = 230$ MeV, 5 different nozzle extensions ranging from $S_{\min} = 1$ cm to $S_{\max} = 27$ cm, 7 different T positions ranging from $T_{\min} = -6$ cm to $T_{\max} = +6$ cm and 11 different U positions ranging from $U_{\min} = -10$ cm to $U_{\max} = +10$ cm. From these measurements, the following response function proved to describe measured data most accurately:

$$B(T) = \begin{cases} B_{\text{trans}} \exp[+\tau (T - (\mu - \omega))] & \text{for } T < \mu - \omega \\ B_{\text{max}} \exp\left[-\frac{1}{2} \left(\frac{T - \mu}{\sigma}\right)^2\right] & \text{for } |T - \mu| \leq \omega \\ B_{\text{trans}} \exp[-\tau (T - (\mu + \omega))] & \text{for } T > \mu + \omega \end{cases} \quad (3.15)$$

with

$$B_{\text{trans}} = B_{\text{max}} \exp\left[-\frac{1}{2} \left(\frac{\omega}{\sigma}\right)^2\right]. \quad (3.16)$$

Figure 3.3(b) displays an example fit of a static spot profile in the T direction. Using this model, we can calculate the response of the strip monitor to scanned line segments via equation 3.6. The fit parameters B_{max} , μ , σ , ω and τ are saved in a 5D look-up table and interpolated for every line segment when predicting the overall profile (see subsection 3.2.4 above). This procedure allows for predicting line profiles for any configuration of delivery parameters. The entire profile prediction algorithm, as executed on a 1.2 GHz single core processor, requires roughly five seconds to compute profiles for 1000 different lines, and is executed once when loading the plan.

Metrics of comparison

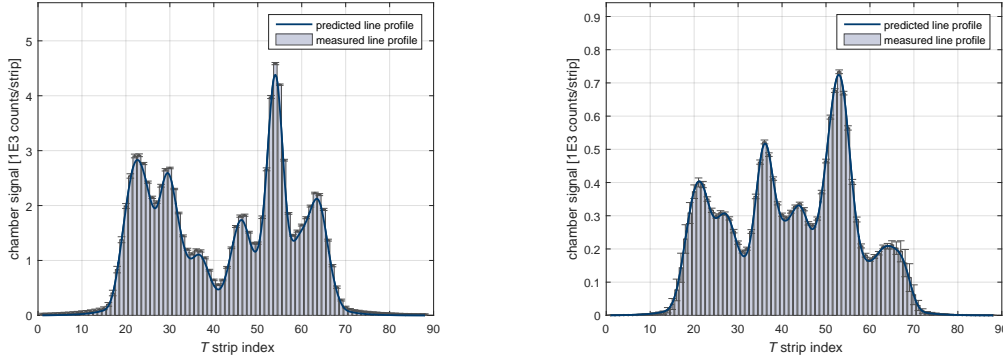
To derive adequate margins for the metrics mentioned above, we applied a set of representative discrete scanning plans previously used for patient treatment on Gantry 2. We superimposed measured profiles of subsequent beam spots with identical U position to emulate irradiation in line scanning mode. From retrospective clinical validation performed by Scandurra et al. (2016) we know that these plans have been delivered with sufficient precision and accuracy. Based on the distribution of comparison metrics, we were able to identify typical upper and lower limits. The results are listed in table 3.1.

Table 3.1: Typical limits for line profile comparison metrics in T and U (see subsection 3.2.5). Δ refers to differences between measured and predicted profiles; δ to deviations. The pass rate of the γ -analysis is given for $\varepsilon = 2\%$ of the maximum line dose and $\rho = 2$ mm (see equation 3.12f). Upper and lower limits were derived from clinical patient plans delivered without any interlocks.

metric of comparison	lower limit	ideal value	upper limit
δD_{tot} [%]	-10.0	0.00	+10.0
ΔT_{COG} [mm]	-1.50	0.00	+1.50
S [%]	-10.0	0.00	+10.0
R^2 [%]	97	100	100
P_γ [%]	70	100	100
ΔU_{COG} [mm]	-1.50	0.00	+1.50
$\Delta \sigma_{\text{RMS}}$ [mm]	-0.50	0.00	+0.50

Example case

Figure 3.6 shows a comparison of measured and predicted T profiles for exemplary lines of relatively high (left) and low dose (right). Scan speeds range between 0.01 and 1.00 cm/ms. The beam current was additionally modulated for the profile of higher dose (see figure 3.5). Note that the profile of lower dose was delivered with an intermediate configuration of gantry angle, beam energy, nozzle extension and line position (i.e. parameters are *not* listed in the look-up table). All metrics of comparison are fulfilled for the two cases and the irradiation could resume without triggering an interlock.



(a) Line scan of relatively high dose for $\alpha = 0^\circ$, $E = 150$ MeV, $S = 27$ cm and $U = 0$ cm. Error bars show one standard error calculated from 50 repetitions. The corresponding dose distribution at iso-center is plotted in figure 3.1; safety level 1 tolerances are displayed in figure 3.5.

(b) Line scan of relatively low dose for $\alpha = 15^\circ$, $E = 115$ MeV, $S = 25$ cm and $U = 5$ cm. Error bars show one standard error calculated from 100 repetitions. Note that the delivery parameters are *not* explicitly contained in the look-up table in this case. Hence, all beam shape parameters had to be interpolated.

Figure 3.6: Comparison of measured (bars) and predicted line profiles (solid lines) in the nozzle plane (T direction). For each segment of the line, we interpolated the five-dimensional look-up table to retrieve the beam shape parameters characteristic to the response of the strip monitor. The prediction matches the measurement for most strips within statistical uncertainty. Both lines satisfy the metrics of comparison introduced in subsection 3.2.5. Note that profiles are *not* normalized; the prediction matches the measurement in absolute values.

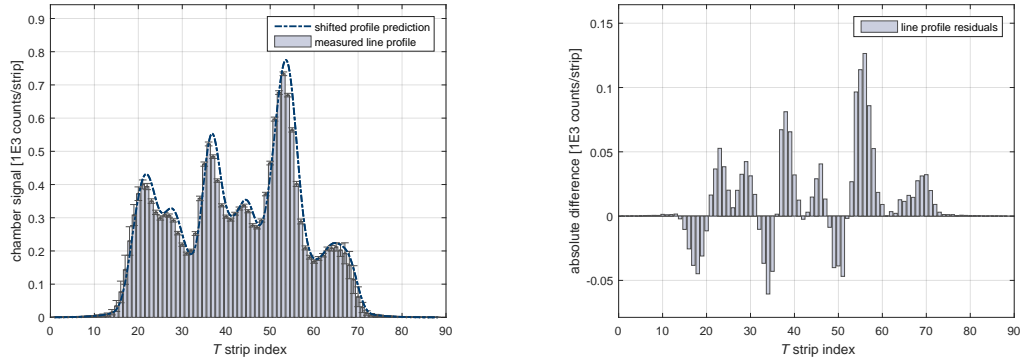
Simulated error scenario

Let us assume a minor regulation issue, e.g. the actual delivered beam current is slightly too low and the entire line is shifted. If both inaccuracies are small enough, they would not classify as a delivery error and remain undetected by safety level 1. In other words, tolerance bands would be fulfilled during delivery and the line would be applied without interlocks. For the profile depicted in figure 3.7, we assumed 7% higher beam current in the prediction and an overall shift of 1.3 mm. This means in return, that 3×10^6 protons would be missing in the delivery. With a maximum dose deposition of 5.0 nGy for 115 MeV protons in a standard treatment planning voxel, we find:

$$- 3.0 \times 10^6 \times 5.0 \text{ nGy} = -15 \text{ mGy}, \quad (3.17)$$

which is within our dose constraint of ± 36 mGy. The position inaccuracy of 1.3 mm is also smaller than our constraint of ± 1.5 mm. However, comparing predicted and measured profiles yields an R^2 index of 96.8%, which is below the threshold of 97.0% stated in table 3.1. Hence, safety level 2 would interrupt the treatment.

3 A beam monitoring and validation system for line scanning



(a) Same line scanning measurement as in figure 3.6(b), but the predicted profile has been shifted to simulate an inaccurate delivery.

(b) Residuals between shifted line profile prediction and measured line profile as displayed in figure 3.7(a).

Figure 3.7: Typical limits for line profile comparison metrics in T and U (see subsection 3.2.5). Δ refers to differences between measured and predicted profiles; δ to deviations. The pass rate of the γ -analysis is given for $\varepsilon = 2\%$ of the maximum line dose and $\rho = 2$ mm (see equations 3.12f). To derive upper and lower limits, we emulated line profiles from clinical patient plans delivered in discrete scanning mode. Irradiations ran interlock-free, which assures clinically acceptable precision and accuracy.

3.4 Discussion and outlook

In this paper, we have described a two-stage monitoring and validation system for proton pencil beam irradiations in continuous line scanning mode. Safety level 1 acts in real-time and uses two independent dose monitors in the gantry nozzle to instantaneously measure the integrated beam current and frequently check it against predefined tolerances. Real-time monitoring is also installed for the lateral beam position. But in this case, we use signals from the Hall probes in the scanner magnets as a surrogate for the beam position at iso-center, in order to have a clean and stable signal independent of the requested beam current. Safety level 2, on the other hand, compares full dose profiles recorded with the strip monitor to precalculated predictions. Such a comparison can be regarded as an online validation of the quality of delivery. To our knowledge, this combination of two safety levels represents a novelty in beam monitoring that is beneficial for, but not restricted to, line scanning irradiations.

The discrete scanning implementation at MD Anderson Cancer Center is very similar to the discrete scanning mode described in subsection 3.2.1 (the beam is turned off completely when moving from one grid point to the next). The beam position is validated only after a spot has been applied. The tolerance used for the measured beam position (width) is ± 1.8 (1.5) mm (Smith et al., 2009), which is slightly larger than our constraints. Other reported dose-driven installations of pencil beam

scanning⁴ use similar monitoring techniques, but typically rely on a time-resolved readout of the position-sensitive monitor as follows:

- Heavy Ion Medical Accelerator in Chiba, Japan: readout of the multi-wire proportional chamber (scanned beam) and fluorescent screen monitor (non-scanned beam) after each spot application (± 2 mm tolerance); additional monitoring the current of the scanner magnet power supply (Furukawa et al., 2010b)
- National Center of Oncological Hadrontherapy, Pavia, Italy: readout of the strip and pixel monitor every 100 μ s (Giordanengo et al., 2013)
- Rinecker Proton Therapy Center, Munich, Germany: readout of the strip monitor every 250 μ s (Borchert et al., 2008)
- Heidelberg Ion-Beam Therapy Center (formerly Gesellschaft für Schwerionenforschung, Darmstadt), Heidelberg, Germany: readout of the multi-wire proportional chambers every 150 μ s (Badura et al., 2000)

In our opinion, the beam position at iso-center can be supervised with (at least) equal precision and accuracy by reading signals from the Hall probes in the scanner magnets. Moreover, we see the advantage of having a higher sampling rate and, therefore, shorter reaction time to errors. For line scanning, we additionally have to consider segments of very low dose (maximum scan speed and decreased current), which yield very low instantaneous signal in the position-sensitive monitor. Hall probe signals, on the other hand, are unaffected by the local dose deposition. Ultimately, we can use the strip monitor to read the integral dose profile of a line and validate the combined effects of speed and current modulation.

The Samsung Medical Center (Seoul, South Korea), is presently, to our knowledge, the only other center that has installed time-driven delivery of pencil beam scanning, but in a slightly modified form. In the United States patent from Inoue (2014), their vendor (Sumitomo Heavy Industries, Ltd.) claims to monitor the beam position with a nozzle-mounted wire chamber every 200 μ s. The treatment is interrupted only if measured and foreseen COG differ. Additional regulation and monitoring of the beam current (as used in our approach), which appears to be constant for each iso-energy layer, are not mentioned in the patent.

Safety level 1 of our system utilizes monitors and readout functionality already installed in the Gantry 2 beamline. Thus, we can easily switch between discrete and continuous scanning mode without changing hardware configurations. To prevent grade two radiation incidents, tolerance bands are derived from the delivery tables

⁴The centers listed here use a hybrid of discrete and continuous scanning: Instead of turning the beam off completely in between spot positions, they accept small transient doses when moving the beam from one position on the scan grid to the next, which lowers the dead time.

(see figure 3.5). The calculation is performed when translating the treatment plan to machine readable files. The actual comparison to measured signals during the scan of a line runs in hardware. Thus, we consider it fast and reliable. Real-time readout additionally allows for real-time logging of the beam current and position at the occurrence of an interlock. This information is important for resuming the treatment at the correct point in space with the correct settings. The design of safety level 1 permits delivering highly modulated lines without compromising patient safety at any time. Very low beam currents (~ 50 pA) can be monitored just as accurately as very high scan speeds (~ 2 cm/ms), since our real-time validation is not hampered by a low signal-to-noise ratio of the strip monitor.

Using the magnetic field of the scanners as a surrogate for beam position at iso-center necessitates a precise cross calibration. This correlation is rather complex (dependencies on gantry angle and beam energy) and specific to the gantry layout. Large changes in beam current or scan speed – when foreseen in the steering file – require introducing a time lag in the tolerance bands due to the finite reaction time of the monitors. But even at maximum current and speed, safety margins are still satisfied.

Safety level 2 assesses the delivery quality online between the application of two lines. We can validate the interplay of speed and current modulation by measuring integral line profiles with the strip monitor in the nozzle. The prediction of line profiles is accurate for all high-dose lines in the 5D parameter space (α, E, S, T, U). Short lines of very low dose (less than ~ 100 counts per strip) are difficult to validate due to a low signal-to-noise ratio. We would have to employ larger margins due to higher measurement uncertainties, which may be practical considering their small contribution to the total delivered dose. Metrics of comparison such as integral counts, COG, RMS, symmetry and R^2 index can be calculated quickly. They ensure that the overall dose, position, width and modulation are within acceptable tolerances. A complete γ -analysis of the profile might be too time consuming and prolong the dead time between lines, which we aim to restrict to 3 ms (average dead time in discrete scanning mode).

The two-level monitoring and validation system described here has been specifically designed for proton irradiations in line scanning mode. Nevertheless, we regard it as a generalized form of beam monitoring applicable to different particles and delivery modes. Even continuous scanning along arbitrarily shaped contours can be supervised with safety levels 1 and 2 as described here. The latter would simply need to validate integral dose profiles in both T and U direction. Furthermore, the monitoring system allows the use of higher beam currents (~ 10 nA) in order to further shorten delivery times. In this case, to satisfy the dose error constraint, we would need to lower the reaction time, which should be feasible considering that monitor responses are well below 2.5 ms (e.g. less than 0.1 ms charge collection time dose monitor 1). Final clinical integration, however, still requires extensive testing of various error scenarios and the development of strategies to resume after interlocks

issued by either safety level.

3.5 Conclusion

The work presented ensures safe patient treatment using continuous line scanning. We identified the main features and risks associated to this mode of operation to derive an adequate, two-level monitoring and validation system: The possibility to change the scan speed and beam current frequently along a single line necessitates continuous monitoring of both parameters. Within safety level 1, we read out both dose monitors and the Hall probes in the scanner magnets every 10 μ s and compare measured signals against predefined tolerances (see figure 3.5). The tolerance bands are calculated from the delivery tables. Interlocks are raised whenever they are exceeded. Presupposing that such dose or position interlocks occur on average less than once per fraction and at random locations, we can guarantee a homogeneity of $\pm 2\%$ of the delivered fraction dose – even in case of several interlocks during one fraction. Such instances would still be classified as harmless grade one radiation events. To assess and validate the quality of the delivered dose, we installed a second safety level, in which we compare the integral dose profile measured with a strip monitor to a forward-calculated prediction (see figure 3.6). This safety level is active after a line has been applied without interlocks. By comparing the weighted center (COG), the overall width (RMS), the symmetry and modulation (e.g. R^2), we are confident to detect inaccuracies in beam current and scan speed that amplify dosimetrically. Interlocks can be raised, whenever metrics of comparison remain unsatisfied. The described beam monitoring and validation system functions with devices and functionality already provided. Currently, we do not see the need to install additional hardware along the beamline to ensure safe operation in line scanning mode.

Authors' contributions

GK performed experiments, analyzed the data and wrote the manuscript. GK, SP and DM designed experiments and interpreted data. CB, UR and ME implemented findings in the therapy control system. SP, AL and DM revised the manuscript at all stages. All authors commented on the paper and approved its final form.

Acknowledgments

The authors would like to express their gratitude to the Giuliana and Giorgio Stefanini Foundation for partly funding this project. Furthermore, they wish to thank Eros Pedroni and all technical experts at PSI for their excellent design and installation of the Gantry 2 beamline. The authors declare that they have no competing financial interests.

4

Real-time beam monitoring in scanned proton therapy

**G. Klimpki^a, M. Eichin^a, C. Bula^a, U. Rechsteiner^a, S. Psoroulas^a,
D.C. Weber^{a,b}, A. Lomax^a, D. Meer^a**

^a Paul Scherrer Institute (PSI), Center for Proton Therapy,
5232 Villigen PSI, Switzerland

^b University Hospital Zurich, Department of Radiation Oncology,
Rämistrasse 100, 8091 Zurich, Switzerland

Nuclear Instruments and Methods in Physics Research A: Accelerators,
Spectrometers, Detectors and Associated Equipment **891** (2018) 62–67
submitted on November 22 (2017) and published on February 27 (2018)

preprint

Abstract

When treating cancerous tissues with protons beams, many centers make use of a *step-and-shoot* irradiation technique, in which the beam is steered to discrete grid points in the tumor volume. For safety reasons, the irradiation is supervised by an independent monitoring system validating cyclically that the correct amount of protons has been delivered to the correct position in the patient. Whenever unacceptable inaccuracies are detected, the irradiation can be interrupted to reinforce a high degree of radiation protection. At the Paul Scherrer Institute, we plan to irradiate tumors continuously. By giving up the idea of discrete grid points, we aim to be faster and more flexible in the irradiation. But the increase in speed and dynamics necessitates a highly responsive monitoring system to guarantee the same level of patient safety as for conventional *step-and-shoot* irradiations. Hence, we developed and implemented real-time monitoring of the proton beam current and position. As such, we read out diagnostic devices with 100 kHz and compare their signals against safety tolerances in an FPGA. In this paper, we report on necessary software and firmware enhancements of our control system and test their functionality based on three exemplary error scenarios. We demonstrate successful implementation of real-time beam monitoring and, consequently, compliance with international patient safety regulations.

4.1 Introduction

Almost every second proton therapy center around the world irradiates their patients using a *step-and-shoot* technique commonly referred to as pencil beam scanning (Haberer et al., 1993; Pedroni et al., 1995): A proton beam of a few millimeter width in air is steered through the three-dimensional (3D) tumor volume by successively changing its penetration depth and transverse position. Scanning in depth (S -direction) can be achieved by adapting the proton beam energy and scanning in the transverse (T, U)-plane¹ is typically realized through a pair of beam-deflecting dipole magnets (see figure 4.1 for a graphical definition of the coordinate system). This state-of-the-art scanning process follows a 3D grid of thousands of discrete beam positions mapped onto the tumor volume. The dwell time at each position can vary from ~ 1 ms up to ~ 100 ms depending on the prescribed number of protons. Upon completion, beamline settings are changed to steer the beam to its next position on the grid.

To guarantee patient safety in case of machine-related errors, the number of delivered protons and the beam position are cyclically checked against expected values. For this purpose, the independent beam monitoring system reads out diagnostic devices (e.g. ionization chambers, position-sensitive monitors) distributed along the beamline. Fastest sampling times reported in the literature are of the order of ~ 0.1 ms (Badura et al., 2000; Borchert et al., 2008; Giordanengo et al., 2013), which yields at least ~ 10 supervisions for every beam position on the grid. The monitoring system will issue an interlock that turns off the beam if expected and measured number of protons deviate by more than a few percent or if the transverse beam position is off by more than ~ 1 mm. As such, compliance with international patient safety regulations (International Commission on Radiation Units and Measurements, 2007; International Electrotechnical Commission, 2014) can be guaranteed.

The Center for Proton Therapy at the Paul Scherrer Institute treats cancer patients since 1996 using pencil beam scanning. To gain flexibility in beam delivery, we aim to go beyond the conventional *step-and-shoot* approach. For this purpose, we discarded the idea of a fixed grid in one of the three dimensions and implemented fully continuous scanning of the proton beam along one of the transverse axes (in the following referred to as the T -axis) (Zenklusen et al., 2010; Safai et al., 2012). This implementation also shortens the overall irradiation time by eliminating dead times when moving from one grid point (T_i, U) to the next (T_{i+1}, U) . We previously showed that by ramping the field of the scanner magnet, we can steer the beam with up to 20 mm/ms along straight T -lines (Pedroni et al., 2011). As such, cyclic monitoring of the beam position every ~ 0.1 ms will no longer be sufficient since the beam could have moved already ~ 2 mm during that time. Uncertainties of this

¹For coplanar treatments with the beam in anterior-posterior direction, the T -axis coincides with the frontal axis of the patient and the U -axis coincides with the longitudinal axis of the patient.

magnitude violate patient safety regulations. Hence, we designed and implemented an enhanced monitoring system that foresees supervision of the beam position and current in real-time (Klimpki et al., 2017b).

While real-time monitoring of beam parameters may be a standard method for many experimental beamlines, it represents a novelty in the context of therapeutically used beams. To our knowledge, no other therapy center relies on real-time monitoring in their primary patient safety system, since it requires fast readout of various detectors installed along the beamline as well as reliable signal processing in hardware. In this paper, we report on the design and implementation of software and firmware enhancements enabling real-time monitoring of the beam current and transverse position and test their functionality based on three exemplary error scenarios.

4.2 Materials and methods

4.2.1 Proton therapy beamline

Figure 4.1 depicts a brief schematic of the proton therapy beamline. A superconducting cyclotron accelerates the proton beam to 250 MeV (Schippers et al., 2007a). For fast intensity control, two deflector plates near the ion source inside the cyclotron can generate an electric field perpendicular to the spiral beam orbit: the higher the field strength, the higher the losses inside the cyclotron and the lower the extracted beam current. By directly controlling the power supply of the vertical deflector plates, we can achieve beam current changes within 50 μ s.

The cyclotron generates a monoenergetic proton beam. However, variable beam energies are required for patient treatments to realize different penetration depths of the proton beam according to the size and location of the tumor. For this purpose, we can insert variable amounts of decelerating (or degrading) material in the beamline. A subsequent double-bend achromat (labeled with energy selection in figure 4.1) assures that only the requested energy reaches the treatment room.

Once in the treatment room, the proton beam passes through an isocentric gantry that rotates around the patient to allow for irradiations from various incident angles. On our Gantry 2, the scanner magnets that determine the final beam position in the transverse (T, U)-plane are placed upstream of the final 90° dipole. By ramping the field strength of these scanner magnets, we can steer the beam with up to 20 mm/ms along straight T -lines (Pedroni et al., 2011).

For fast beam suppression in case of interlocks, we installed a beam-deflecting magnet (so-called kicker) upstream of the degrader unit. When fully powered, it deflects the proton beam onto an absorber. Periodic tests yield an average response time of less than 300 μ s including delays of monitors, electronics, cabling and software.

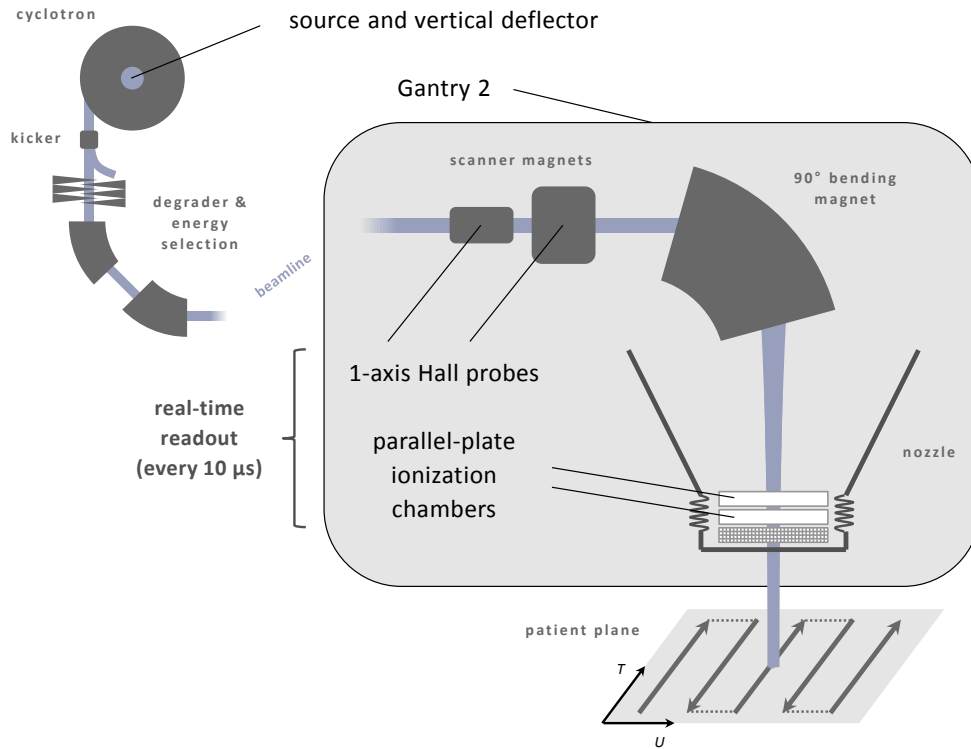


Figure 4.1: Schematic of the Gantry 2 beamline at the Paul Scherrer Institute.

4.2.2 Beam delivery and monitoring

Figure 4.2 depicts the flow of control signals during irradiation. One can see that for safety reasons, our control system is based on two redundant units: the beam delivery system that sends values to all actuators (e.g. vertical deflector and scanner magnets) and the beam monitoring system that reads back status values from independent detectors (e.g. ionization chambers and Hall probes). As such, the delivery unit assures precise and accurate control of the proton beam reaching the patient and the monitoring unit supervises the irradiation process to guarantee patient safety at all times. Both systems are synchronized in real-time and run on VxWorks version 6.9. They communicate over a 32 bit hardware bus.

Real-time monitoring of the beam position and current relies on four monitors: two one-axis Hall probes placed in the scanner magnets and two plane-parallel ionization chambers placed downstream of the vacuum exit window (see figure 4.1 and the section below for more details). During irradiation, dedicated readout electronics convert their analog signals to digital counts and transmit them at 100 kHz over a 2 Gbit/s line to the main field-programmable gate array (FPGA) of the monitoring system (Virtex-6 from Xilinx, Inc.). Interlocks can be raised whenever signals fall below or exceed their specified tolerances.

Hall probes

The field strength of the scanner magnets is directly correlated to the beam position in the transverse plane. Thus, supervising their magnetic field allows for non-destructive monitoring of the transverse beam position. Measurement ranges of the Hall probes span ± 0.2 T and ± 0.4 T for the T and U scanners, respectively. The noise in both probes amounts to less than $10 \mu\text{m}$ uncertainty in position.

Ionization chambers

Both parallel-plate ionization chambers, referred to as monitor 1 and 2 in the following, are filled with air at ambient temperature and pressure and have a maximum charge collection time of approximately $90 \mu\text{s}$ and $240 \mu\text{s}$, respectively (Lin et al., 2009). Hall probes and ionization chambers are synchronized in their real-time readout.

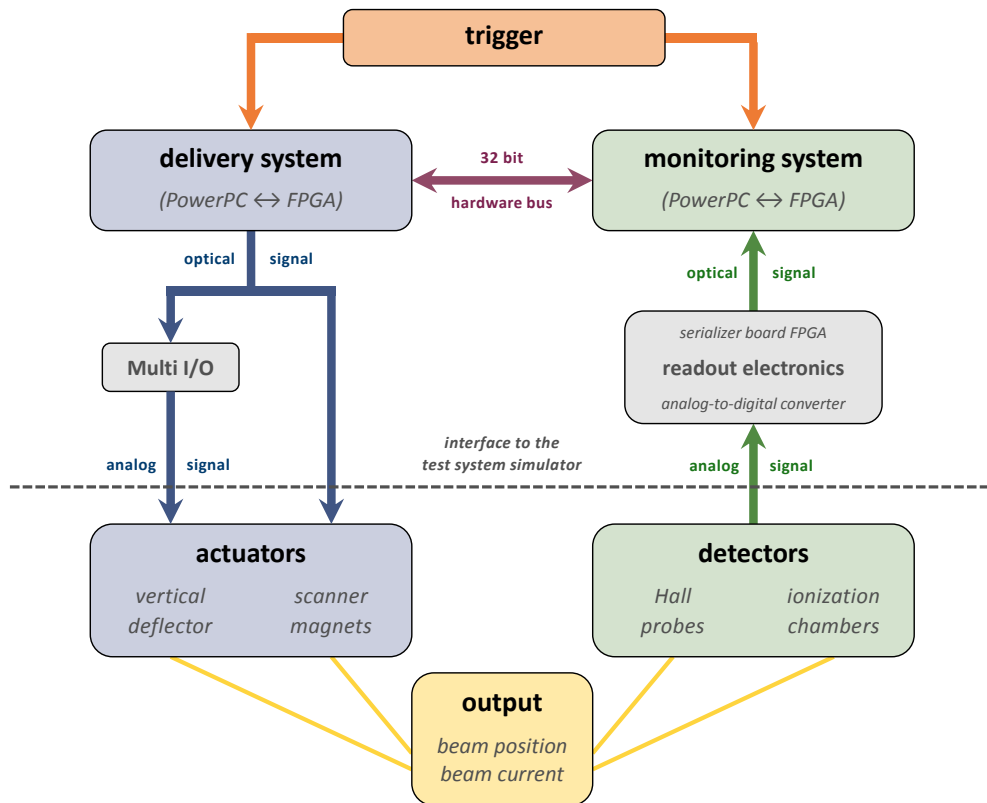


Figure 4.2: Signal flow of the delivery and monitoring system during irradiation.

4.2.3 Control software

State-of-the-art proton therapy systems offer large flexibility in varying the amount of locally deposited protons. When scanning along T -lines, we wanted to support modulating the scan speed v and beam current I simultaneously. Hence, we implemented time-driven irradiations based on trajectory tables of the form

$$\{(t_1 = 0 \text{ ms}, T_1), \dots, (t_n > 0 \text{ ms}, T_n)\} \quad (4.1)$$

and

$$\{(t_1 = 0 \text{ ms}, I_1), \dots, (t_n > 0 \text{ ms}, I_n)\}, \quad (4.2)$$

which will be interpolated linearly by the control system. In other words, the beam is scanned over the distance $\Delta T = T_{i+1} - T_i$ during the time interval $\Delta t = t_{i+1} - t_i$ with a constant speed $v = \Delta T / \Delta t$, while the beam current changes linearly from I_i to I_{i+1} . The minimal step size in time is $10 \mu\text{s}$. The beam current I is feedback-controlled and ranges from a few hundred pA down to $\sim 10 \text{ pA}$. The beam is suppressed completely when fully powering the vertical deflector plates.

Since this time-driven form of treatment places high demands on controls and monitoring, it is not a standard solution for most therapy centers. Changes in the proton beam position and current can occur frequently, which necessitates monitoring these irradiation parameters in real-time. To do so, we calculate tolerance bands for every line prior to its application. Such tolerances contain shifts of the nominal signals ($\pm\delta I$ and $\pm\delta T \mid \pm\delta U$) as well as shifts along the time axis ($\pm\delta t$) to allow for clinically acceptable uncertainties in the irradiation. As a result, we end up with four tolerance tables containing upper and lower limits; one for each Hall probe and one for each ionization chamber. Choosing adequate margins (see Klimpki et al. (2017a) for detailed derivation), we can assure that irradiations are carried out safely. Table 4.1 exemplifies upper and lower tolerances for the beam current measured with monitor 1.

To compare transmitted signals during the irradiation of a line to their corresponding upper and lower tolerances fast and reliably, we execute this task in the main FPGA of the monitoring system. For this purpose, the control system converts the calculated tolerance tables from physical units (e.g. ms, cm, pA) to digital counts before downloading them to the FPGA. The actual firmware implementation is described in the following section².

²Software and firmware solutions concerning real-time monitoring were partly developed by SCS Supercomputing Systems AG, Zurich, Switzerland.

Table 4.1: Delivery table for the proton beam current I (left column) and the corresponding upper (middle column) and lower tolerances (right column). The margins in the example were chosen to be $\delta I = 50$ pA and $\delta t = 2$ ms. Figure 4.7 shows the linear interpolation of these tables carried out in firmware.

<i>nominal beam current</i>		<i>upper beam current tolerance</i>		<i>lower beam current tolerance</i>	
t	I_{nom}	t	I_{max}	t	I_{min}
[ms]	[pA]	[ms]	[pA]	[ms]	[pA]
0.00	0	0.00	550	0.00	0
0.01	500	38.00	550	2.00	0
37.99	500			2.01	450
38.00	0			35.99	450
				36.00	0
				38.00	0

4.2.4 FPGA firmware of the monitoring system

Precise and reliable timing on the μs scale is crucial for time-driven irradiations as described above. Hence, the beam delivery and monitoring system run on synchronized hardware (FPGAs) that processes and analyzes incoming signals in real-time. Figure 4.3 provides a simplified sketch of the monitoring firmware logic that we developed and implemented for this purpose.

The FPGA supports data input over eight optical links. Every incoming data package contains a 16 bit value in units of ADC counts and a unique 21 bit timestamp. Registers set by the control system link the different data channels to the physical sensors (Hall probes and ionization chambers). Furthermore, each channel can be configured to either nominal or integrated limit supervision. In the former case, the incoming 16 bit value is directly compared to reference data (high and low limit) obtained through linear interpolation of the tolerance tables loaded into the random-access memory (RAM)³. NOM_HIGH and NOM_LOW interlocks will be triggered if the comparison fails. Signals from both T and U Hall probes as well as ionization chamber 1 are configured as nominal limit supervisors. In other words, we monitor the beam position and current every $10 \mu\text{s}$ during irradiation. We use ionization chamber 2 as a redundant monitor and configured it as an integrated limit supervisor. As such, we can also monitor the total number of protons being delivered to the patient over time. For this purpose, nominal 16 bit values are multiplied by the difference of two consecutive timestamps ($10 \mu\text{s}$) and added to a running counter.

³Due to limitations in the RAM, tolerance tables can contain a maximum of 512 entries.

To reduce traffic and free RAM space, reference data is also integrated in hardware and not in software. In the comparison step, we add and subtract a fixed margin to the integrated reference to obtain upper and lower bounds, respectively. INT_HIGH and INT_LOW interlocks will be triggered if the comparison fails.

In case of limit violation during irradiation, the FPGA is able to raise an interlock immediately. All interlocks of this origin will generate an emergency beam-off command. Such commands are anchored deep within the patient safety system and common to irradiations in discrete and continuous scanning mode. The reaction time to switch off the beam is dominated by the time it takes to power the kicker magnet ($< 300 \mu\text{s}$). To retrospectively analyze the source of the interlock, we log its time of occurrence as well as the violation value and its corresponding high and low tolerances. Additionally, we store tables of the incoming data for every channel at full time resolution in machine log files.

At the beginning of every new T -line, the control software generates a trigger pulse that clears the RAM, resets all interlock registers and sets the integration counter back to zero. A pulse generator within the FPGA receives this software trigger and distributes it to the readout electronics of all monitors.

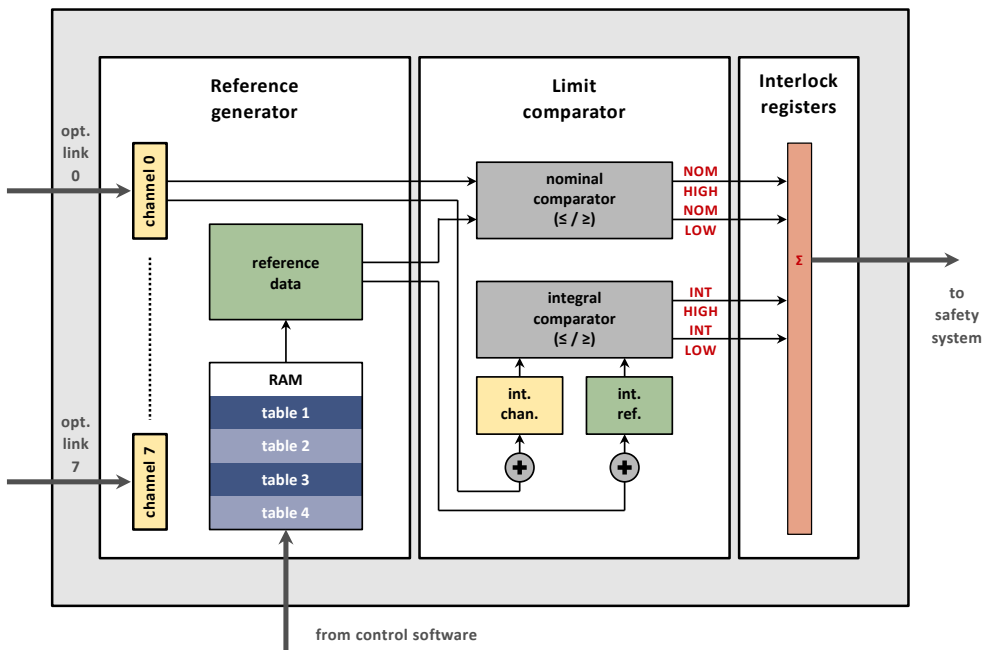


Figure 4.3: Simplified sketch of the FPGA logic in the monitoring system responsible for nominal and integrated limit supervision in real-time.

The firmware supports supervision of two upper and two lower tolerances for every data channel – we will refer to them as error and warning bands in the following.

Upper and lower errors are configured to trigger interlocks as described above. Upper and lower warnings, on the other hand, shall provide information on the performance of the machine to estimate the likelihood of interlocks. For this purpose, and without disturbing the irradiation, we log the number of high and low warning violations for every data channel. The values on these warning counters are stored in the machine log file for every T -line. Margins for warning bands are self-evidently smaller than margins for error bands.

4.2.5 Gantry 2 test system

Gantry 2, together with its beamline and control system, was developed in-house. To enable debugging, maintenance and further development independent of the clinical operation, we installed an exact copy of the readout electronics and software in a separate lab (see figure 4.4). This test system features a decoupled beam delivery and beam monitoring unit as well as identical signal processing and similar timing characteristics compared to the productive system. Furthermore, it hosts a simulator unit that mimics the response of the Hall probes and ionization chambers. We are using and maintaining this test environment since 2005 and it proved to be a valuable and accurate tool especially during commissioning of Gantry 2. Hence, we tested software and firmware features described in subsections 4.2.3 and 4.2.4 above on this system. The response to various error scenarios – often impossible to provoke on the productive system – could be simulated without any risk of damaging devices used in daily, clinical operation.

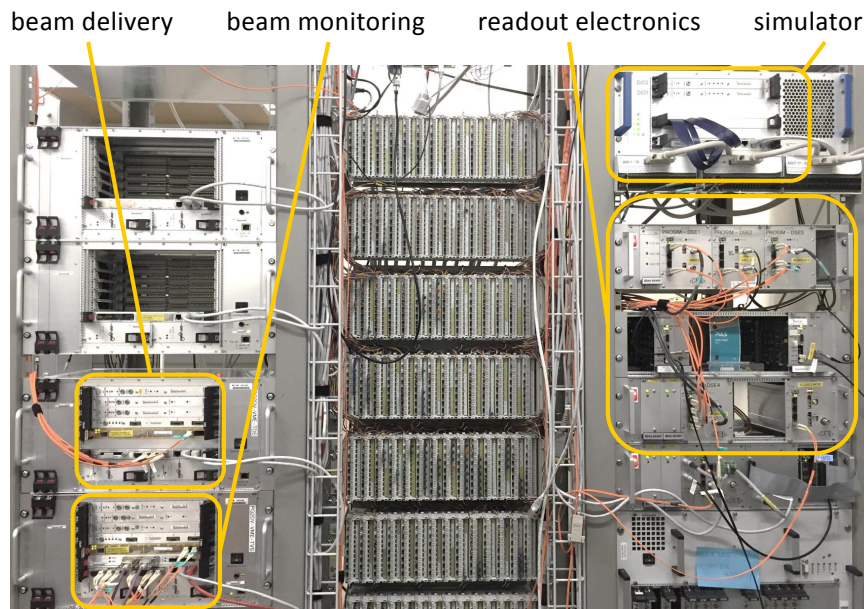


Figure 4.4: Installation of the Gantry 2 test system.

4.2.6 Verifying software and firmware enhancements

We verified functionality of the new software and firmware implementations described in subsections 4.2.3 and 4.2.4 above on the Gantry 2 test system. To demonstrate capability of interpolating delivery and monitoring tables in real-time (see table 4.1), we compare signals sent to the actuators by the delivery system and signals read back from the corresponding detectors in subsection 4.3.1 below. For this purpose, we make use of the implemented logging functionality of the FPGA firmware that allows writing tables of detected data samples at full time resolution to machine log files.

In subsection 4.2.4 above, we described how we equipped the FPGA of the monitoring system with interlock triggering functionality to terminate the irradiation of the patient whenever a tolerance violation has been detected. To test this functionality, we connected incoming and reference data lines inside the reference generator block (see figure 4.3) to an oscilloscope. As such, we can observe the signals sent to the nominal limit comparator unit (dark gray box in figure 4.3). To retrace if they are handled correctly, we also displayed the interlock lines on the oscilloscope. Exemplary tests of the `NOM_LOW` and `NOM_HIGH` interlocks are described in subsections 4.3.2 and 4.3.3 below.

Verifying `INT_LOW` and `INT_HIGH` interlocks requires an additional step, since we cannot connect the output values of internal integrators of the FPGA to an oscilloscope. Hence, we recorded the incoming data samples using the built-in logging functionality of the FPGA and retrospectively integrated this data. By applying the same warning and error thresholds configured in the firmware, we can calculate the intersection point between integrated signal and upper/lower error band. Its time of occurrence should match the value stored in the FPGA interlock register. By comparing the two, we can test the accuracy of the internal integration unit. In subsection 4.3.4 below, we trigger an `INT_HIGH` error of the proton beam current.

4.3 Experiments and results

In this section, we would like to demonstrate successful implementation of software and firmware functionality as described above based on one successful and three erroneous T -line irradiations. We simulated an error in beam position as well as in instantaneous and integrated beam current. All measurements were conducted on the Gantry 2 test system.

4.3.1 Logging functionality

Figure 4.5 shows the monitored T -position of a successfully irradiated line. For demonstration purposes, the delivery table foresees changes in the scan speed ev-

ery 5 ms. Typical speed modulation will be irregular in time. In this test case, we compare nominal position (as stated in the delivery table) and monitored Hall probe signal. The latter was recorded using the built-in logging functionality of the firmware described in subsection 4.2.4. When subtracting the two (see inset figure), we observe that deviations between planned and monitored position occur when changing the scan speed. The differences are within +24 and -32 ADC counts, which translates into less than $\pm 100 \mu\text{m}$ position error of the beam.

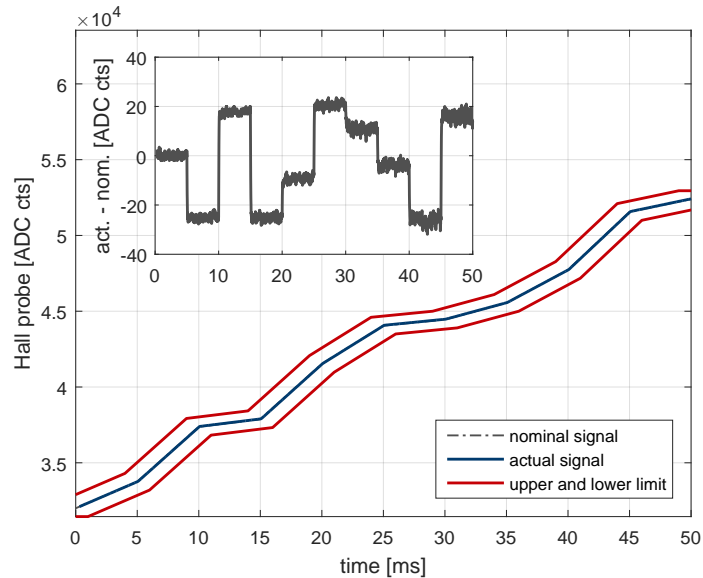


Figure 4.5: Nominal beam position (dashed gray line) and measured Hall probe signal (solid blue line) demonstrating logging functionality of the FPGA firmware. Upper and lower limits are displayed in red ($\delta t = 1$ ms and $\delta T = 1.5$ mm). The inset in the top right corner shows the difference between logged and expected Hall probe signal.

4.3.2 Error in beam position

A plausible error scenario for the proton beam position could be a non-responding T scanner magnet that stagnates at a fixed field strength and prevents the beam from moving along the T -line (see figure 4.6). Such an error needs to be prevented as it yields a local, potentially harmful overdose of protons to the patient. To simulate this error, we manually corrupted the nominal trajectory table (see equation 4.1) before irradiating the T -line. However, the tolerance bands were calculated on the original table with $\delta T = 1.5$ mm. Hence, we end up with mismatching delivery and monitoring configurations. For visualization purposes, we connected the actual beam position and the upper and lower error bands to an oscilloscope (see subsection 4.2.6 for a detailed description of the procedure). Furthermore, we connected the `NOM_LOW` interlock line to enable quantitative determination of the time of tolerance violation. We triggered data acquisition on the rising edge of the software trigger that synchronizes beam delivery and monitoring right before the application

of the line. In figure 4.6 we see that the value of the interlock register changes as soon as the actual beam position crosses the lower tolerance band. Irradiation parameters were chosen such that the violation occurs at precisely 40 ms after the start of line. Analyzing the recorded signal yields an interlock trigger after 40.08 ms.

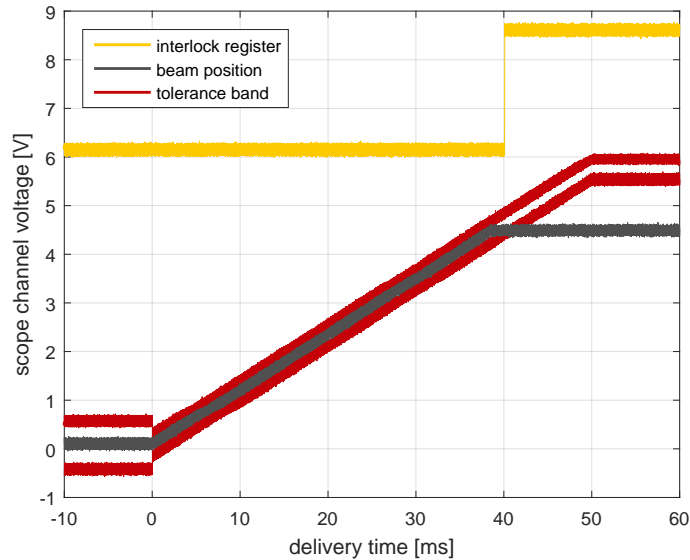


Figure 4.6: Interlock scenario for the beam position measured with an oscilloscope connected to the FPGA of the monitoring system. The interlock register (yellow line) flips as soon as the detected beam position (gray line) violates the tolerance band (red lines).

4.3.3 Error in instantaneous beam current

A plausible error scenario for the instantaneous beam current could be a non-responding vertical deflector that stagnates at a fixed field strength and fails to regulate down the current (see figure 4.7). In this case, we would over-dose the patient and, therefore, we need to issue a beam-off command to the kicker magnet. To simulate this error, we followed the procedure described in subsection 4.3.2 above. But this time we manipulated the nominal beam current table (see equation 4.2) and connected it to the oscilloscope. Tolerance bands were, once again, calculated on the original table with $\delta t = 2$ ms and $\delta I = 50$ pA. In figure 4.7 we see that the value of the interlock register changes as soon as the actual beam current crosses the upper tolerance band. Irradiation parameters were chosen such that the NOM_HIGH violation occurs at precisely 40 ms after the start of the line. Analyzing the recorded signal yields an interlock trigger after 40.02 ms. The zoom shows that it requires roughly 300 μ s (reaction time of the kicker magnet) to completely suppress the beam after triggering the interlock.

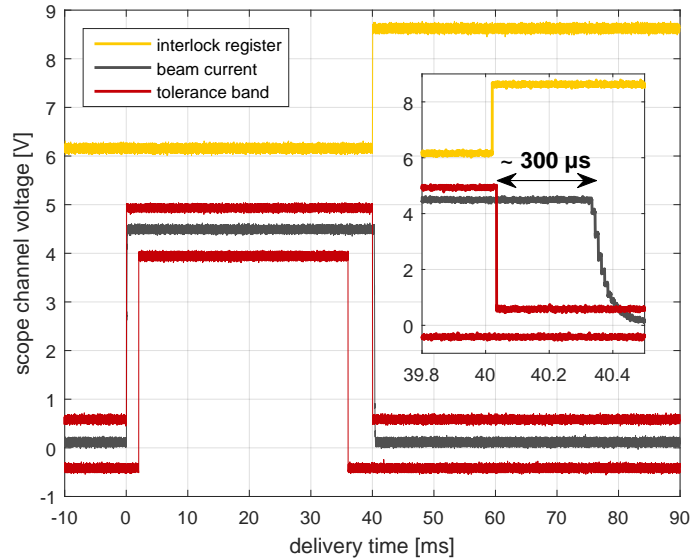


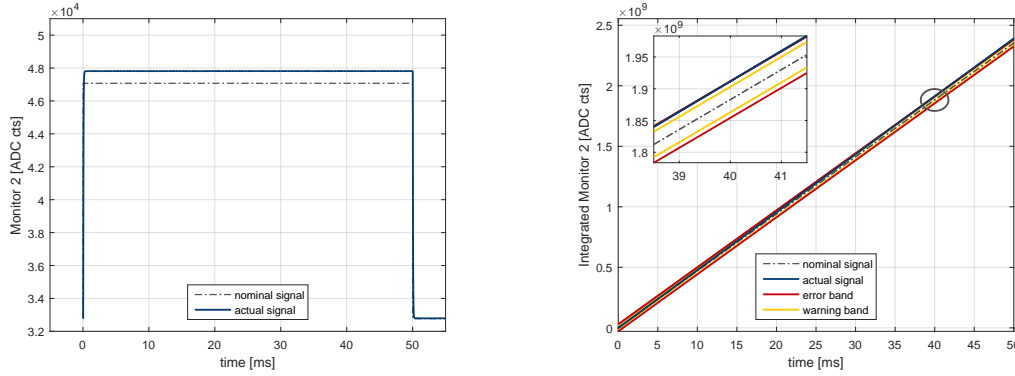
Figure 4.7: Interlock scenario for the *instantaneous* beam current measured with an oscilloscope connected to the FPGA of the monitoring system. The interlock register (yellow line) flips as soon as the detected beam current (gray line) violates the tolerance band (red lines). A zoom around the point of violation is shown in the inset. The corresponding tolerance bands are given in table 4.1.

4.3.4 Error in integrated beam current

The error scenario portrayed in subsection 4.3.3 above delivers excess protons at the end of the line only; throughout the irradiation, the beam current follows its target value. However, if the set point is constantly too high (or too low), we will start deviating from the prescribed number of protons much earlier in the delivery. We regard such a case as highly unlikely because of our feedback regulation loop, but the tolerance bands shown in figure 4.7 could be blind to such systematic offsets. Hence, we additionally supervise the integrated beam current with ionization chamber 2. The integration principle is described in subsection 4.2.4 and we designed the following error scenario to test it: We added a fixed offset to the beam current delivery table. Its magnitude is small enough not to violate the instantaneous limit supervision as shown in figure 4.8(a). Integrating the nominal beam current over time yields a linear increase in the number of delivered protons; integrating the manipulated beam current over time yields a linear increase with elevated slope (see figure 4.8(b)). After 40 ms, we expect to trigger an INT_HIGH interlock.

For this example case, we followed the test procedure described in the last paragraph of subsection 4.2.6. Integrating the logged monitor 2 signal and the upper integration limit yields a tolerance violation after 39.99 ms (figure 4.8(b)). The interlock register in the firmware showed a value of 40.01 ms, which amounts to a deviation of two samples (20 μ s). The number of warning violations calculated from the logged signal

is slightly larger than the value on the FPGA warning counter: 2177 vs. 2174.



(a) Logged instantaneous monitor 2 signal (solid blue line) and the targeted beam current (dashed gray line).

(b) Integration of the logged monitor 2 signal and detection of the upper error violation (see inset for a zoom on the circle region).

Figure 4.8: Interlock scenario for *integrated* beam current reconstructed from the FPGA logging data of an erroneous irradiation.

4.4 Discussion and conclusion

We developed and implemented real-time beam monitoring on a clinically operating proton therapy beamline. The transverse beam position and the beam current at the patient are sampled on a 100 kHz clock – more frequent than current state-of-the-art therapy systems. An FPGA compares sampled signals to predefined tolerances in real-time. Based on three exemplary error scenarios, we demonstrated that implemented software and firmware enhancements are able to trigger interlocks whenever measured currents or positions violated their respective tolerances. In case of tolerance violation, four monitoring tables are written to the machine log file in full resolution; one for each Hall probe and one for each ionization chamber. In addition to instantaneous limit supervision, we included a hardware-based beam current integrator that supervises the total number of protons delivered during irradiation. All systems run synchronized on a 10 μ s clock.

The results presented in section 4.3 were obtained on the Gantry 2 test system. We are well aware that such a test environment can never represent the productive system in its full complexity. However, even if incoming signals may significantly differ from simulated input, their handling in firmware will be identical and we are confident that interlocks can be triggered with equal reliability. Furthermore, we do not see any differences in handling interlocks triggered in discrete or continuous scanning mode, since patient safety logic and treatment interruption mechanisms are identical. Self-evidently, we foresee additional tests on the productive system

before irradiating patients in line scanning mode.

Our choice of hardware (e.g. monitors, electronics) was restricted to installed and commissioned devices on the Gantry 2 beamline. This particularly affected real-time monitoring of the beam position. The readout of our position-sensitive monitor (see gridded box in figure 4.1) is not fast enough to enable frequent position checks. One could argue that such direct position supervision might be more obvious, but we would like to emphasize that it is also sensitive to low signal-to-noise ratios (typically expected when regulating the beam current down). E.g. at the National Center of Oncological Hadrontherapy in Pavia, Italy, the strip and pixel monitors are read out every $100\ \mu\text{s}$ (Giordanengo et al., 2013). By relying on Hall probe data and an indirect position supervision, we can guarantee high sampling rates and a stable signal-to-noise ratio ($< 10\ \mu\text{m}$ uncertainty in position) independent of the applied beam current. Furthermore, we can use our position-sensitive monitor as a redundant validation device by integrating the fluence profile over the entire duration of a T -line.

Translating double-precision beam positions and currents into integer ADC counts yields inaccuracies in the calculation of the tolerance bands. For example, when scanning the proton beam over the full scan range from $T = -6\ \text{cm}$ to $T = +6\ \text{cm}$, we expect errors smaller than $\pm 100\ \mu\text{m}$ in the interpolation of the tolerance band. For the beam current integrator, inaccuracies will be smaller than $\pm 2 \times 10^4$ protons (for a 120 MeV beam) when ramping down/up the beam current linearly over a duration of 10 ms (maximum allowed step size in time). Margins for the tolerance bands derived from clinical constraints (International Commission on Radiation Units and Measurements, 2007; International Electrotechnical Commission, 2014) are much larger: we can typically accept errors in beam position of the order of $\delta T = \delta U = \pm 1.5\ \text{mm}$; the deviation from the integrated number of protons should be smaller than $\pm 6 \times 10^6$ for a 120 MeV beam (Klimpki et al., 2017b). Even if we exceed these limits once throughout the course of the treatment, we do not expect any clinical consequence for the patient.

Last but not least, we wish to point out that this real-time beam monitoring system is designed for, but certainly not restricted to, continuous irradiations in line scanning mode. It features high sampling rates and, thus, short reaction times to errors in beam delivery. As such, it meets the general demand for faster and more dynamic patient treatments. Furthermore, the presented monitoring system grants sufficient flexibility in the definition of the tolerance bands to facilitate various beam scanning implementations: different transverse scan patterns (e.g. arbitrarily shaped contours) and different ion species (e.g. helium or carbon) can be supervised equally precise and accurate using the presented methods and tools.

Acknowledgments

The authors would like to thank Dr. Eros Pedroni and the technical experts at PSI for their excellent work on the Gantry 2 beamline and test system.

Funding

This work was supported by the Giuliana and Giorgio Stefanini Foundation, Wilen, Schwyz (Switzerland).

5

A real-time beam monitoring system for highly dynamic irradiations in scanned proton therapy: derivation of safety tolerances

**G. Klimpki^a, M. Eichin^a, C. Bula^a, U. Rechsteiner^a, S. Psoroulas^a,
D.C. Weber^a, A. Lomax^a, D. Meer^a**

^a Paul Scherrer Institute (PSI), Center for Proton Therapy,
5232 Villigen PSI, Switzerland

Proceedings to the 16th International Conference on Accelerator
and Large Experimental Physics Control Systems (ICALEPCS 2017)
THCPAO6:1224–1228

submitted in October (2017) and published in January (2018)

postprint

Abstract

Patient treatments in scanned proton therapy exhibit dead times, e.g. when adjusting beamline settings for a different energy or lateral position. On the one hand, such dead times prolong the overall treatment time, but on the other hand they grant possibilities to (retrospectively) validate that the correct amount of protons has been delivered to the correct position. Efforts in faster beam delivery aim to minimize such dead times, which calls for different means of monitoring irradiation parameters. To address this issue, we report on a real-time beam monitoring system that supervises the proton beam position and current during beam-on, hence while the patient is under irradiation. For this purpose, we sample one-axis Hall probes placed in beam-scanning magnets and plane-parallel ionization chambers every 10 μs . FPGAs compare sampled signals against verification tables – time vs. position/current charts containing upper and lower tolerances for each signal – and issue interlocks whenever samples fall outside. Furthermore, we show that by implementing real-time beam monitoring in our facility, we are able to respect patient safety margins given by international norms and guidelines.

Preface

A detailed report on software and firmware enhancements of the control system has been submitted as an ordinary paper (Klimpki et al., 2018). In these proceedings, we concentrate on one part of the work and derive applicable safety tolerances supervised by the real-time monitoring system.

5.1 Introduction

In scanned proton therapy, we use a Gaussian-shaped beam of protons to irradiate cancerous tissue. The beam size σ in air amounts to a few millimeters. To cover the entire extent of the three-dimensional tumor volume with protons, the beam needs to be scanned transversally and in depth. At the Paul Scherrer Institute (PSI), we installed a dedicated super-conducting cyclotron that provides a continuous and mono-energetic proton beam of 250 MeV (Schippers et al., 2007a). We realized transverse scanning with a pair of beam-deflecting dipole magnets; to scan the proton beam in depth, we change its energy (and, thus, penetration depth) by inserting variable amount of degrading material into the beamline (Pedroni et al., 2011).

The beam scanning process requires a discretization of the tumor volume: it is cut in slices of equal energy (or penetration depth) and a rectilinear scan grid of fixed transverse (or lateral) beam positions is imposed on all of those slices. In our second-generation treatment room at PSI, we require ~ 100 ms to change the beam energy between slices and ~ 3 ms to scan the beam from one transverse grid point to the next (Safai et al., 2012). The beam is turned off completely during those transitions. We use this dead time, especially the latter, to validate that the correct amount of protons has been applied to the correct position. If the deviation between measurement and expectation exceeds a certain tolerance, we have the possibility to interrupt the treatment of the patient to investigate the source of uncertainty. International norms (International Electrotechnical Commission, 2014) and guidelines (International Commission on Radiation Units and Measurements, 2007) demand such frequent checks to guarantee patient safety.

At PSI, we treat patients successfully using this discretized beam scanning technique since 1996. To maximize irradiation performance and possibly broaden the window of treatable indications, we pursue implementing a faster form of beam delivery, which we call line scanning (Zenklusen et al., 2010). In line scanning, the beam is moved continuously along straight lines in the transverse plane giving up the idea of the fixed grid in this dimension. The 3 ms dead times are reduced to changes between lines, which yields increased performance but, at the same time, fewer opportunities for validation checks.

To provide adequate safety measures for line scanning, we introduced a dedicated beam monitoring system. We reported on its design (Klimpki et al., 2017b) and implementation (Klimpki et al., 2018) in previous works. A major enhancement with respect to the conventional monitoring approach is its real-time character: we compare the measured beam position and proton deposition to predefined tolerances every $10\ \mu\text{s}$. This cyclic comparison runs during beam-on, hence while lines are scanned. As such, we can react to errors in different beam delivery units very fast and issue beam-off commands rapidly in case of unforeseen inaccuracies or failures.

The scope of this paper is to provide a full derivation of our line scanning safety tolerances. We will focus on acceptable over/underexposure of the healthy/malignant tissue to radiation and acceptable deviations in the transverse beam position. Based on our experience in patient treatments, we presuppose that errors in beam delivery occur rarely (less than once throughout the entire course of the treatment) and randomly. They cannot be linked to specific configurations of the machine and do not lead to any systematic effects.

5.2 Derivation of safety tolerances

5.2.1 Definition of erroneous delivery

An average treatment schedule at PSI foresees 30 irradiation sessions. In each session, an average dose of 1.818 Gy is delivered homogeneously to the tumor volume. We consider an irradiation erroneous if the homogeneity (or uniformity) across the target is significantly impaired. We set the threshold at absolute deviations of $\pm 2\%$ or $\pm 36\ \text{mGy}$. Localized over- or underdosages of this magnitude are physically measurable, but we do not expect them to have any consequence on the clinical outcome of the treatment. Hence, we aim to restrict all excess or missing doses to $\pm 36\ \text{mGy}$, even in case of severe errors of the delivery system. Line scanning under such monitoring conditions can be considered safe.

With this definition we follow the guidelines of the International Commission on Radiation Units and Measurements. They claim that safe and accurate irradiations apply to doses that “*are delivered throughout the target volume with sufficient uniformity (better than $\pm 2.5\%$)*” (International Commission on Radiation Units and Measurements, 2007). Furthermore, we are well within the tolerance given by the International Electrotechnical Commission:

“The secondary dose monitoring system shall be set to terminate irradiation before an additional absorbed dose of 10% or 0.25 Gy, whichever is greater, is delivered.”

– International Electrotechnical Commission (2014)

In order to fulfill the $\pm 36\ \text{mGy}$ constraint – even in case of severe failures of the

beam delivery system – we supervise the following three quantities in real-time during patient irradiation: (i) total dose deposition, (ii) instantaneous beam current, as well as (iii) transverse beam position. We measure the former two quantities with two independent parallel-plate ionization chambers (Lin et al., 2009) that are connected to cyclic readout electronics (data samples every 10 μ s). They are the final diagnostic elements in the beamline and placed between the exit window of the vacuum beam pipe and the patient. The beam position in the transverse plane is supervised indirectly by one-axis Hall probes, which measure the field strength of the beam-scanning magnets at identical readout frequency. High field strengths correspond to a large transverse deflection of the proton beam and vice versa.

In the following sections, we will derive acceptable safety tolerances for all three quantities. We base our derivation on the assumption that all machine-related errors occur rarely. Hence, we regard a combined failure of multiple elements as highly improbable.

5.2.2 Maximum dose deposition of a proton beam

When protons penetrate through matter, they continuously lose energy before coming to rest. The energy loss is low at the beginning of their path and reaches a maximum near the end of their range. Due to collisions with target nuclei, protons may experience large angle deflections. The combined effect of characteristic energy deposition and transverse scattering can be seen in figure 5.1.

The energy deposition is quantified as absorbed dose D and formally defined as

$$D = \Delta\varepsilon/\Delta m, \quad (5.1)$$

with the mean energy imparted $\Delta\varepsilon$ in the mass element Δm . Doses can be measured in finite volumes ΔV only. The PSI treatment planning software uses a voxel size of

$$\Delta V = (4.0 \times 4.0 \times 2.5) \text{ mm}^3. \quad (5.2)$$

If we place such a small volume on the central beam axis (white dashed line in figure 5.1) and calculate the average dose deposition as a function of penetration depth, we obtain the ‘on-axis’ Bragg curves shown in figure 5.2. We see that the maximum energy deposition never exceeds

$$D_{\max} = 4.2 \text{ nGy/proton}. \quad (5.3)$$

Furthermore, the analytic calculations (Pedroni et al., 2005) agree with the Monte Carlo simulations (Perl et al., 2012), which are based on a detailed phase space model of our proton beam. We conclude that, independent of the beam energy, we will never deposit more dose than D_{\max} inside a small volume of size ΔV assuming that the material contained is water-like.

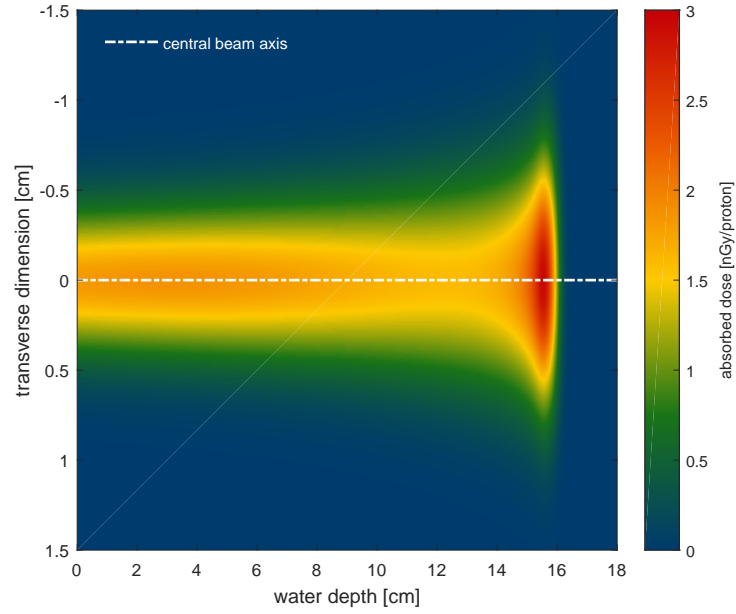


Figure 5.1: Energy deposition of a 150 MeV proton beam in water. The initial beam width σ was assumed to be 2.9 mm. The calculation was performed using the analytic transport models of the PSI treatment planning software.

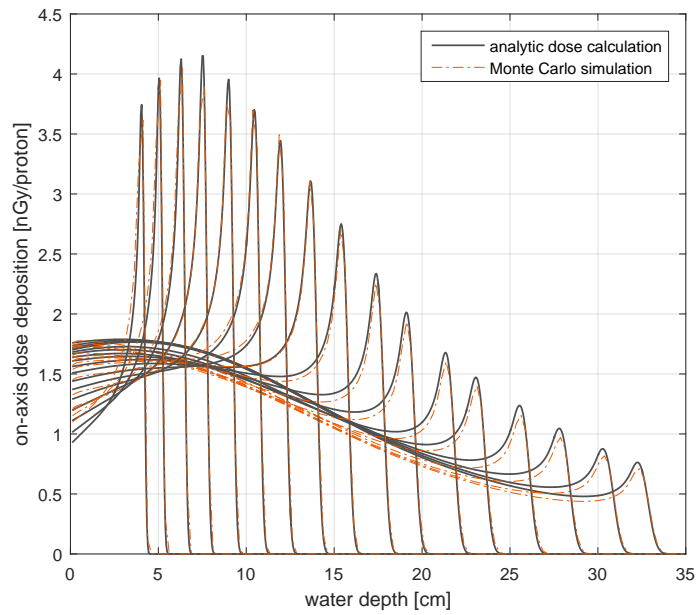


Figure 5.2: Analytically calculated vs. Monte-Carlo-simulated on-axis Bragg curves for 17 different incident energies (70, 80, ..., 220, 230) MeV.

5.2.3 Tolerance for dose deposition

Both ionization chambers have been calibrated to measure the proton beam current I . Internally, they operate on monitor units (MU), which can be correlated to absolute number of protons using the calibration curve shown in figure 5.3. The maximum authorized beam current in the treatment room is limited to 500 MU/ms. E.g. at 120 MeV we find

$$I_{\max} = 500 \text{ MU/ms} \approx 500 \text{ pA}. \quad (5.4)$$

Scaling all on-axis Bragg curves of figure 5.2 by their corresponding MU-conversion factor (see figure 5.3) yields a maximum dose deposition of

$$D_{\max} = 0.024 \text{ mGy/MU}. \quad (5.5)$$

Hence, we can set the tolerance for the deposited dose to

$$\delta D_{\max} = \frac{36 \text{ mGy}}{D_{\max}} = 1500 \text{ MU}, \quad (5.6)$$

which means that the delivered dose distribution will have sufficient homogeneity if deviations are within $\pm \delta D_{\max}$.

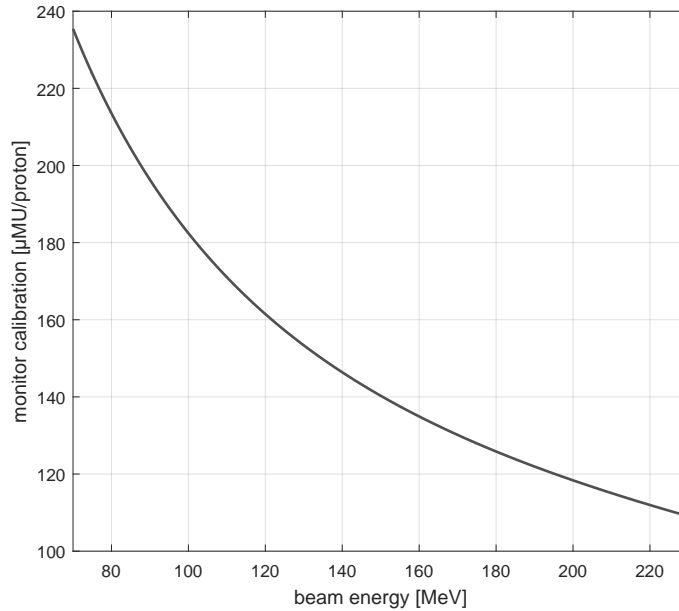


Figure 5.3: Calibration curve for the primary ionization chamber correlating internal monitor units (MUs) to absolute number of protons for different beam energies.

5.2.4 Tolerances for instantaneous beam current

From equations 5.4 and 5.6 we can immediately calculate the tolerance for fluctuations in the beam-on time:

$$\delta t_{\max} = \frac{\delta D_{\max}}{I_{\max}} = 3 \text{ ms.} \quad (5.7)$$

In addition, we would like to specify a margin for the instantaneous beam current to define a tolerance band similar to the one depicted in figure 5.4 below. In a worst case error scenario, the beam current would follow the red arrow in figure 5.4: It would increase by δI at the very end of the irradiation and remain on for δt although we would expect zero beam current at that point. The excess dose must be below 1500 MU, hence

$$(I_{\max} + \delta I) \delta t \leq 1500 \text{ MU.} \quad (5.8)$$

We can fulfill this criterion, by choosing a δI of 50 MU/ms and a δt of 2 ms. Note that we chose a smaller value here for the tolerance δt compared to equation 5.7, since we need to consider the time it takes to switch off the beam after a violation of an error band has been detected (typically ~ 0.3 ms).

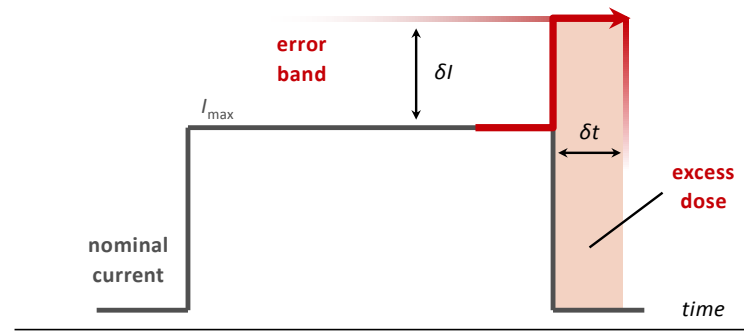


Figure 5.4: Schematic of the upper beam current tolerance band comprising margins in time (δt) and current (δI).

5.2.5 Tolerance for beam position

The homogeneity of dose distributions is very sensitive to misplacements of the beam in the transverse plane. Small inaccuracies can yield areas of significantly higher and lower dose concentration with respect to the prescription. As such, the supervision of the transverse beam position requires a strict tolerance.

Let us assume a square ($10 \times 10 \times 10$) cm^3 target volume filled with water that we plan to irradiate to 1.818 Gy. A simple treatment plan could foresee 25 different

iso-energy slices, each filled with straight lines delivering uniform dose. Figure 5.5 below visualizes this example case. If we assume a 1 mm deviation in position that is localized within a single dose calculation voxel ΔV , the resulting differences in planned and delivered dose distribution will be of the order of ± 30 mGy (without derivation). Hence, we conclude that errors in the transverse beam position should be smaller than ± 1 mm.

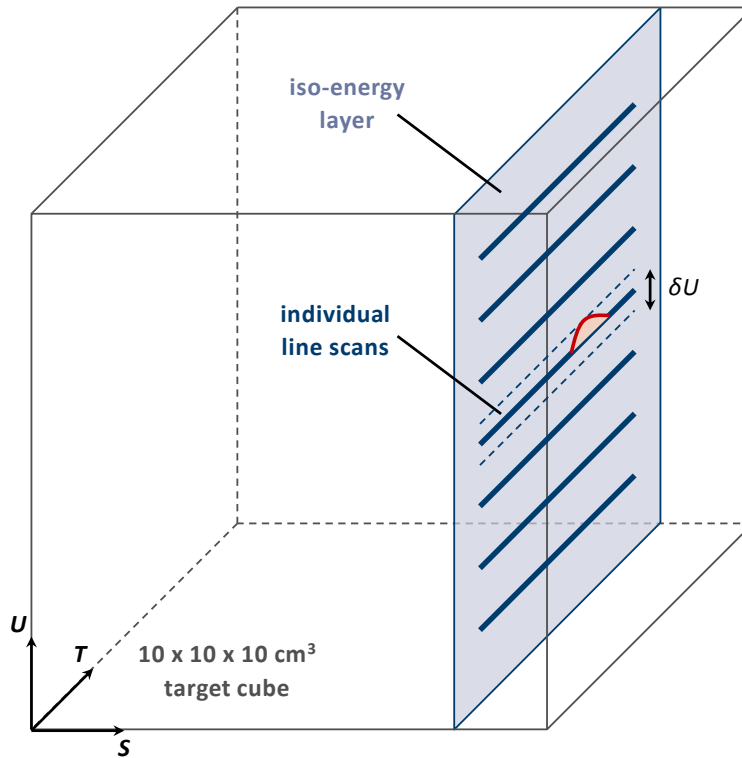


Figure 5.5: Example for an error in the transverse beam position (deviation from the planned beam position indicated in red).

5.3 Discussion of safety tolerances

We have derived a set of beam monitoring tolerances for line scanning irradiations in proton therapy from fundamental dosimetric considerations. These tolerances, combined with effective safety measures that terminate the irradiation in case of errors, facilitate complying with safety constraints given by international norms and guidelines. Although actual tolerance values may be specific to line scanning irradiations using a proton beam, we are confident that they could be derived in a very similar way for different particles (e.g. helium or carbon ions) and different beam scanning techniques (e.g. spot or raster scanning).

5.3.1 Definition of erroneous delivery

In the definition of an erroneous delivery we use an absolute value of ± 36 mGy. In our patient history we have very few cases, in which the prescribed dose for a single session is below 1.818 Gy. Thus, we can satisfy the $\pm 2\%$ criterion for almost all patients. Numerous studies actually suggest that a treatment with fewer sessions and higher dose per session could be advantageous for radio-resistant tumors, especially when irradiating with carbon ions. In such cases, the ± 36 mGy threshold would actually correspond to a relative tolerance smaller than $\pm 2\%$.

5.3.2 Maximum dose deposition of a proton beam

The height of the on-axis Bragg curves in figure 5.2 depends on the voxel size ΔV and the contained material. The average dose deposition increases with increasing material density and decreasing voxel size. For infinitesimally small volumes dV , the value for the maximum dose deposition amounts to ~ 5 nGy/proton. Nevertheless, we would argue that a finite volume of 40 mm^3 , as used in our derivation, is well below typical sensitive volumes of standard ionization chambers (e.g. 600 mm^3 for PTW Farmer chamber type 30010). And we think that all tolerances should be defined based on quantities that are actually measurable with standard dosimetry equipment.

5.3.3 Tolerance for dose deposition

We regard the tolerance δD_{\max} (see equation 5.6) as an important tool against systematic over or under-dosage (e.g. beam current in figure 5.4 constantly too high or too low). To verify it during the irradiation of a line, we added an integration unit in the readout electronics of one of our parallel-plate ionization chambers. As such, it monitors the total number of delivered MUs (or protons) as function of time rather than the instantaneous beam current. Hence, we can immediately abort the irradiation whenever a violation of δD_{\max} has been detected. Dedicated firmware features of this tool are described elsewhere (Klimpki et al., 2018).

5.3.4 Tolerance for instantaneous beam current

We use the remaining ionization chamber to monitor the instantaneous beam current I . The noise level of the chamber mainly determines the value for δI . On the one hand, it is desirable to decrease δI as much as possible to guarantee high safety standards, but, on the other hand, a low δI can become very impractical if the treatment of a patient is interrupted too frequently.

From equation 5.8 we see that δt is directly correlated to the maximum authorized beam current I_{\max} , with which patients can be irradiated. Efforts in decreasing the irradiation times even further often suggest increasing I_{\max} (by roughly a factor 10).

To guarantee the same level of safety, δt would need to be lowered in that case. We think that a value of 200 μs could still be practical considering all delays and reaction times of our beamline and controls.

5.3.5 Tolerance for beam position

In our opinion, the tolerance for the transverse beam position (± 1 mm) represents the strongest constraint. Because therapeutic beam currents are generally low compared to many experimental beamlines, signals in position-sensitive monitors often suffer from high noise levels. Furthermore, these monitors need to be as non-destructive as possible in order to avoid deteriorations in the beam quality. As such, their spatial resolution is limited to μm -thin readout channels every one or two millimeters. Following the ALARA principle (as low as reasonably achievable), many centers increase their position tolerance (e.g. to ± 1.8 mm at MD Anderson Cancer Center, Houston, TX, USA (Smith et al., 2009)). Other viable approaches are adapting the tolerance according to the beam energy (and, thus, beam size in air) or to use indirect measures on beam position such as the field strength of the scanner magnets (our approach for line scanning). The latter comes at the advantage of exhibiting a stable signal-to-noise ratio independent of the proton beam current, but it provides an indirect measurement of the transverse beam position only.

5.4 Conclusion

We provided a set of tolerances and their derivation for line scanning irradiations in proton therapy. We consider patient treatments in line scanning mode safe, when supervising those tolerances frequently (in our case every 10 μs) during the irradiation.

Acknowledgment

The authors would like to thank C. Winterhalter (PSI) for performing the Monte Carlo simulations.

6

The impact of pencil beam scanning techniques on the effectiveness and efficiency of rescanning moving targets

G. Klimpki^a, Y. Zhang^a, G. Fattori^a, S. Psoroulas^a, D.C. Weber^{a,b,c},
A. Lomax^a, D. Meer^a

^a Paul Scherrer Institute (PSI), Center for Proton Therapy,
5232 Villigen PSI, Switzerland

^b University Hospital Zurich, Department of Radiation Oncology,
Rämistrasse 100, 8091 Zurich, Switzerland

^c University Hospital Bern, Department of Radiation Oncology,
Freiburgstrasse 18, 3010 Bern, Switzerland

Physics in Medicine and Biology

submitted on December 22 (2017)

preprint

Abstract

Therapeutic pencil beams are typically scanned using one of the following three techniques: spot scanning, raster scanning or line scanning. While providing similar dose distributions to the target, these three techniques can differ significantly in their delivery time sequence. Thus, we can expect differences in effectiveness and time efficiency when trying to mitigate interplay effects using rescanning. At the Paul Scherrer Institute, we are able to irradiate treatment plans using either of the three delivery techniques. Hence, we can compare them directly with identical underlying machine parameters such as energy switching time or minimum/maximum beam current. For this purpose, we selected three different liver targets, optimized plans for spots – on the end-exhalation phase of the 4D CT – and converted them to equivalent raster and line scanning plans.

In addition to the scanning technique, we varied the underlying motion curve, starting phase, prescription dose and rescanning strategy, which resulted in a total of 1584 4D dose calculations and 49 measurements. They indicate that rescanning becomes effective when achieving a high number of rescans for *every* dose element. Fixed minimum spot weights for spot and raster scanning machines often hamper this. By introducing adaptive scaling of the beam current within iso-energy layers for line scanning, we can flexibly lower the minimum weight whenever required and achieve higher rescanning capability. Averaged over all scenarios studied, volumetric rescanning is significantly more effective than layered provided the same number of rescans are applied. Fast lateral scanning contributes to the efficiency of rescanning. We observed that in any given time window, we can always perform more rescans using raster or line scanning compared to spot scanning irradiations. Thus, we conclude that line scanning represents a promising technique for rescanning by combining both effectiveness and efficiency.

6.1 Introduction

Particle therapy centers increasingly use the method of pencil beam scanning (PBS), as defined by Flanz (2011), to distribute dose in the tumor volume. Meer and Psoroulas (2015) showed that by the end of 2014, almost 50% of all particle therapy gantries around the world were equipped with PBS technology. In PBS, a pair of scanner magnets deflects the beam in the lateral plane. In addition, the beam energy can be modified to successively change the penetration depth of the beam. By alternating lateral scans and changes in energy, particles and their dose deposition can be distributed throughout the three-dimensional tumor volume.

The beam scanning process in the lateral plane is typically performed in three different ways: using spot scanning, raster scanning or line scanning¹. Spot scanning was introduced clinically by Pedroni et al. (1995) at the Paul Scherrer Institute (PSI) and has also been adopted in the first-generation scanning system at the MD Anderson Cancer Center (Smith et al., 2009) as well as at the Massachusetts General Hospital (Grassberger et al., 2013). Raster scanning, on the other hand, was first introduced by Haberer et al. (1993) at the Gesellschaft für Schwerionenforschung (GSI). Many facilities treating with carbon ions, e.g. HIT in Germany (Haberer et al., 2004), NIRS in Japan (Furukawa et al., 2010b) and CNAO in Italy (Giordano et al., 2015), make use of the raster scanning technique. Line scanning was introduced recently by PSI (Zenklusen et al., 2010) and Sumitomo Heavy Industries, Ltd. (Inoue, 2014) and is used clinically at Samsung Medical Center, Seoul, South Korea (Kwangzoo et al., 2015). Spot and raster scanning systems are also offered by a number of industrial vendors (e.g. IBA, Hitachi or Varian).

These three scanning techniques may differ in performance, but they all exhibit increased sensitivity to periodic, intra-fractional motion (e.g. breathing, heartbeat, intestinal activity) compared to passive scattering irradiations. The reason for this is the motion of the patient anatomy that interferes with the motion of the particle beam. Resulting interference or so-called interplay patterns/effects – hot and cold spots in the delivered dose distribution – can be mitigated in various ways (Bert and Durante, 2011). Rescanning is one of the investigated methods: the idea, suggested decades ago, is to irradiate the same field multiple times with proportionally reduced dose to blur out interplay patterns (Phillips et al., 1992). This approach requires increased margins of the target that encompass its motion, but it imposes relatively low technical demands on the beam delivery system compared to e.g. tumor tracking (Riboldi et al., 2012).

Published studies identify numerous factors that influence the effectiveness of rescanning such as motion amplitude (Bert et al., 2008; Schätti et al., 2013), motion

¹Wobbling is not considered here as it requires patient-specific hardware such as collimators and compensators.

estimation (Zhang et al., 2012), beam width (Grassberger et al., 2013), tumor size (Zenklusen et al., 2010) or rescanning type (Schätti et al., 2013; Bernatowicz et al., 2013; Grassberger et al., 2015). Furthermore, they reveal a strong dependence of the efficiency of rescanning on the beam delivery system (Furukawa et al., 2010a; Schätti et al., 2014) and the integration into the clinical workflow (Mori et al., 2014a,b). All these studies have in common that their findings are coupled to the underlying beam scanning technique. Even though Bernatowicz et al. (2013) and Dowdell et al. (2013) varied the characteristics of beam delivery for spot scanning in simulation studies, we still lack a comprehensive comparison of the three scanning techniques available and their impact on rescanning under identical irradiation conditions (same accelerator, dose rate, beam size etc.). On the second-generation gantry at PSI, so-called Gantry 2, we have the unique opportunity to irradiate patient plans in either spot, raster or line scanning mode. Hence, we can directly compare these three techniques and their impact on rescanning under identical irradiation conditions.

For this purpose, we conducted a comparative study on the effectiveness and efficiency of spot, raster and line scanning to mitigate interplay effects using rescanning. We investigated three liver targets following two different (patient-specific) breathing curves. Furthermore, we varied the fraction dose, the starting phase as well as the type and the amount of rescans. By studying the impact of all these parameters on simulated and measured dose distributions, we wish to answer the following three questions:

- How do magnitudes of interplay patterns compare across the different scanning techniques?
- Which technique is most effective or efficient when combined with rescanning?
- Is there a preferred scanning technique when mitigating motion using rescanning?

Within this study, we developed a treatment plan converter that translates plans optimized for spot scanning to raster and line scanning plans of similar quality. All plans are deliverable on Gantry 2, which, for experimental purposes, can perform irradiations in all three scanning modes.

6.2 Materials and methods

6.2.1 Beam delivery techniques

In *spot scanning*, lateral pencil beam positions are discretized on a rectilinear grid. For beams in anterior/posterior direction, the lateral (T, U)-plane coincides with the coronal plane of the patient. The number of protons delivered to every grid point (or spot) is simply given by the dwell time of the beam. Before switching from one spot to another, the beam is turned off completely, which results in roughly 3 ms dead

time between spot transitions (value for PSI Gantry 2). The distance between grid points can, in principle, vary as function of beam energy. However, to be consistent with our clinical protocol, we selected fixed grid distances of $\Delta T = \Delta U = 4$ mm. *Raster scanning* follows the same rectilinear grid, but the beam remains on when moving from one grid point to the next. As such, raster scanning saves dead time at the cost of introducing small transient doses. When the distance between two prescribed beam positions exceeds an upper limit (here 10 mm), a beam-off command needs to be issued nonetheless. *Line scanning* is fully continuous in T -direction and not bound to any grid constraints in this dimension. The delivered dose can be modulated by changing the scan speed and beam current dynamically during irradiation. The beam is switched off only when changing U -position. Due to different control mechanisms in spot and line scanning, we expect an increased dead time between two lines of roughly 7.9 ms. Figure 6.1 exemplifies how the same iso-energy layer would be delivered in spot scanning (left), raster scanning (middle) and line scanning mode (right).

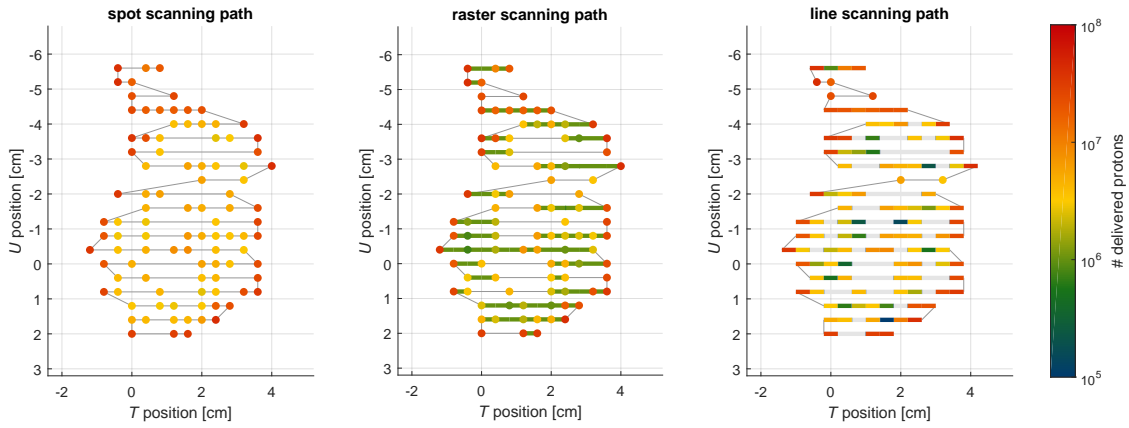


Figure 6.1: Scan paths for all three scanning techniques: spot scanning (left), raster scanning (middle) and line scanning (right). The three illustrations represent the same iso-energy slice ($E = 151$ MeV) of patient \mathcal{P}_3 (see table 6.1). Beam weights were optimized for a total field dose of 0.606 Gy.

6.2.2 Patient cases and treatment plans

The patient data set comprises three-dimensional computed tomography scans (3D CTs) of liver tumors stemming from three different patients as well as four-dimensional magnetic resonance imaging (4D MRI) under free breathing (Zhang et al., 2016). The delineation of the clinical target volumes (CTVs) was based on the 3D CTs. From each 4D MRI, we extracted patient-specific motion vector fields over the entire period of image acquisition. To simulate target motion under breathing, we applied these vector fields to the static 3D CT using deformable image registration. This procedure was introduced and described in more detail by Boye et al. (2013). Table 6.1 shows how we combined three 3D CTs and two 4D MRIs in this

study. Fairly small density variations inside the liver facilitate purely geometric target expansion to encompass the full extent of the CTV motion (Knopf et al., 2013). All treatment plans were optimized for homogeneous coverage of the resulting geometrical internal target volumes (gITVs).

Table 6.1: gITV sizes for all six combinations of 3D CT geometry and 4D MRI motion.

	motion data ^a \mathcal{M}_1 : $\langle A_{pp} \rangle = (5.1 \pm 1.3)$ mm $\langle \tau \rangle = (3.2 \pm 0.3)$ s	motion data ^a \mathcal{M}_2 : $\langle A_{pp} \rangle = (16.9 \pm 2.4)$ mm $\langle \tau \rangle = (6.6 \pm 0.8)$ s
patient data ^b \mathcal{P}_1 : CTV of 95 cm ³	148 cm ³	184 cm ³
patient data ^b \mathcal{P}_2 : CTV of 220 cm ³	313 cm ³	382 cm ³
patient data ^b \mathcal{P}_3 : CTV of 340 cm ³	458 cm ³	528 cm ³

^a obtained from 4D MRI; ^b obtained from 3D CT.

We chose a three-field arrangement for all six target volumes with conventional (2 Gy (RBE) per fraction) and hypo-fractionated irradiation scheme (6 Gy (RBE) per fraction). Each of the three fields was optimized for homogeneity separately (single-field uniform dose approach). Only the anterior-posterior field was considered in this comparison study (to limit the amount of variable parameters) and was prescribed doses of 0.606 Gy and 1.818 Gy, respectively. All plans were optimized for spot scanning on a (4×4) mm² rectilinear spot grid. Figure 6.2 shows static dose distributions at the center of the spread-out Bragg peak for all three patients included in this study. Raster and line scanning plans were created by converting the original spot scanning plan to the corresponding scanning technique (see subsection 6.2.4 below). A 3D re-optimization on the patient anatomy to account for the different delivery scenarios was not performed.

6.2.3 Rescanning strategy

To investigate the effectiveness of each scanning technique in mitigating tumor motion using rescanning, we split the field dose of every plan in 2, 4, 6, 8 and 10 scans (R_{nom}). However, we respected the smallest deliverable number of protons $N_{p,\text{min}}$ when scaling the dose by evaluating the possible number of rescans $[R_i]$ separately for every dose element as follows:

$$[R_i] = \min \left\{ \left\lfloor \frac{N_{p,i}}{N_{p,\text{min}}} \right\rfloor, R_{\text{nom}} \right\}. \quad (6.1)$$

As such, not all dose elements can receive the full number of anticipated rescans R_{nom} , with elements with very low initial weights being rescanned less than elements with high initial weights. We considered both layered and volumetric rescanning sequences (Bert and Durante, 2011), which resulted in a total of 36 static and 360 motion plans.

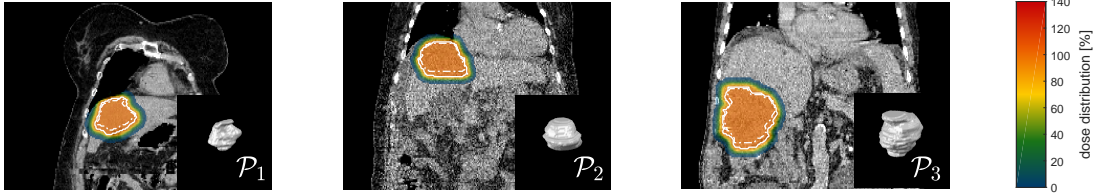


Figure 6.2: Static dose distributions for patients \mathcal{P}_1 (left), \mathcal{P}_2 (middle) and \mathcal{P}_3 (right). The CTV (dashed contour) was enlarged according to motion \mathcal{M}_1 . All plans were optimized for spot scanning on the resulting gITV (solid contour). The insets show 3D renders of the CTV.

6.2.4 Treatment plan conversion

In order to compare the different scanning techniques quantitatively, we developed a treatment plan converter that translates spot scanning plans to raster and line scanning plans. The converter respects all machine-related constraints such as maximum and minimum dose rate or maximum beam scanning speed and, thus, produces realistic and deliverable plans. In a first step, the converter groups all spots placed on straight lines (same U -position and same energy) and calculates their nominal fluence profile in water². In case of raster scanning, transient dose contributions between spots are added and the original spot weights are decreased to preserve the total number of delivered protons. In case of line scanning, segments of constant scan speed and beam current are defined to enable continuous motion of the beam in T -direction. Created line segments stretch from one midpoint between two spots to the next. In case of less than three spots per line, we keep the individual beam spots. Raster and line scanning fluence profiles obtained in this fashion deviate from the nominal spot scanning profile. Hence, we added an iterative matching step based on non-linear least squares that recalculates beam weights for all raster and line segments under the constraints of optimal fluence matching to those of the initial spot scanning plan.

To be compatible with most raster scanning installations, we assign a fixed beam current to every raster scanning path. Each path is interrupted only when changing U -position or if the change in T -position exceeds 10 mm (gap in the scan path).

²The width of the pencil beam for this calculation resembles the pencil beam width in water at the Bragg peak including both phase space and scattering contributions.

The former reason for interruptions is due to a limitation in our control system, the latter is common practice to prevent large transient doses. In line scanning, we allow for frequent modulation of the beam current during a single line. Hence, we can avoid interruptions due to gaps in the scan path by suppressing the beam current completely in those regions. The different handling of gaps in raster and line scanning mode can be seen in figure 6.1.

The maximum (minimum) point-to-point dose difference between translated raster and nominal spot scanning plans amounts to +2.7% (−2.4%). The vast majority (95%) of all point-to-point dose differences is much smaller and ranges between +0.6% and −0.8% with a median difference of 0.0%. The agreement for line scanning is similar: the maximum (minimum) difference among all translated plans amounts to +1.8% (−2.1%) and the 95% interval spans from +0.9% and −0.4% (median difference 0.2%).

6.2.5 4D dose calculation

We use time-resolved dose calculations to estimate the magnitude of dose deterioration due to motion of the anatomy during irradiation. Our dose calculation uses the motion vector field extracted from the 4D MRI to deform the dose calculation grid as function of time. Based on warped 3D CT information, water-equivalent path lengths and density information are adapted for every point in time. The anatomy, however, is assumed to be stationary during the irradiation of a single spot (\sim few milliseconds duration). A full description of the algorithm was provided by Boye et al. (2013). We recently validated it against measurements (Krieger et al., 2018).

The 4D dose calculation was originally developed for spot scanning irradiations and supports input in form of spot lists only. Thus, we deconvolved raster and line scanning plans back to extended lists of discrete spots. To represent the dose deposition accurately, we decreased the spot grid in the T -direction down to 1 mm. In this way, we could mimic (quasi-)continuous irradiations and provide compatible input to our validated 4D dose calculation algorithm.

In addition to (extended) spot lists, the 4D dose calculation requires timestamps for every entry. These timestamps indicate how much time has passed between the overall start of the irradiation and the start of the current spot. To have precise estimates on relevant system delays and performance parameters, we analyzed machine log files from patient irradiations on Gantry 2 and derived a timing model. Input parameters to this model are listed in table 6.2. E.g. irradiating a spot with 10^7 protons at 150 MeV requires

$$t_{\text{spot}} = 10^7 \times \frac{(1.602 \times 10^{-19} \text{ C})}{(400 \times 10^{-12} \text{ A})} \cong 4 \text{ ms} \quad (6.2)$$

with our maximum beam current (currently limited by radiation protection considerations). For each spot transition, we accumulate 2.83 ms of dead time on average. Hence, the next spot in the same energy layer will start 6.83 ms later. When changing the beam energy we have to account for another 106 ms dead time on average. Irradiations at low energies are affected by a drop in the beamline transmission and, therefore, the irradiation time t_{spot} increases. Such effects are considered in our timing model and characterized through an energy-dependent look-up table.

Based on predicted timelines for all 396 plans, we calculated dose distributions for four different starting phases of the motion cycle resulting in 1584 4D dose calculations in total. In addition, we performed conventional dose calculations for all 36 static plans on the reference 3D CT.

Table 6.2: Specifications of the Gantry 2 beam delivery system at the Paul Scherrer Institute.

	70 MeV	150 MeV	230 MeV
max. clinically used beam current ^{c,d} [pA]	65	400	514
min. clinically used beam current ^c [pA]	24	40	51
min. spot weight [10^5] for spot/raster scanning ^c	2.8	4.6	6.0
min. equiv. weight [10^5] for line scanning ^e	0.6	1.0	1.3
max. stable and reproducible scan speed in T -direction		1 cm/ms	
mean dead time between two spots		2.83 ms	
mean dead time between two lines		7.90 ms	
mean dead time between energy changed		106 ms	
mean ramping time of the beamline ^f		9.3 s	

^c energy-dependent; ^d transmission-dependent;

^e distributed 4 mm at maximum scan speed and minimum beam current; ^f occurs when resetting all beamline elements between two volumetric rescans.

6.2.6 Measurement devices and setup

Absolute dose distributions were measured with a 2D array of ionization chambers placed at iso-center (PTW *seven29*), whilst relative ones were measured with a scintillation screen coupled to a CCD camera (Schätti et al., 2013). To be in agreement with our standard quality assurance workflow, we applied a constant output-scaling factor of 2% (Pedroni et al., 2005) to all dose distributions measured with the PTW *seven29*. Both dosimeters could be moved with the QUASAR™ Respiratory Motion Platform during irradiation. It was programmed to reproduce patient-specific, rigid motions at the iso-center, as extracted from the 4D MRIs. All measurements were taken at 11 cm water-equivalent depth, which marks the center of the spread-out Bragg peak for patient \mathcal{P}_3 . Krieger et al. (2018) provide a more detailed description of the experimental setup.

6.2.7 Quantification metrics

We assessed the efficiency and effectiveness of spot, raster and line scanning based on the following three metrics:

- (i) the total irradiation time t ,
- (ii) the dose inhomogeneity $d_{5/95}$ defined as

$$d_{5/95} := \frac{D_{5\%} - D_{95\%}}{D_{\text{field}}}, \quad (6.3)$$

with the greatest dose $D_{5\%}$ which all but 5% of the CTV receives, the least dose $D_{95\%}$ received by at least 95% of the CTV and the prescribed field dose D_{field} (International Commission on Radiation Units and Measurements, 2007),

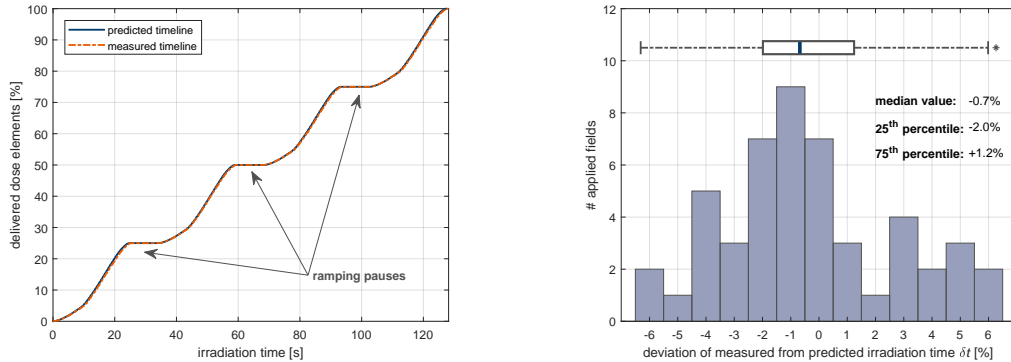
- (iii) and the effective number of rescans R_{eff} defined as the average over all rescans per dose element $[R_i]$ (see equation 6.1).

6.3 Experiments and results

All absolute and relative dose measurements were conducted for patient \mathcal{P}_3 in combination with motion \mathcal{M}_1 . We applied various different rescanning factors to the static plan and used both layered and volumetric rescanning sequences to mitigate for target motion. Based on these measurements, we validated the timing model of the machine, the treatment plan converter as well as the 4D dose calculation engine for the different beam scanning techniques (subsections 6.3.1 to 6.3.3). The results of the 4D dose calculations are provided in subsection 6.3.4. A final experimental validation of the effectiveness and efficiency of rescanning can be found in subsection 6.3.5.

6.3.1 Experimental validation of the timing model

The Gantry 2 timing model, as described in subsection 6.2.5, is used as input to the 4D dose calculation algorithm. To have accurate estimates of the resulting interplay pattern, the timing model has to match the performance of the machine. We validated our model against 49 irradiations on Gantry 2, from which the default machine log files could be used to reconstruct the actual irradiation sequence and delivery timestamps (see figure 6.3(a)). The deviations of predicted and measured irradiation time are shown in figure 6.3(b). We see that 95% of all observed deviations are within -6.3% and $+6.0\%$, with a median deviation of -0.7% .



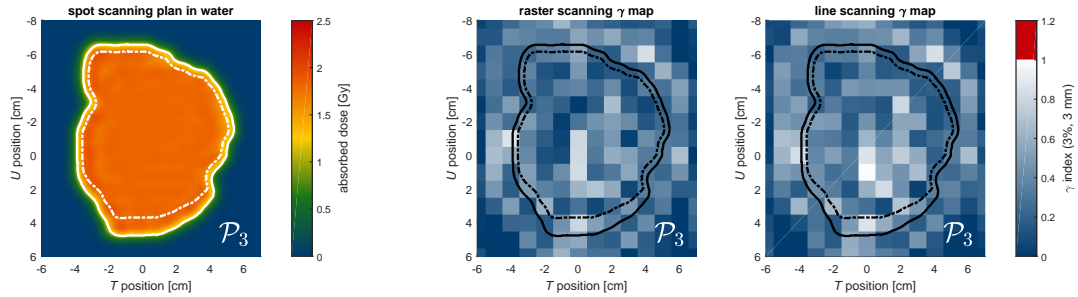
(a) When rescanning patient \mathcal{P}_3 (1.818 Gy field) four times volumetrically using line scanning, the difference between measured and predicted irradiation time is below 1 s.

(b) For spot, raster and line scanning, 95% of all observed deviations between predicted and measured irradiation time are within -6.3% and $+6.0\%$, with a median deviation of -0.7% .

Figure 6.3: Deviations of the Gantry 2 timing model from actual machine performance for 49 irradiated fields.

6.3.2 Experimental validation of the plan converter

To demonstrate validity of the plan converter, we selected patient \mathcal{P}_3 and recalculated the dose distribution of the 1.818 Gy spot scanning field in water (see figure 6.4(a)). We defined 11 cm as reference depth, since it marks the center of the spread-out Bragg peak. Using the PTW array, we measured absolute dose distributions at a water depth of 11 cm for raster and line scanning irradiations of the same field under static conditions. To compare measured dose distributions to the plan reference, we applied the γ -method introduced by Low et al. (1998) with a distance-to-agreement of 3 mm and a dose-to-agreement of 3%. The resulting maps are shown in figure 6.4(b). We observe that all irradiations pass the criteria with 100%.



(a) Recalculated spot scanning plan of patient \mathcal{P}_3 in 11 cm water depth (1.818 Gy field). (b) γ -maps of absolute dose measurements for raster (left) and line scanning (right) with respect to the recalculated spot scanning plan.

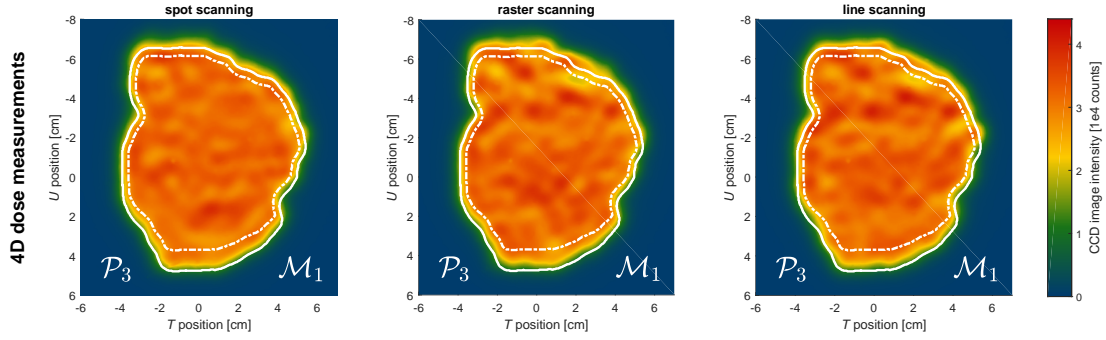
Figure 6.4: Quantitative comparison of calculated and measured dose distributions in water. The overall γ pass rate is at 100% in all cases. The dashed (solid) line represents the CTV (gITV) contour.

6.3.3 Experimental validation of the 4D dose calculation engine

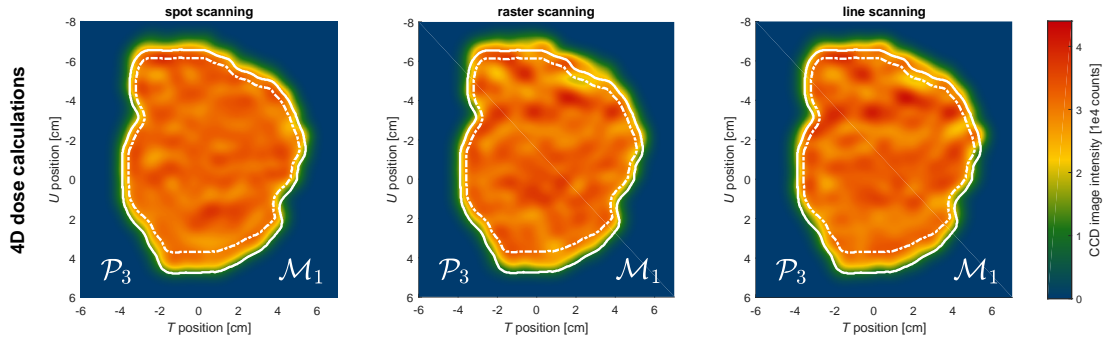
Although we recently validated our 4D dose calculation algorithm for spot scanning irradiations (Krieger et al., 2018), we wished to confirm the temporal validity of the dose calculation engine for raster and line irradiations, since these two scanning techniques comprise continuous movements of the proton beam. For this purpose, we acquired relative dose distributions in 11 cm water-equivalent depth with a CCD camera placed on a moving platform (see subsection 6.2.6 for a detailed description of the setup). We irradiated the 1.818 Gy field of patient \mathcal{P}_3 under motion \mathcal{M}_1 in all three delivery modes (no rescanning applied). The start of the irradiation was precisely synchronized to the start of the breathing curve using optical tracking of the motion platform (Fattori et al., 2017). Figure 6.5(a) shows the measured interplay patterns, which differ across the different scanning techniques. Using machine and motion log files as well as quenching-corrected Bragg curves, we calculated the expected dose distributions using our 4D dose calculation engine (see figure 6.5(b)). All γ -maps between measured and calculated interplay patterns pass the (3% | 3 mm)-criterion with over 99%.

6.3.4 Results of 4D dose calculations

In order to study the effectiveness and efficiency of the different scanning techniques for motion mitigation using rescanning, we have analyzed the results of all 1584 4D dose calculations using the metrics described in subsection 6.2.7. In particular, we considered the influence of the effective number of rescans R_{eff} and the influence of the rescanning sequence (layered vs. volumetric) on effectiveness as well as the influence of the scanning technique (spot vs. raster vs. line scanning) on efficiency.



(a) Measured 4D dose distributions.



(b) Calculated 4D dose distributions.

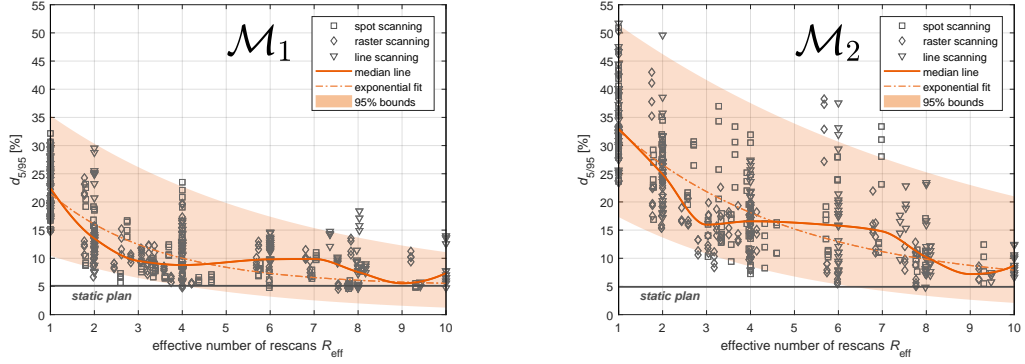
Figure 6.5: Comparison of measured (a) and calculated (b) interplay patterns for spot, raster and line scanning. We irradiated the 1.818 Gy field of patient \mathcal{P}_3 under motion \mathcal{M}_1 to a moving CCD camera. The 4D dose calculation, which was based on machine and motion log files as well as quenching-corrected Bragg curves, agrees with the measurement. The dashed (solid) line represents the CTV (gITV) contour.

Effectiveness of rescanning

We consider rescanning effective if it decreases inhomogeneities inside the target to close to the level of the static treatment plan ($d_{5/95} \sim 5\%$ for all targets). To quantify inhomogeneities, we calculated the $d_{5/95}$ inside the CTV as defined in equation 6.3 for all 4D dose calculations. The results for volumetric rescanning are shown in figure 6.6. We observe a decrease in inhomogeneity with increasing effective number of rescans R_{eff} . For motion \mathcal{M}_1 (\mathcal{M}_2), the median $d_{5/95}$ decreases from 22.43% (32.96%) for $R_{\text{eff}} = 1$ to 7.38% (8.73%) for $R_{\text{eff}} = 10$. Based on an analysis of variance, this trend is significant with $p \ll 10^{-10}$ for both motion cases. The scanning technique, starting phase, target size and field dose do not have a significant influence on the effectiveness of rescanning ($p > 0.1$). They contribute to the high fluctuations between the individual cases. For layered rescanning, we observed a less pronounced decrease in inhomogeneity with increasing R_{eff} (data not shown here).

In figure 6.7, we have plotted the $d_{5/95}$ of both rescanning sequences against each

6 The impact of PBS techniques on rescanning moving targets

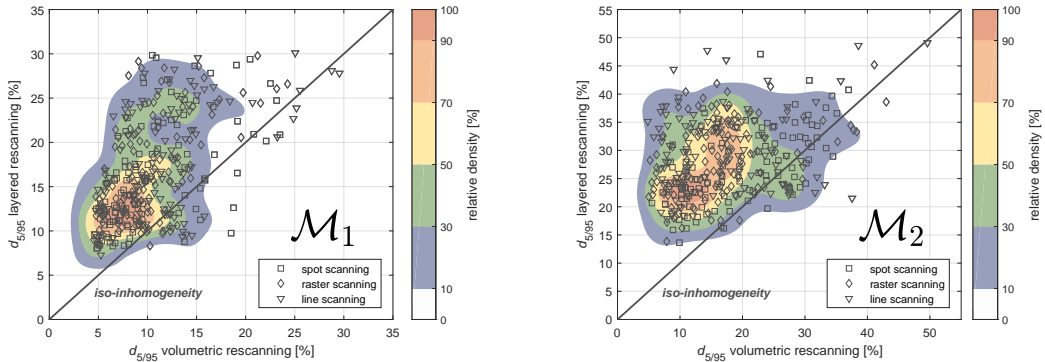


(a) Target inhomogeneity $d_{5/95}$ as a function of R_{eff} for motion \mathcal{M}_1 .

(b) Target inhomogeneity $d_{5/95}$ as a function of R_{eff} for motion \mathcal{M}_2 .

Figure 6.6: Target inhomogeneity $d_{5/95}$ of all 4D dose calculations concerning volumetric rescanning as a function of effective number of rescans R_{eff} . A high R_{eff} decreases target inhomogeneities significantly ($p \ll 10^{-10}$), whereas the scanning technique does not seem to influence the effectiveness of rescanning. The exponential bounds contain 95% of all data points and the solid curve indicates the median distribution.

other. Each point in the graph represents one combination of scanning technique, starting phase, field dose, target size and effective number of rescans. We observe that the density distributions of the point clouds are shifted away from the line of iso-inhomogeneity indicating larger target inhomogeneities when rescanning layer-wise. The differences between the layered and volumetric approach are significant with p -values below 10^{-10} . This observation holds for both motion scenarios \mathcal{M}_1 and \mathcal{M}_2 .



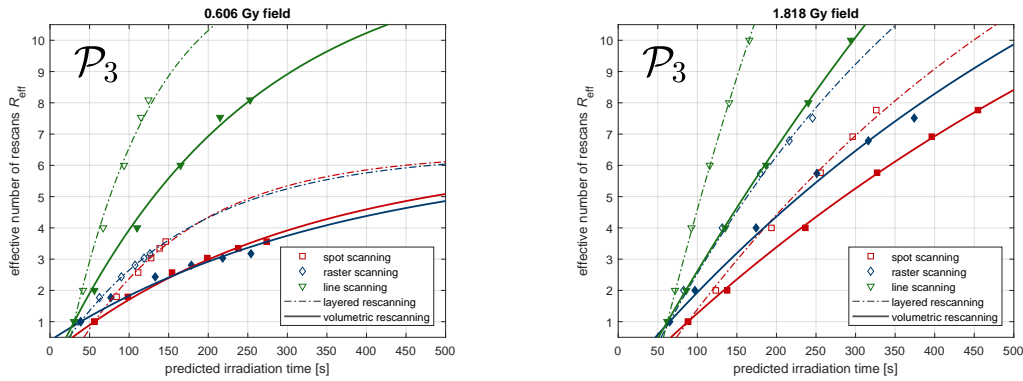
(a) Target inhomogeneities of layered vs. volumetric rescanning for motion \mathcal{M}_1 .

(b) Target inhomogeneities of layered vs. volumetric rescanning for motion \mathcal{M}_2 .

Figure 6.7: Data of all 4D dose calculations are shown in the two plots. The density of the point cloud is visualized in form of a color wash. We observe significantly higher inhomogeneities when rescanning layer-wise for both motion cases independent of the beam scanning technique.

Efficiency of rescanning

In the previous subsection we showed that a high R_{eff} is needed in order to decrease inhomogeneities inside the target. But increasing the number of rescans will also increase the total irradiation time, making rescanning inefficient. In other words, we observe a trade-off between effectiveness and efficiency. Figure 6.8 shows that the sweet spot shifts across the different scanning techniques. Line scanning represents the fastest technique and has the ability to reach high rescanning numbers in shorter time windows. We also see that spot and raster scanning show difficulties in reaching high R_{eff} values: they are limited to 6.4 effective rescans for the 0.606 Gy field of patient \mathcal{P}_3 , whereas line scanning can reach 12.8 effective rescans at maximum in this case. Last but not least, we observe that, despite being less effective for any given R_{eff} , layered rescanning is significantly faster than volumetric rescanning in all cases.



(a) R_{eff} as a function of predicted irradiation time t for patient \mathcal{P}_3 (0.606 Gy field).

(b) R_{eff} as a function of predicted irradiation time t for patient \mathcal{P}_3 (1.818 Gy field).

Figure 6.8: Layered rescanning is shown in dashed lines and volumetric rescanning in solid lines. Since \mathcal{P}_3 exhibits the largest gITV, differences in the irradiation times are most pronounced for this case.

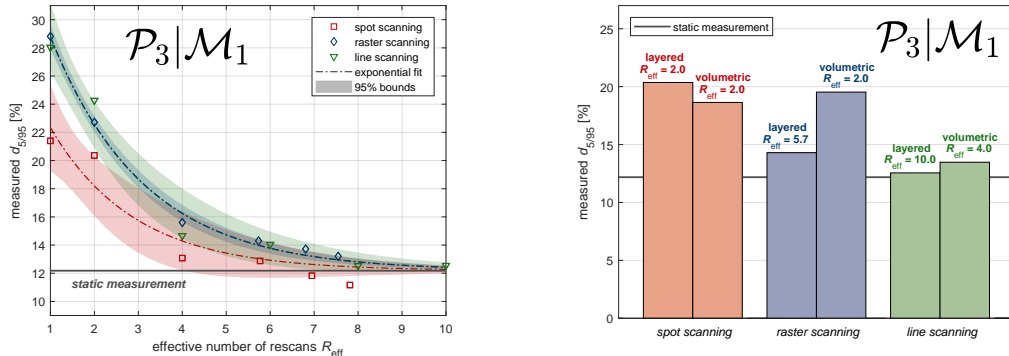
6.3.5 Experimental validation of effectiveness and efficiency

To confirm the efficacy of all scanning techniques experimentally, we irradiated the 1.818 Gy field of patient \mathcal{P}_3 to a CCD camera following the motion curve \mathcal{M}_1 . All dose distributions were measured in 11 cm water depth, which marks the center of the spread-out Bragg peak. We computed the $d_{5/95}$ inside the two-dimensional CTV contour shown in figure 6.5(a) and compared it to the value of the static irradiation (CCD camera at rest) in figure 6.9(a)³. We can confirm that rescanning – in this

³The absolute $d_{5/95}$ values of measurement and calculation should not be compared as the former represents one distinct layer in water whereas the latter stands for the entire CTV in patient anatomy.

case layer-wise – is effective, when reaching high values for R_{eff} . The overlapping confidence bounds of the exponential fits indicate that this observation is independent of the scanning technique. In this example case, spot scanning produces less interplay patterns in the unmitigated irradiation ($R_{\text{eff}} = 1$) than raster or line scanning.

If we impose a constraint on the total irradiation time t , we will not be able to deliver the same number of rescans with all three scanning techniques because of varying efficiency. As such, we chose to restrict t to twice the time it takes to deliver the static spot scanning plan (160s) and compare the measured inhomogeneities in figure 6.9(b). For this delivery time, layered rescanning is the most effective scenario for raster and line scanning, due to its faster delivery time and the higher R_{eff} that can be achieved within this time restriction. For spot scanning, two layered and two volumetric rescans yield similar mitigation strength with the latter being slightly more effective. With line scanning, we can reach the highest numbers of effective rescans, which reduces the $d_{5/95}$ almost to the value of the static measurement. With raster scanning, we would be able to deliver 5.7 effective rescans (layer-wise) which yields a similar strength in mitigation. The efficiency of spot scanning and volumetric raster scanning is not high enough to effectively mitigate for interplay effects in this example.



(a) The measured target inhomogeneity $d_{5/95}$ decreases as function of R_{eff} for all scanning techniques. Confidence bounds of the exponential fits overlap. We considered layered rescanning in this example.

(b) In a fixed time window (here 160s), line scanning (green bars) can deliver more effective rescans than spot (red bars) or raster scanning (blue bars), which helps to decrease target inhomogeneity.

Figure 6.9: Experimental validation of effectiveness (a) and efficiency (b) of rescanning based on measurements for the 1.818 Gy field of patient \mathcal{P}_3 in combination with motion \mathcal{M}_1 .

6.4 Discussion and outlook

We found that rescanning can be an effective tool for motion mitigation when repeatedly irradiating the *entire* tumor volume. All dose elements of the plan should be visited multiple times, since a high effective number of rescans is key to successful mitigation. However, not all scanning techniques facilitate applying dose elements with very low weight, which limits their rescanning capability. Line scanning – with its combined speed and intensity modulation – shows the greatest flexibility in this regard. We also observed that maximizing the effective number of rescans comes at the cost of increasing the total irradiation time. As such, rescanning appears to be most efficient when applied using the line scanning technique.

We observed a significant correlation between decrease in target inhomogeneity ($d_{5/95}$) and increase in effective number of rescans (R_{eff}) that is independent of the applied scanning technique. While this correlation generally holds for both motion curves studied, we found a much larger spread in the data points calculated for the larger motion extent (see figure 6.6). This observation could indicate that rescanning alone may not be effective for tumors that move with peak-to-peak amplitudes of the order of ~ 15 mm or more. These findings are in agreement with previous works (Schätti et al., 2013, 2014; Zhang et al., 2016). We should also note that dose inhomogeneity inside the target appears to be very case specific with rather high fluctuations for identical values of R_{eff} . Grassberger et al. (2015) also conclude that it is difficult to predict the number of rescans required for individual patients. Hence, individual 4D dose calculations and interplay analyses are encouraged prior to patient treatment.

The total irradiation time is another important factor that influences the effectiveness of mitigation. Averaging out interplay patterns over many breathing cycles may help to lower the $d_{5/95}$ (Zenklusen et al., 2010). This effect is certainly coupled to two of the main observations: (1) rescanning with a high R_{eff} is more effective than with a low one (see figure 6.6) and (2) volumetric rescanning is more effective than layered (see figure 6.7). In both cases, the more effective method exhibits a longer irradiation time. However, increased irradiation time alone cannot be the sole explanation for increased effectiveness as shown in figure 6.9(b). We see that, although having similar irradiation times, treatments with different R_{eff} and different rescanning sequences can indeed lead to varying $d_{5/95}$ values. Bernatowicz et al. (2013) and Schätti et al. (2013) came to similar conclusions.

Efficient rescanning requires fast lateral scanning (Grassberger et al., 2015), as provided by raster and line scanning, as well as fast energy changes when irradiating in volumetric sequences (Bernatowicz et al., 2013). On top of that, it necessitates a low minimum weight on applicable dose elements to ensure a high number of effective rescans. As such, adaptive scaling of the beam current at any given point in the

target provides an advantage (see table 6.2). In line scanning, we can regulate the current down to $\sim 10\%$ of its maximum value within less than $100\ \mu\text{s}$. This allows for adapting irradiation settings locally rather than having the need to fix them globally: many commercially available systems set the beam current for an entire iso-energy layer based on the lowest-weighted element contained in that layer. Such constraints impair the efficiency of rescanning significantly (see figure 6.8). Spot or raster scanning combined with adaptive beam current scaling could, in principle, reach the same R_{eff} values as line scanning. For spot scanning, however, this approach would come at the cost of a dramatically increased delivery time due to the accumulation of dead time.

In figure 6.7 we see, that volumetric rescanning is significantly more effective than layered rescanning. For the vast majority of data points – each representing one combination of target size, motion curve, starting phase, field dose and scanning technique – volumetric rescanning decreases target inhomogeneities further than layered. Several other studies support this result (Seco et al., 2009; Schätti et al., 2013; Zhang et al., 2016). On the contrary, Bernatowicz et al. (2013) and Grassberger et al. (2015) concluded an increased sensitivity of volumetric rescanning to so-called synchronization or resonance effects. It is worth mentioning that both of them used periodically repeated motion curves, which may trigger or, at least, enhance this observation. By using irregular, patient-specific motion curves that have been recorded for $> 70\ \text{s}$ (Zhang et al., 2016), we hope to obtain more realistic estimates on the effectiveness of rescanning.

We chose to base this study upon patients with liver tumors, because our experimental plan converter yields best results for fairly homogeneous targets. In such cases, the prerequisites for plan conversion are optimal: spots are placed on (mostly) uninterrupted lines and their weights change rather gradually. Hence, by limiting this study to liver targets, we could rule out bias originating from differences in the initial plans, but we also lack information on the influence of density heterogeneities in the beam path (e.g. as for lung tumors). Furthermore, we restricted all measurements to irradiations of a non-deformable target. Validation of 4D dose calculations based on such measurements may be eligible when considering fairly homogeneous targets, but may require additional tests in case of density heterogeneities. Nonetheless, the measurements helped to gain trust and confidence in our 4D dose calculation algorithm as they confirm the results derived from the calculations.

In our current implementation, we begin the treatment of any patient with a ramping scheme that clears the history of all magnets on the gantry ($\sim 10\ \text{s}$ duration). Afterwards, we start the irradiation with the highest energy in the plan and lower it successively. Between two volumetric rescans, we have to repeat this ramping scheme, which makes it much slower than layered rescanning despite having short energy switching times ($\sim 100\ \text{ms}$). By supporting successive upscaling of the energy in the control system, we could avoid these ramping pauses and e.g. decrease the ir-

radiation time in figure 6.3(a) from ~ 2 min. to $\sim 1\frac{1}{2}$ min. As such, the difference in efficiency between layered and volumetric rescanning would be minimized. Hence, we are currently implementing this variant of volumetric rescanning and plan to combine it with line scanning for patient treatments soon. Given that energy layer switching times for most commercial systems are much longer than those used in this work, we would hope that our efforts towards fast energy changes encourage manufacturers to pursue decreasing their energy layer switching times to facilitate volumetric rescanning.

6.5 Conclusions

Different pencil beam scanning techniques such as spot, raster or line scanning produce interplay patterns of comparable magnitude when irradiating moving targets. Motion mitigation using rescanning is most effective when achieving a high number of rescans for every dose element in the plan. While this observation is independent of the beam scanning technique, not all variants may be able to reach a high effective number of rescans due to technical constraints (e.g. lowest deliverable spot weight). In line scanning, we can adapt the beam current locally which facilitates delivery of very low doses with minimal compromise on the total irradiation time. Hence, we consider it an effective and efficient irradiation technique for rescanning.

Authors' contributions

GK performed experiments, analyzed the data and wrote the manuscript. YZ provided motion data, optimized treatment plans and calculated 4D dose distributions. GF supported execution of the measurements and provided optical tracking functionality. All authors commented on the paper and approved its final form.

Acknowledgments

The authors wish to thank the Massachusetts General Hospital for providing 3D CT data. Furthermore, they would like to express their gratitude to the Giuliana and Giorgio Stefanini Foundation for supporting this project. They declare they have no competing financial interests.

7

Discussion and outlook

This chapter summarizes and discusses the main results of all four publications. Section 7.1 provides an overview on the key findings and compares them, if applicable, with the literature. Furthermore, it highlights their uniqueness and implications. Section 7.2 reviews the tools and methods used in this dissertation critically by addressing their strengths and weaknesses. It scrutinizes the impact on the conclusions derived and emphasizes potential bias. Section 7.3 serves as an outlook to this dissertation by considering future perspectives of the line scanning technique and associated safety measures.

7.1 Overall results

This section summarizes the main results of each publication included in this thesis and evaluates their novelty and impact. Furthermore, it draws connections between the papers and discusses how they relate to each other. The beam monitoring system introduced in chapter 3 is addressed in subsection 7.1.1 and its technical implementation (see chapter 4) in subsection 7.1.2. Subsection 7.1.3 summarizes the derivation of safety margins for line scanning as demonstrated in chapter 5 and subsection 7.1.4 discusses a potential clinical application of line scanning (see chapter 6).

7.1.1 The design of a beam monitoring system

Chapter 3 elaborates on a two-stage beam monitoring system that guarantees safe patient treatments on Gantry 2 using the line scanning technique. Two partly re-

dundant safety levels supervise that the correct amount of protons will be delivered to the correct location inside the patient. The irradiation resumes seamlessly as long as the supervised quantities remain inside a clinically tolerable range. Upon detection of a tolerance violation, the beam monitoring system propagates an interlock to the patient safety system, which will terminate the irradiation immediately. As such, the monitoring system assures patient safety in case of unforeseen technical failures. Although arising dosimetric fluctuations may be measurable, their impact on the clinical outcome of the treatment is estimated to be negligible.

Safety level 1 supervises the transverse pencil beam position, the proton beam current and the total number of protons delivered over time. It receives signals from Hall probes and ionization chambers on a 100 kHz clock (thus every 10 μs) and compares them against predefined tolerances. As such, safety level 1 can react to failures or inaccuracies in real-time and has the ability to store precise information on the time and source of the interlock. Since it runs on separate software and hardware modules, level 1 monitoring is executed in the background and in parallel to the irradiation. It imposes minimal constraints on beam delivery and avoids dead times in the treatment usually required to perform safety checks. Safety level 2, on the other hand, is active between the application of two line scans. It validates the integral dose profile recorded with a position-sensitive strip monitor over the entire duration of a single line. As such, level 2 analyzes the combined effect of changes in the beam position and current. If the measured dose profile deviates from a modeled prediction (e.g. its center of gravity is off by more than ± 1.5 mm), level 2 can also issue an interlock that pauses the irradiation.

The combination of two safety levels represents a novelty in beam monitoring for particle therapy centers. Safety level 1 can react faster than any other monitoring system reported in the literature. They predominantly rely on frequent safety checks rather than supporting real-time beam monitoring. E.g. to supervise the transverse beam position, the National Center of Oncological Hadrontherapy in Pavia, Italy, reads out a strip and pixel monitor every 100 μs (Giordanengo et al., 2013). The Rinecker Proton Therapy Center in Munich, Germany, is slightly slower in reading out their strip monitor: every 250 μs (Borchert et al., 2008). The Heidelberg Ion-Beam Therapy Center (formerly Gesellschaft für Schwerionenforschung, Darmstadt) in Heidelberg, Germany, claims that they read out their multi-wire proportional chambers every 150 μs (Badura et al., 2000) to check whether the transverse beam position is still within tolerance. Less frequent safety checks yield longer reaction times in case of failures, which can directly translate into larger deviations from the prescribed dose distribution potentially compromising the quality of the treatment. A common compensation approach is to reduce the flexibility in beam delivery. In the examples given above, the change in transverse beam position would be restricted to ~ 1 mm between two readouts. While this constraint helps to minimize dosimetric errors in case of failures, it also compromises irradiation performance. As such, level 1 real-time beam monitoring can be regarded as minimally invasive to

the delivery unit. It opens up the possibility to change the transverse pencil beam position and beam current fast and frequently during the application of a single line. Chapter 6 demonstrates the positive consequence of this flexibility when irradiating moving targets using the rescanning approach. In principle, the monitoring system would be even general enough to cope with different particles (e.g. helium or carbon ions), different beam optics, or arbitrarily shaped scan paths (e.g. tumor contours).

Besides describing the conceptual design of the beam monitoring system, chapter 3 also includes a detailed description of the strip monitor calibration and software algorithm required for dose profile prediction. As such, the implementation of level 2 on the productive system was completed. Concerning level 1, however, necessary software enhancements to the control system and firmware modification to the read-out system amount to substantial and non-trivial work, which lead to the second publication included in this thesis (see chapter 4). The main results are discussed in the following section.

7.1.2 The hardware and firmware implementations

The section above explains the novelty of real-time beam monitoring in the context of particle therapy. Safety level 1 checks irradiation parameters more frequently than any other state-of-the-art therapy system. It supervises two ionization chambers mounted in the gantry nozzle and two Hall probes placed in the scanner magnets in real-time during irradiation. Realizing this technology on the Gantry 2 scanning system required substantial software and firmware enhancements. On the control software side, algorithms had to be developed that calculate upper and lower tolerance bands from the nominal delivery tables for beam position and current. These tolerance bands are then downloaded to the FPGA of the monitoring system prior to the application of each line scan, where they are interpolated in real-time to obtain upper and lower tolerance values for each incoming data sample. Besides interpolator and comparator unit, the firmware was enhanced by three additional features: (1) An integrator adds incoming data samples from one of the ionization chamber to a running counter. As such, the total number of particles delivered can be monitored over time in addition to the instantaneous beam current. This feature is a requirement derived from safety constraints (see chapter 5 and subsection 7.1.3 below.) (2) A violator propagates interlock signals to the patient safety system if the comparator detects values outside of the acceptable tolerance range. As such, the machine can be set to a safe state within $\sim 300 \mu\text{s}$ by switching off the proton beam. (3) Last but not least, a memorizer stores precise information on the time of the interlock and its origin for retrospective analysis. These values will be queried by the control software and stored in the machine log file. In addition, logging tables at full $10 \mu\text{s}$ time resolution will be saved for every supervised detector to analyze the trend of the recorded signals.

Chapter 4 describes the signal flow during irradiation and the software and firmware

enhancements in great detail. Additionally, it demonstrates their functionality based on three exemplary failure scenarios simulating position, current and dose errors. In each scenario, a safe state could be recovered within 300 μs or less. Interlocks are propagated as specified and the recorded logging tables are in good agreement with the anticipated behavior of the system. However, failure scenarios are difficult to provoke on the productive system without risking hardware damage. As such, all tests have been carried out in a dedicated test environment, which has been used previously for the commissioning of Gantry 2. Since it emulates the response of the productive system very accurately, results obtained and conclusions drawn will also be valid in the clinical environment. Tests conducted on the productive system after the submission of the second paper confirmed this assumption: All implemented interlock lines are responsive and able to turn off the beam reliably. Subsection 7.2.6 below demonstrates that.

In summary, level 1 real-time monitoring features high sampling rates and very short reaction times to errors. It addresses the demand for faster irradiation systems in particle therapy and imposes minimal constraints on the beam delivery system. The definition of tolerances is based on only four values: a margin for the local beam-on time (δt), a margin for the transverse beam position ($\delta T/\delta U$), a margin for the beam current (δI), and a margin for the locally deposited dose (δD). These margins can be adapted according to changing circumstances (e.g. machine parameters or national legislations). As such, level 1 is a valid monitoring approach for most particle therapy centers around the world. The follow-up publication (see chapter 5) derives values for the four margins from first principles considering Gantry 2 machine parameters. Hence, it assures effective and clinically acceptable level 1 real-time monitoring.

7.1.3 The compliance with safety regulations

Safety level 1 will be an effective measure against delivery inaccuracies or errors only when provided clinically adequate margins. In other words, the comparator unit of the FPGA must check incoming values against clinically meaningful tolerances. If the margins are too narrow, interlocks will be triggered too early picking up insignificant dosimetric fluctuations; if the margins are too wide, interlocks will be triggered too late allowing for potentially harmful errors in the irradiation. Seeking an appropriate balance, chapter 5 provides a full derivation of all four tolerance values from first principles following a rigorous worst-case error estimation. Although the assumed machine parameters are specific to the Gantry 2 scanning system, the derivation itself should be general enough to apply to other centers as well.

The starting point is a formal definition of an erroneous delivery. The ICRU report 78 published by the International Commission on Radiation Units and Measurements (2007) indirectly mentions that dose distributions must be delivered with sufficient uniformity. Hot and cold spots should be restricted to $\pm 2.5\%$. The error definition in chapter 5 is slightly more strict:

“We consider an irradiation erroneous if the homogeneity (or uniformity) across the target is significantly impaired. We set the threshold at absolute deviations of $\pm 2\%$ or ± 36 mGy.”

– Klimpki et al. (2017a)

The latter value is based on the assumption that errors in beam delivery occur rarely (much less than once per treatment) and at random locations. Assuming an average fraction dose of 2 Gy (RBE) or 1.818 Gy physical, deviations of $\pm 2\%$ correspond to absolute differences of ± 36 mGy. As indicated by the French Nuclear Safety Authority (2010) in their definition of radiation incidents, localized over- or underdosages of this magnitude may be physically measurable, but they are not expected to have any consequence on the clinical outcome of the treatment. Hence, by restricting all excess or missing doses to ± 36 mGy through effective level 1 beam monitoring, we can assure safe irradiations in line scanning mode. It is worth mentioning that the International Electrotechnical Commission (2014) allows for even higher differences between intended and actually delivered dose distributions in their international standard (IEC 60601-2-64). They state that the magnitude of hot and cold spots can be as high as 10% or 250 mGy, whichever is greater. Self evidently, these constraints are satisfied through the definition given above.

The derivation of the level 1 safety tolerances in chapter 5 is of theoretical nature. As mentioned in the introduction to this thesis, an irradiation free from any machine-related risks can never be provided. As such, the goal of the beam monitoring system is to reduce these risks to events with minimal impact on the outcome of the treatment. However, a smooth clinical workflow may require compromises on the tolerances. E.g. it is irrational to impose a beam position tolerance that is much smaller than the spatial resolution of the position-sensitive detector. It may even be impracticable to demand tolerances that trigger interlocks very frequently and, hence, prolong the irradiation of each and every patient. Under these circumstances, softening theoretically derived margins may be eligible by choosing them as low as reasonably achievable (ALARA principle). Chapter 5 concludes that the transverse beam position should be within ± 1 mm. However, Smith et al. (2009) report on a margin of ± 1.8 mm used at the MD Anderson Cancer Center in Houston, Texas. Although not fulfilling the theoretical requirement and potentially compromising patient safety, a lower tolerance value may not be applicable at their center in the interest of a smooth clinical workflow.

Unfortunately, the amount of monitoring tolerances published in the literature is sparse. Each institution and commercial vendor weighs safety aspects differently resulting in a multitude of safety concepts, all of which somehow comply with international norms and regulations. As such, chapter 5 could help standardizing safety considerations and margin definitions without restricting the space for further technological developments.

7.1.4 The application of line scanning in the context of moving target treatments

The combination of chapters 3, 4 and 5 guarantees safe patient irradiation in line scanning mode on Gantry 2. These chapters enable clinical usage of the line scanning technique by minimizing the risk of harmful overexposure of healthy tissue or alarming underexposure of tumor tissue to radiation in case of technical failures. However, the clinical use case of line scanning and the associated performance gain remain to be demonstrated. This is the purpose of the final study included in this dissertation (see chapter 6). It examines line scanning (and two other irradiation techniques) in the context of moving target irradiations using the rescanning approach and investigates how effectively (or how well) and how efficiently (or how fast) interplay patterns can be mitigated.

The set of targets included in this study comprises three liver tumors prescribed to identical dose levels. The tumors vary in size and shape and show different motion (e.g. amplitude and period) and deformation characteristics. The uniqueness of this study is that for each target, three different treatment plans have been constructed: one dedicated to the line scanning technique and two dedicated to other commercially available forms of pencil beam scanning (referred to as spot and raster scanning). Moreover, the Gantry 2 scanning system could be configured such that it supports irradiation of all three plan types. This modification enabled a quantitative analysis of the effectiveness and efficiency of three different pencil beam scanning techniques in the context of rescanning moving targets under identical machine parameters (e.g. accelerator, beam current, beam size, dead times).

The 4D dose calculations and measurements show that rescanning mitigates interplay patterns effectively for small motion amplitudes (< 10 mm) independent of the beam scanning technique. This result is in agreement with previous findings reported in the literature (Schätti et al., 2013, 2014; Zhang et al., 2016). The key to effective mitigation is a high number of rescans. Delivering the field dose in many repetitions requires a flexible beam delivery system that is able to scale down the dose at every point in the plan. It could be shown that combined modulation of the transverse scan speed and beam current, as provided by the line scanning technique, provides an advantage in this regard. Concerning the efficiency of beam delivery under rescanning, continuous scanning techniques (e.g. raster or line scanning) are superior to discrete ones (e.g. spot scanning). Furthermore, irradiating the target with the highest beam current possible speeds up beam delivery. As such, scaling of the current at any point in the target according to the local dose deposition can be considered advantageous. In principle, any of the three scanning techniques could offer this functionality as it is coupled to the accelerator conditions rather than to the beam scanning system. In addition to these findings, chapter 6 reveals that volumetric rescanning is significantly more effective than layered rescanning, although being less efficient. This result confirms earlier works done by

Seco et al. (2009), Schätti et al. (2013), and Zhang et al. (2016). In summary, one can reach high numbers of rescans and irradiate fields of very low dose (~ 100 mGy) rapidly using the line scanning technique. Hence, it can be considered an effective and efficient delivery technique when rescanning moving targets.

7.2 Strengths and weaknesses of the underlying methods

The tools and methods used in this dissertation inevitably influence the results summarized in the previous section. Their choice will be motivated in the following by weighing their strengths against their weaknesses. Potential bias or restrictions are discussed critically whenever suspected.

7.2.1 The choice of beam monitors

The two-stage monitoring system was designed based on a detailed performance assessment of various diagnostic devices installed along the Gantry 2 beamline. Their response to the line scanning technique was investigated in order to determine, how the different detectors can contribute to risk minimization. The primary goal has always been to use and combine existing devices but replacements or additional installations have not been ruled out *per se*. However, relying on tested and commissioned detectors offers two main advantages: the clinical workflow in conventional irradiation mode can continue without interruptions and both irradiation modes will be fully compatible. As such, one can easily activate or deactivate the line scanning technique whenever desired without having the need for physical changes to the beamline.

The performance assessment revealed two deficiencies of the detectors in use: (1) The readout of the strip monitor is too slow to enable real-time monitoring of the transverse beam position. (2) The ionization chambers in the gantry nozzle are not particularly fast in collecting charges. Especially monitor 2 provides a significant delay of roughly 370 μ s. To cope with these circumstances, two alternative solutions have been developed: (1) Hall probes in the scanner magnets are used to monitor the transverse beam position indirectly. (2) Only monitor 1 is used to supervise the proton beam current in safety level 1. The signal from monitor 2 is integrated over time to monitor the number of delivered protons. Safety considerations showed that margins are less strict on the latter quantity somewhat mitigating the delay problem. Nonetheless, redundancy is preserved by checking the instantaneous and integrated beam current using two independent ionization chambers.

Choosing Hall probes as primary position monitors comes at the cost of losing direct information on the beam position. It is not necessarily guaranteed that an appropriate field strength will deflect the beam to the correct transverse position. Especially

entering the scanner magnets under angles or offsets has been of concern. To estimate the influence of these uncertainties, the beam transport through the gantry was studied in simulations based on the OPAL framework (Rizzoglio et al., 2017). In summary, such scenarios are largely suppressed by the transport settings of the beamline upstream of the gantry. They have been optimized to inject a beam with rotational symmetric and achromatic phase space into the gantry (Pedroni et al., 2011). A collimator at the coupling point additionally suppresses erroneous phase spaces. Moreover, settings of all magnets on (and off) the gantry are supervised: inaccuracies or failures cause interlocks. Last but not least, Gantry 2 is an upstream scanning system featuring parallelism of the beam in both scanning directions. As such, the scanner magnets are situated upstream of the final 90° bending magnet. Its particular design damps position offsets due to divergence-compensating optics (Gabard et al., 2010).

But besides all drawbacks and concerns, using Hall probes to indirectly monitor the transverse beam position also offers three considerable advantages: (1) Their signal-to-noise ratio (SNR) is extremely low (less than $10\ \mu\text{m}$ at iso-center) and independent of the proton beam current. Since line scanning permits frequent modulation of the beam current, a stable SNR on the monitored beam position is not trivial and certainly advantageous. (2) Hall probes could be equipped with real-time readout functionality and successfully integrated in safety level 1. High sampling rates guarantee short reaction times to errors in the beam position and grant high flexibility in beam delivery. (3) Ultimately, the position-sensitive strip monitor could be used for additional, redundant checks. In safety level 2, it validates the delivered dose profile of a line scan. As such, the strip monitor can almost be regarded as a quality assurance measure evaluating dose delivery online.

7.2.2 The look-up table approach for safety level 2

The prediction of dose profiles from nominal delivery parameters in safety level 2 is based on a look-up table approach. Systematic analysis of the strip monitor response showed that the recorded beam profile depends on five parameters: the gantry angle α , the beam energy E , the nozzle extension S , as well as the transverse T and U position. Seeking for a computationally efficient model, five-dimensional polynomials of the form $f(\alpha, E, S, T, U) = \mathcal{O}(\alpha^4, E^4, S^2, T^2, U^2)$ have been fitted to the acquired data set. However, the accuracy achieved was insufficient. Consequently, the look-up table and interpolation approach described in chapter 3 was developed. Because the computation time of a single profile prediction is substantial ($\sim 5\ \text{ms}$ on average), this task is executed when loading the plan prior to the treatment. Pre-calculated predictions are stored in the RAM and accessed during the comparison step of safety level 2.

For line scans of medium to high dose, the profile prediction matches measurements obtained with the strip monitor extremely well (see figure 3.6). However, line scans

that deposit very little dose will also induce very little signal in the strip monitor. In such cases, the profile comparison margins must be softened to prevent frequent interlocks. A second weakness of the profile prediction algorithm is its sensitivity to changes in the beam optics. The recorded look-up table is only valid as long as the beam shape is stable and reproducible across the five-dimensional parameter space. Significant variations may require a recalibration of the look-up table. Although the measurement is automated, it still requires hours of data acquisition.

7.2.3 The firmware limitations

All monitoring-related tasks run on a single Virtex-6 FPGA from Xilinx, Inc. As such, level 1 real-time monitoring is only one task among others executed within the FPGA. Consequently, the resources are limited and the computational tasks concerning level 1 monitoring needed to be simple (e.g. interpolation, integration, comparison). Thus, the more complex calculation of the tolerance bands around the nominal delivery tables has to be performed in software. As described in chapter 4, the control system downloads the calculation results into the RAM of the FPGA before the application of each line scan. Unfortunately, the calculation and download of the tolerance bands prolongs the dead time between two lines significantly. In discrete scanning mode, the average dead time between two dose spots amounts to 2.83 ms. In continuous line scanning mode, this dead time measures 7.90 ms on average. While other factors such as level 2 related monitoring tasks add to this number, the major contribution ($\sim 50\%$) originates from calculating and downloading tolerance tables leaving much room for further optimization in the interest of delivery performance.

A second limitation is the size of the RAM itself. Currently, the logging tables written to the machine log in case of an interlock can span 327.67 ms only. If the tolerance violation happens to occur afterwards, it will not be visible in the machine log impeding interlock analysis. The length of the logging tables can, in principle, be extended (ideally to 1 s) by accessing external RAM blocks. However, this enhancement requires substantial changes to the firmware architecture. Nonetheless, the implementation is encouraged before starting clinical treatments in line scanning mode.

7.2.4 The assumption of rare interlocks

Level 1 monitoring restricts hot and cold spots arising from erroneous beam delivery to ± 36 mGy when using the set of margins derived in chapter 5. This is a very conservative limit assuming that interlocks of that kind occur, on average, less than once over the entire course of the treatment. Even if every fraction experiences a level 1 interlock, hot and cold spots will average out in superposition as long as they are randomly distributed throughout the irradiated volume. However, if interlocks occur very frequently and at similar location, hot and cold spots could amplify

resulting in undesired and clinically unacceptable deviations from the planned dose distribution. Safety level 1 cannot prevent such a scenario. Thus, it is strongly recommended to analyze the source of the interlock carefully using the tools provided (e.g. machine log files) before resuming the treatment. The operating physicist could pay particular attention to the warning counters. During every line scan they count the number of incoming data samples that came close to violating their tolerance and triggering an interlock. E.g. line scans with high warning counters on the T position indicate a malfunction of the scanner magnet or Hall probe. Only solving this issue before resuming the treatment can guarantee patient safety. In summary, level 1 monitoring cannot warrant zero-risk irradiations and it is always possible to construct failure scenarios harmful to the patient. However, all of them presuppose very unreasonable and negligent behavior of the operators.

7.2.5 The treatment plan converter

The final study included in this dissertation (see chapter 6) demonstrates a potential use case of the line scanning technique. It compares the effectiveness and efficiency in mitigating interplay patterns through rescanning across different beam delivery techniques. For each of the three techniques, clinically acceptable and deliverable treatment plans were created. However, the treatment planning system (TPS) can optimize discrete spot scanning plans only. Since it lacks means to create plans for continuous scanning techniques, a converter (see section 2.2) has been developed and used to translate spot scanning plans to raster and line scanning plans of equal dosimetric quality. Indeed, static target coverage was very similar with residual dose differences of the order of $\pm 1\%$ for 95% of the target voxels. Although preserving dosimetric similarity, the plan converter may not necessarily ensure consistent performance conditions across the different scanning techniques. E.g. by translating plans of suboptimal starting conditions, raster and line scanning could have been restricted in their delivery performance. Thus, the efficiency (and potentially also the effectiveness) of raster and line scanning could have been underestimated in this study.

By selecting fairly homogeneous liver targets, this bias was suppressed as much as possible. Spots in the original treatment plan have been placed on mostly uninterrupted lines. The dose modulation from one spot to the next was moderate creating optimal performance prerequisites for raster and line scanning. Nonetheless, only a TPS that considers performance criteria in its optimization step would completely overcome this restriction. Implementations could be similar to direct optimization techniques in volumetric modulated arc therapy (Papp and Unkelbach, 2014; Unkelbach et al., 2015). Such a planning system would also open up the possibility to study the effectiveness and efficiency of treating targets with heterogeneous beam paths (e.g. lung tumors) using the line scanning technique. Results and conclusions may be different in such cases.

7.2.6 Resuming irradiations after level 1 interlocks

The previous sections discussed the weaknesses and deficiencies of this dissertation in great detail. Especially the choice of hardware and available FPGA resources has been reviewed critically. Nevertheless, and despite all limitations, an accurate and reliable beam monitoring system could be developed, implemented and tested. But at this point, one open question still remains: how to resume the treatment after an interlock triggered by safety level 1? This section will briefly introduce the resumption strategy and demonstrate successful implementation.

Safety level 1 can detect interlocks originating from four different sources: (1) instantaneous beam current, (2) integrated beam current, (3) transverse T position of the beam, and (4) transverse U position of the beam. The precise time of primary tolerance violation is stored in FPGA registers and queried by the control system. This point in time will be referred to as $t_{\text{ILK},1}$ in the following. Any level 1 interlock – erroneous beam current, transverse position or deposited dose – will trigger a beam off command. Consequently, these primary interlocks will cause a secondary interlock on the instantaneous beam current as the beam is being turned off. Its time of occurrence is also stored in machine log files and will be denoted as $t_{\text{ILK},2}$ in this section. This rule has two exceptions: (i) If a low beam current should be the primary cause of error, $t_{\text{ILK},1}$ and $t_{\text{ILK},2}$ will be identical. (ii) If the lower tolerance on the beam current should be zero, a secondary interlock may not be triggered. In this case, $t_{\text{ILK},2}$ will be set equal to $t_{\text{ILK},1}$. A typical example case could be a stagnating scanner magnet preventing the beam from moving along the T -direction. A primary interlock will be issued as soon as the T -position is outside tolerance to turn off the beam. Shortly after, the beam current measured by monitor 1 drops triggering a secondary interlock on this channel. Typically,

$$t_{\text{ILK},2} \cong t_{\text{ILK},1} + 0.30 \text{ ms.} \quad (7.1)$$

In order to avoid overdosing the patient, the resumption of the treatment will start from $t_{\text{ILK},2}$. As such, any additional dose deposited between the time of the primary interlock and complete beam suppression is taken into account. Because of delays in the control software, the precise time of resumption t_{res} had to be shifted by a small correction term Δt_{corr} determined empirically:

$$t_{\text{res}} = t_{\text{ILK},2} - \Delta t_{\text{corr}} = t_{\text{ILK},2} - 0.17 \text{ ms.} \quad (7.2)$$

With these values and considerations in place, the resumption itself is rather simple: The corrupt line will be irradiated again with a modified delivery table for the beam current. Between $t_0 = 0$ ms and t_{res} , the current is set to zero. Afterwards, it follows its nominal trajectory without further modifications.

Figure 7.1 demonstrates successful implementation of treatment resumption from level 1 interlocks. The left plot (a) shows a line profile recorded with the CCD

camera system described in section 2.3 that could be delivered interlock-free. The proton beam moves from $T = -5$ cm to $T = +5$ cm within 14 ms and induces a signal on the CCD sensor of ~ 60 counts along the central profile. Plot (b) shows the same line scan interrupted by an external software trigger after ~ 6 ms. Consequently, the light output vanishes around $T = 0$ cm. Plot (c) displays the interrupted line resumed from t_{res} . When evaluating the difference between plot (a) and plots (b)+(c), dosimetric equivalence can be observed in plot (d) validating the resumption strategy.

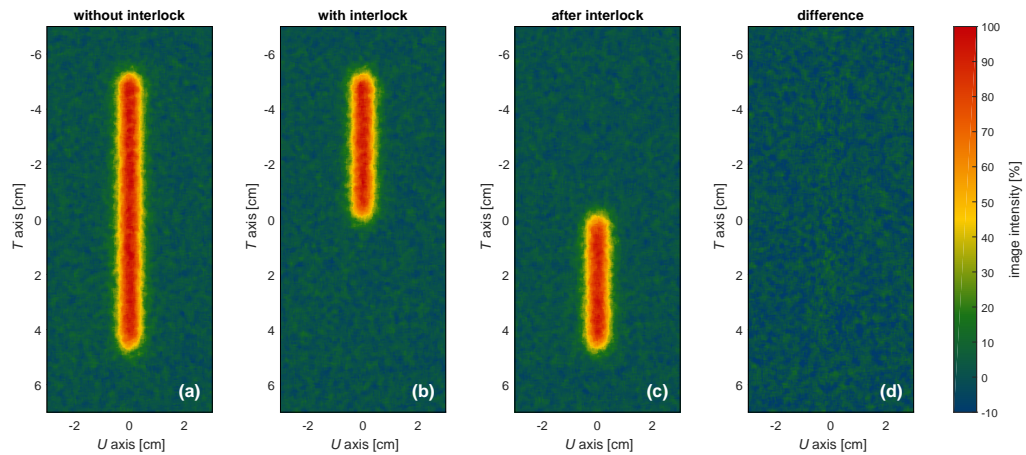


Figure 7.1: Dose profiles of single line scans recorded with the CCD camera system placed at iso-center. The interlock-free irradiation (a) shows a straight line scanned from $T = -5$ cm to $T = +5$ cm within 14 ms. Partial irradiations before and after an interlock are shown in plots (b) and (c), respectively. The difference between plot (a) and plots (b)+(c) is virtually zero demonstrating efficacy of the resumption strategy.

7.3 Future perspectives of line scanning

This final part of chapter 7 provides an outlook on the future perspectives of proton therapy and the line scanning technique. Subsection 7.3.1 discusses four remaining steps to be taken before using line scanning clinically for patient treatments. Subsection 7.3.2 highlights potential indications and tumor sites that could benefit most from fast irradiations. It also lists developments beyond the line scanning technique that could further improve the performance and quality of pencil beam scanning.

7.3.1 Open issues before clinical operation

This dissertation provides the technical basis for continuous pencil beam scanning on Gantry 2. It demonstrates successful implementation of an effective beam monitoring system for line scanning and emphasizes the clinical potential of this irradiation technique. However, four open issues remain that currently prohibit patient treatments in line scanning mode. They are discussed in the following.

Beam current regulation

One of the key characteristics of line scanning is its ability to modulate the beam current continuously while steering the beam along straight lines. In the interest of precise and accurate dose delivery, any modulation of the beam current must satisfy the following three constraints: (1) The absolute difference between nominal and actual beam current must stay within ± 35 monitor units (or ± 40 pA for a 150 MeV beam) at all times. Deviations of this magnitude may induce warnings during the irradiation, but they are far away from triggering a level 1 interlock (margin of ± 50 monitor units). (2) The beam current must stabilize within 750 μ s measured from the start of a line scan. This value originates from a minimal line length of 1.5 cm scanned at maximum accessible speed (2 cm/ms). Shorter lines will have inferior performance and accuracy compared to discrete beam spots. (3) The integral difference between prescribed and delivered dose must be within $\pm 2\%$ for every line scan to guarantee sufficient accuracy (Schippers et al., 2010). To fulfill these requirements, a feedback control loop counteracts inaccuracies in the regulation of the beam current. Based on the beam current measured in monitor 1, the voltage on the vertical deflector plate inside the cyclotron is adjusted in real-time to increase or decrease the extracted current compensating for deviations. However, constraints are not fully satisfied, yet: the power supply of the vertical deflector currently suffers from irreproducible regulation deficiencies hampering accurate beam current control. These effects are most pronounced when ramping the current quickly (both up and down) yielding undesired over- or undershoots, which, in most cases, trigger a level 1 interlock. One possible solution, apart from replacing the power supply entirely, could be a more sophisticated feedback controller. Its development is work in progress and tests will show if it enables beam current modulation according to specification.

Treatment planning system

As mentioned in section 7.2 above, irradiations in line scanning mode are not yet supported by the treatment planning system. To incorporate accurate dose calculation of scanned line segments, one needs to modify the transverse beam shape in T -direction. Discrete beam spots are modeled through a two-dimensional Gaussian distribution peaked around (μ_T, μ_U) :

$$d_{\text{spot}}(T, U) = N_p \eta_{\text{spot},T}(T) \eta_{\text{spot},U}(U), \quad (7.3)$$

with

$$\eta_{\text{spot},T}(T) = \frac{1}{\sigma_T \sqrt{2\pi}} \exp \left[-\frac{1}{2} \left(\frac{T - \mu_T}{\sigma_T} \right)^2 \right] \quad (7.4)$$

and

$$\eta_{\text{spot},U}(U) = \frac{1}{\sigma_U \sqrt{2\pi}} \exp \left[-\frac{1}{2} \left(\frac{U - \mu_U}{\sigma_U} \right)^2 \right]. \quad (7.5)$$

N_p denotes the total number of delivered protons and $\sigma_{T/U}$ represents the width of the pencil beam in T/U -direction. To describe line segments mathematically, $\eta_{\text{spot},T}(T)$ has to be convolved with a rectangular kernel function characterizing the movement of the beam in T -direction. Resulting line segments take the form

$$d_{\text{line}}(T, U) = N_p \eta_{\text{line},T}(T) \eta_{\text{spot},U}(U), \quad (7.6)$$

with

$$\eta_{\text{line},T}(T) = \frac{1}{2\Delta T} \left(\operatorname{erf} \left[\frac{T - (\mu_T - \Delta T/2)}{\sigma_T \sqrt{2}} \right] - \operatorname{erf} \left[\frac{T - (\mu_T + \Delta T/2)}{\sigma_T \sqrt{2}} \right] \right). \quad (7.7)$$

ΔT denotes the scan distance of the line segment. In addition to the dose calculation engine, line scanning should also be incorporated in the optimization algorithm. By penalizing gaps in the scan path (segments with $N_p = 0$), one could force continuous line scans of moderate modulation. Furthermore, the scan distances of individual segments should be variable, not bound to any grid constraints, to allow for maximum flexibility. Last but not least, line scanning must also be incorporated in the retrospective dose calculation based on machine log files (Meier et al., 2015), which proved to be a valuable tool for identifying differences between planned and delivered dose distribution (Scandurra et al., 2016; Belosi et al., 2017).

Quality assurance measures

Actis et al. (2017) recently reported on the daily quality assurance (QA) routine executed on Gantry 2 every morning prior to patient irradiations. It assesses the machine performance and verifies beam characteristics to demonstrate functionality of the beam delivery and monitoring units within specified tolerances. *Inter alia*, the routine checks the range and divergence of the proton beam for various energies, the accuracy of the pencil beam position in the transverse plane, as well as the dose delivered to a three-dimensional box target. To incorporate line scanning into the clinical workflow, dedicated QA measures would have to be added to the routine. It would certainly be worth validating functionality of the T and U -scanner Hall probes. Furthermore, the responsiveness of all level 1 interlock lines should be tested to guarantee effective real-time monitoring during treatment. Concerning beam delivery, the modulation of the beam current and scan speed should be checked in separate tests. Additionally, their combined effect should be analyzed through level 2 profile comparisons. Finally, irradiating a box field in line scanning mode could confirm accurate dose delivery.

In addition to these daily checks, line scanning also necessitates dedicated monthly QA measures. It is advised to recalibrate the Hall probes frequently to guarantee effective level 1 monitoring of the transverse beam position. Previously observed drifts, especially on the T Hall probe, could impair the accuracy of safety level 1

significantly. As such, calibrations should be repeated on a monthly basis. Other models characterizing the system (e.g. beam shape look-up table used for level 2 profile predictions) could be validated yearly and reacquired if necessary.

Legal authorization

The final hurdle for treatments in line scanning mode is the official agreement from the federal health authority. It can only be issued when achieving all of the following three milestones: (1) The Gantry 2 safety report needs to be revised. In its current form, it foresees treatments in spot scanning mode only. As such, the risk and fault tree analysis has to be expanded according to the considerations made in chapter 5. The safety measures introduced in chapter 3 should also be incorporated into this document demonstrating effective and redundant prevention of errors. (2) A list of daily, monthly, and yearly QA tasks dedicated to line scanning must be created and added to the existing manual. Furthermore, their effectiveness needs to be demonstrated and thoroughly documented. (3) Ultimately, end-to-end tests (treatment plan → patient-specific verification → dummy irradiation → log file analysis) must prove successful integration of the line scanning technique into the clinical workflow.

7.3.2 The evolution of proton therapy: a methodological comparison

Proton therapy is at the frontier of moving target treatments. Currently restricted to irradiations of predominantly static tumors, researchers seek for viable solutions that overcome this barrier making proton therapy accessible to a much wider range of indications. Continuous beam scanning could be an important milestone in this evolution. Compared to discrete pencil beam scanning, it offers superior performance characteristics such as reduced treatment time and enhanced flexibility in beam delivery. Chapter 6 shows that especially large tumors ($\gtrsim 250 \text{ cm}^3$) profit from these improvements. As such, craniospinal irradiations or elongated head and neck tumors may represent suitable indications. But most importantly, continuous scanning enables efficient treatment of moving targets using rescanning or other motion mitigation techniques (e.g. beam gating or breath-hold). In this context, abdominal cancers and large lung lesions represent tumor sites for which proton therapy may become practicable soon.

A comparison with the evolution of conventional radiation therapy, for which moving target treatments are standard clinical practice (see section 1.4), emphasizes the importance of continuous and highly dynamic irradiations. The transition from static *step-and-shoot* treatments to dynamic *sliding window* irradiations lead to the development of modern state-of-the-art delivery system offering advantages in both performance and plan quality. Nowadays, these systems enable effective and efficient

treatments of moving targets. The following enumeration briefly summarizes the main milestones in this development:

- ① *Passive conformation:* In the 1970s, revolutions in imaging and computational performance paved the way for significant improvements in radiation therapy. It was possible to conform the dose distribution more accurately to the shape of the tumor using patient-specific collimators. In early (3D) conformal radiation therapy, one collimator was manufactured for each beam angle allowing for dose escalation in the target and dose reduction to normal tissues (Vijayakumar and Chen, 1995). This approach provided good conformation and homogeneity but turned out to be time-consuming and expensive. Moreover, it restricted the number of beam angles or fields due to the inefficient workflow.
- ② *Active conformation:* Multi-leaf collimators (MLCs) helped to overcome these restrictions. They provide flexible, yet equally precise, fluence shaping and eliminate the need for individually manufactured collimators (LoSasso et al., 1993). Combined with inverse planning and optimization tools (Webb, 1989), MLCs maximized workflow efficiency in 3D conformal radiation therapy.
- ③ *Intensity modulation:* Further advances in treatment planning opened up the possibility for intensity-modulated radiation therapy (IMRT). To improve dose conformation to the target, static segments – each homogeneous in fluence – were combined to build up fields with inhomogeneous fluence distributions, whose superposition will ensure optimal target coverage and healthy tissue sparing (Bortfeld et al., 1994). Prior to the irradiation of each field segment, collimator leaves move into position. The intensity delivered to the field segment increases linearly with the respective beam-on time. Due to alternating beam-on and beam-off phases, this form of irradiation is often referred to as *step-and-shoot* IMRT. Fraass et al. (1999) called it a practical and simple evolution of 3D conformal radiation therapy.
- ④ *Continuous irradiation:* However, many small field segments prolong the overall irradiation time. Hence, Brahme (1988) and Convery and Rosenbloom (1992) proposed an alternative to static IMRT: the so-called *sliding window* approach. The idea is to move open MLC windows across the target during beam-on while changing leaf positions continuously to modulate the field intensity. The scan speed of individual leaves is adapted according to the prescribed fluence distribution. Seco et al. (2001) and Nicolini et al. (2005) conclude superior target coverage and performance. Simultaneous modulation of the output fluence rate offers additional flexibility in the delivery.
- ⑤ *Performance optimization:* Current state-of-the-art treatments use an irradiation technique commonly referred to as volumetric modulated arc therapy (VMAT) (Yu, 1995). It is yet another step in the evolution of radiation therapy. VMAT combines intensity modulation through sliding MLC windows and

continuous rotation of the gantry around the patient. As such, it replaces the concept of discrete fields with continuous arcs. In VMAT, intensity modulation can be achieved by adapting the position and velocity of the individual leaves, by changing the rotation speed of the gantry, and by controlling the dose rate. This three-fold degeneracy requires advanced planning tools that permit optimizing plan quality and irradiation performance simultaneously (Unkelbach et al., 2015).

Interestingly, proton therapy follows a very similar evolution with striking analogies:

- ① *Passive conformation:* Similar to conformal radiation therapy, the passive scattering technique uses patient-specific collimators and compensators to conform the proton field to the target (Koehler et al., 1977). Despite being comparably cost effective and robust (e.g. to organ motion), recent developments indicate a paradigm shift away from passive scattering (Meer and Psoroulas, 2015).
- ② *Active conformation:* Pencil beam scanning (PBS) (Renner et al., 1989) is now the method of choice for nearly half of the proton therapy centers around the world. Just like MLCs, pencil beam scanning eliminates the need for patient-specific hardware in the beamline and, thus, reduces the neutron background dose significantly (Hälg et al., 2014). Most technical implementations of PBS constrain the proton beam position to a rectilinear grid (Haberer et al., 1993; Pedroni et al., 1995).
- ③ *Intensity modulation:* Nevertheless, PBS represents a more flexible irradiation technique than passive scattering. For instance, it opened up the possibility for in-field intensity modulation. In analogy to IMRT, intensity-modulated proton therapy can reduce dose to neighboring organs at risk by optimizing the dose distributions of all fields simultaneously (Lomax, 1999). The resulting fields exhibit inhomogeneous dose distributions that can irradiated precisely using PBS only.
- ④ *Continuous irradiation:* To overcome the grid constraint in PBS, continuous beam scanning has been proposed and implemented (Pedroni et al., 2011; Inoue, 2014) in analogy to the *sliding window* approach. It has the potential to increase irradiation performance (Schätti et al., 2014) and dose conformity, when carried out along arbitrarily shaped tumor contours (Meier et al., 2017). The simultaneous modulation of the beam current at any point in the target offers additional gain in performance.
- ⑤ *Performance optimization:* Higher dose rates and further degrees of freedom in beam delivery would help maximizing machine performance. Continuous modulation of the beam energy and, potentially, simultaneous irradiation and rotation of the gantry would open up the possibility to optimize treatment

plans according to dose and performance constraints. VMAT-like irradiations under rotation would additionally smear out skin and entrance doses. In proton therapy, this step remains to be taken.

Slowly advancing to stage four, proton therapy lags behind conventional radiation therapy in many regards. Hence, it is not surprising that organ motion still represents a major obstacle. Self-evidently, the pronounced sensitivity of scanned proton beams to anatomical variations aggravates this issue. Further technological advances in the direction of rapid and fully continuous irradiations may still be required to enable effective and efficient moving target treatments. Continuous beam scanning along tumor contours, continuous modulation of the beam energy, and simultaneous rotation of the gantry may represent suggestions worth investigating. They all have in common that they require continuous monitoring systems similar to the one developed in this dissertation to guarantee safe irradiations. At the same time, and this could be one of the most challenging aspects, proton therapy machines must become smaller and cheaper to make this technique affordable for ordinary hospitals and not just a few specialized centers around the world (Bortfeld and Loeffler, 2017).

8

Concluding remarks

The beam monitoring system presented in this dissertation ensures safe patient treatments using continuous pencil beam scanning in proton therapy. The risks associated with this advanced form of irradiation have been analyzed in order to derive an adequate set of safety measures. Their formulation led to the conceptual design of the monitoring system (see \mathcal{Q}_1 and chapter 3). After implementing and testing required software and firmware enhancements (see \mathcal{Q}_2 and chapter 4), the efficacy of the monitoring system was guaranteed through the derivation of clinically acceptable safety tolerances (see \mathcal{Q}_3 and chapter 5). This technological foundation enables continuous patient irradiations that comply with international norms and guidelines. Moving target treatments are expected to benefit most from continuous pencil beam scanning, since it offers high flexibility in dose modulation while keeping irradiation times short. For instance, line scanning improves both efficiency and effectiveness of rescanning when compared to other discrete beam scanning techniques (see \mathcal{Q}_4 and chapter 6). As such, it represents a promising technology to tackle the difficulties associated with moving target treatments in scanned proton therapy.

The driving principle of this thesis has been to balance the risks and benefits of continuous irradiations in proton therapy. The monitoring system needs to be responsive and reliable, yet minimally invasive to the beam delivery itself to allow for dynamic modulation of the scanning parameters (e.g. speed and current). Level 1 real-time monitoring satisfies these requirements. The beam current, the number of deposited protons, and the transverse beam position are supervised in parallel to the irradiation on dedicated software and hardware units. Every 10 μs , sampled signals are compared to expected values and an interlock will be triggered if one of these

comparisons fails. As such, level 1 real-time monitoring ensures patient safety in the case of machine-related errors while imposing minimal constraints on beam delivery. The scan speed and beam current can change frequently and rapidly at any point in the irradiation as long as the actuators follow their setpoints within clinically acceptable tolerances. Level 2 online monitoring represents an additional, partly redundant safety stage. Between the application of two continuous scans, integral dose profiles in both transverse directions are compared to predictions calculated from the nominal delivery tables used to steer the actuators. As such, safety level 2 is able to identify small inaccuracies in beam delivery potentially undetected by level 1.

The implementation of level 1 real-time monitoring represents another compromise between risk and benefit. The choice of detectors was restricted to devices already installed and commissioned. While this approach avoids uncertainties originating from supplementary hardware, it may come at the cost of suboptimal performance. The same argument holds for the software and hardware topology, which has been enhanced with functionality enabling real-time monitoring. However, the entire architecture and signal flow remained unchanged. Nonetheless, level 1 real-time monitoring could be successfully implemented and tested. It triggers interlocks quickly and reliably for all scanning parameters under supervision. The proton beam is completely suppressed after 300 μs in case of a detected tolerance violation. This value is well within the clinical safety requirements for continuous beam scanning on Gantry 2. For every interlock, the precise time of occurrence is documented in machine log files. When resuming the treatment, actuators of the beamline are steered to conditions that correspond to exactly that point in time and the irradiation can be resumed without inducing additional dosimetric fluctuations.

The clinical benefits associated with continuous pencil beam scanning mainly concern machine performance. Irradiation times can be decreased by using the beam more efficiently. On Gantry 2, line scanning is significantly faster than spot scanning while delivering dose distributions of similar quality. The gain in performance can be crucial especially in the context of moving target irradiations, where mitigation techniques such as rescanning, gating or breath-hold require fast beam delivery. In case of rescanning, continuous irradiations offer a second advantage: because of pronounced flexibility in dose modulation, they can achieve higher rescanning capability, which is beneficial for the effectiveness of motion mitigation.

Most proton therapy systems installed today are designed for a lifecycle of several decades. However, the technology behind them and the clinical requirements evolve much faster. This dissertation demonstrates a successful system upgrade from discrete, *step-and-shoot* treatments to continuously scanned irradiations. Since the underlying actuators and diagnostic devices are identical, the upgrade could be carried out in parallel to daily clinical operation. Hence, this work could be of interest to any vendor or center around the world trying to keep up with changing demands in order to constantly offer high-quality, state-of-the-art proton therapy.

APPENDIX



List of publications

During my time at the Center for Proton Therapy of the Paul Scherrer Institute I have written a total of six publications; four of those as first-author and two of those as co-author. While some of them are already published, others may still be under review. A complete overview is provided in the following.

First authorship

- Klimpki *et al.* A beam monitoring and validation system for continuous line scanning in proton therapy. *Physics in Medicine and Biology*, **62**(15):6126–6143, 2017.
- Klimpki *et al.* Real-time beam monitoring in scanned proton therapy. *Nuclear Instruments and Methods in Physics Research A*, **891**:62–67, 2018.
- Klimpki *et al.* A real-time beam monitoring system for highly dynamic irradiations in scanned proton therapy: derivation of safety tolerances. In *Proceedings of ICALEPCS 2017, Barcelona, Spain*, pages 1224–1228, 2017.
- Klimpki *et al.* The impact of pencil beam scanning techniques on the effectiveness and efficiency of rescanning moving targets. *Physics in Medicine and Biology*, submitted on December 22 (2017).

Co-authorship

- Psoroulas *et al.* Challenges in fast beam current control inside the cyclotron for fast beam delivery in proton therapy. In *Proceedings of CYCLOTRONS 2016, Zurich, Switzerland*, pages 1–4, 2016.
- Krieger *et al.* Experimental validation of a deforming grid 4D dose calculation for PBS proton therapy. *Physics in Medicine and Biology*, **63**(5):055005-1–11, 2018.

B

List of abbreviations

ADC	analog-to-digital converter
ALARA	as low as reasonably achievable
CCD	charge-coupled device
CNAO	Centro Nazionale di Adroterapia Oncologica
COG	center of gravity
CPT	Center for Proton Therapy
CT	computed tomography
CTV	clinical target volume
FPGA	field-programmable gate array
gITV	geometrical internal target volume
GSI	Gesellschaft für Schwerionenforschung
HIT	Heidelberger Ionenstrahl-Therapiezentrum
IBA	Ion Beam Applications
ICRP	International Commission on Radiological Protection
ICRU	International Commission on Radiation Units and Measurements
IEC	International Electrotechnical Commission
ILK	interlock
IMRT	intensity-modulated radiation therapy
LET	linear energy transfer
MLC	multi-leaf collimator
MRI	magnetic resonance imaging
MU	monitor unit
nD	n -dimensional

B List of abbreviations

NIRS	National Institute for Radiological Sciences
OPAL	Object Oriented Parallel Accelerator Library
PBS	pencil beam scanning
PMMA	poly(methyl methacrylate)
PROSCAN	proton scanning
PSI	Paul Scherrer Institute
PTCOG	Particle Therapy Co-Operative Group
PTW	Physikalisch-Technische Werkstätten
QA	quality assurance
RAM	random-access memory
RBE	relative biological effectiveness
RMS	root mean square
SCS	Supercomputing Systems
SENIS	Sensors, Instruments and Services
SNR	signal-to-noise ratio
SOBP	spread-out Bragg peak
TDS	therapy delivery system
TERA	TERA Fondazione per Adroterapia Oncologica
TPS	treatment planning system
TVS	therapy verification system
VMAT	volumetric modulated arc therapy

C

List of figures

1.1	Conventional radiotherapy vs. proton beam therapy	3
1.2	Interplay effect for a target in the liver	5
1.3	Rescanning capability for a target in the liver	8
2.1	Schematic of the Gantry 2 beamline	16
2.2	Schematic comparison of pencil beam scanning techniques	21
2.3	Fluence matching during treatment plan conversion	26
2.4	Geometric distortions of the CCD imaging system	28
2.5	Intensity distortions of the CCD imaging system	29
2.6	Quenching model of the CCD imaging system	30
2.7	Setup for experiments on Gantry 2	31
3.1	Schematic and dosimetric comparison of discrete spot and continuous line scanning	37
3.2	Flowcharts of the line scanning monitoring and validation system	40
3.3	Location and exemplary response of the Gantry 2 strip monitor .	41
3.4	Dependencies of the pencil beam width measured in the nozzle plane	44
3.5	Safety level 1 tolerance bands for the beam position and beam current at iso-center	46
3.6	Comparison of measured and predicted line profiles in the nozzle plane	49
3.7	Simulation of delivery inaccuracies to test safety level 2	50
4.1	Schematic of the Gantry 2 beamline	59
4.2	Signal flow of the delivery and monitoring system	60

LIST OF FIGURES

4.3	Simplified sketch of the FPGA logic in the monitoring system . . .	63
4.4	Installation of the Gantry 2 test system	64
4.5	Logging functionality of the FPGA firmware	66
4.6	Interlock scenario for beam position	67
4.7	Interlock scenario for instantaneous beam current	68
4.8	Interlock scenario for integrated beam current	69
5.1	Energy deposition of a 150 MeV proton beam in water	78
5.2	Calculated vs. simulated on-axis Bragg curves	78
5.3	Calibration curve for the primary ionization chamber	79
5.4	Schematic of the upper beam current tolerance band	80
5.5	Example for an error in the transverse beam position	81
6.1	Scan patterns for spot, raster and line scanning	89
6.2	Static dose distributions of all three patients	91
6.3	Accuracy of the Gantry 2 timing model	95
6.4	Dosimetric accuracy of raster and line scanning irradiations	96
6.5	Comparison of measured and calculated interplay patterns for spot, raster and line scanning	97
6.6	Target inhomogeneity vs. effective number of rescans	98
6.7	Target inhomogeneities of layered vs. volumetric rescanning	98
6.8	Effective number of rescans vs. predicted irradiation time	99
6.9	Experimental validation of effectiveness and efficiency of rescanning	100
7.1	Resuming a line scan from a level 1 interlock	116

D

List of tables

2.1	Specifications of the Gantry 2 scanner magnets	18
2.2	Generalized line scanning delivery table	22
3.1	Safety level 2 metrics of comparison	48
4.1	Delivery table for the proton beam current I and the corresponding upper and lower tolerances	62
6.1	Target sizes (gITV) considered for treatment planning	90
6.2	Specifications of the Gantry 2 beam delivery system	93

Bibliography

- H. Abbas, B. Chang, and Z. Chen. Motion management in gastrointestinal cancers. *Journal of Gastrointestinal Oncology*, 5(3):223–235, 2014. ISSN 2219-679X. DOI 10.3978/j.issn.2078-6891.2014.028. (cited on page 6)
- O. Actis, D. Meer, and S. König. Precise on-line position measurement for particle therapy. *Journal of Instrumentation*, 9(12):C12037, 2014. DOI 10.1088/1748-0221/9/12/C12037. (cited on pages 20 and 40)
- O. Actis, D. Meer, S. König, D. Weber, and A. Mayor. A comprehensive and efficient daily quality assurance for PBS proton therapy. *Physics in Medicine and Biology*, 62(5):1661–1675, 2017. DOI 10.1088/1361-6560/aa5131. (cited on page 118)
- E. Badura, H. Brand, H. Essel, T. Haberer, H. Hardel, J. Hoffmann, N. Kurz, P. Liebold, W. Ott, K. Poppensieker, and M. Richter. Control system for cancer therapy with a heavy ion beam at GSI. *IEEE Transactions on Nuclear Science*, 47:170–173, 2000. DOI 10.1109/RTCON.1999.842596. (cited on pages 51, 57 and 106)
- M. Belosi, R. van der Meer, P. Garcia de Acilu Laa, A. Bolsi, D. Weber, and A. Lomax. Treatment log files as a tool to identify treatment plan sensitivity to inaccuracies in scanned proton beam delivery. *Radiotherapy and Oncology*, 125(3):514–519, 2017. ISSN 0167-8140. DOI <https://doi.org/10.1016/j.radonc.2017.09.037>. (cited on page 118)
- K. Bernatowicz, A. Lomax, and A. Knopf. Comparative study of layered and volumetric rescanning for different scanning speeds of proton beam in liver patients. *Physics in Medicine and Biology*, 58(22):7905–7920, 2013. DOI 10.1088/0031-9155/58/22/7905. (cited on pages 8, 9, 88, 101 and 102)
- K. Bernatowicz, Y. Zhang, R. Perrin, D. Weber, and A. Lomax. Advanced treatment planning using direct 4D optimisation for pencil-beam scanned particle therapy. *Physics in Medicine and Biology*, 62(16):6595–6609, 2017. DOI 10.1088/1361-6560/aa7ab8. (cited on page 6)

Bibliography

- C. Bert and M. Durante. Motion in radiotherapy: Particle therapy. *Physics in Medicine and Biology*, 56(16):R113–R144, 2011. DOI 10.1088/0031-9155/56/16/R01. (cited on pages 5, 35, 87 and 91)
- C. Bert, S. Grözinger, and E. Rietzel. Quantification of interplay effects of scanned particle beams and moving targets. *Physics in Medicine and Biology*, 53(9):2253–2265, 2008. DOI 10.1088/0031-9155/53/9/003. (cited on pages 5, 9, 35 and 87)
- J. Birks. Scintillations from organic crystals: Specific fluorescence and relative response to different radiations. *Proceedings of the Physical Society. Section A*, 64(10):874–877, 1951. DOI 10.1088/0370-1298/64/10/303. (cited on page 29)
- H.-J. Borchert, M. Mayr, R. Schneider, M. Arnold, D. Geismar, M. Wilms, L. Wissner, and M. Herbst. Proton therapy with spot scanning: The Rinecker Proton Therapy Center in Munich. Part 2: Technical & physical aspects. *Nowotwory. Journal of Oncology*, 58(2):116–124, 2008. URL <http://www.nowotwory.edu.pl/archives.php?rok=2008&zeszyt=2>. (cited on pages 51, 57 and 106)
- T. Bortfeld and J. Loeffler. Three ways to make proton therapy affordable. *Nature News*, 549(7673):451–453, 2017. ISSN 0028-0836. DOI 10.1038/549451a. (cited on page 122)
- T. Bortfeld, A. Boyer, W. Schlegel, D. Kahler, and T. Waldron. Realization and verification of three-dimensional conformal radiotherapy with modulated fields. *International Journal of Radiation Oncology*Biophysics*Physics*, 30(4):899–908, 1994. ISSN 0360-3016. DOI 10.1016/0360-3016(94)90366-2. (cited on page 120)
- T. Bortfeld, S. Jiang, and E. Rietzel. Effects of motion on the total dose distribution. *Seminars in Radiation Oncology*, 14(1):41–51, 2004. ISSN 1053-4296. DOI 10.1053/j.semradonc.2003.10.011. (cited on page 5)
- D. Boye, T. Lomax, and A. Knopf. Mapping motion from 4D-MRI to 3D-CT for use in 4D dose calculations: A technical feasibility study. *Medical Physics*, 40(6):061702–1–11, 2013. ISSN 2473-4209. DOI 10.1118/1.4801914. (cited on pages 89 and 92)
- W. Bragg and R. Kleeman. XXXIX. on the α particles of radium, and their loss of range in passing through various atoms and molecules. *The London, Edinburgh, and Dublin Philosophical Magazine and Journal of Science*, 10(57):318–340, 1905. DOI 10.1080/14786440509463378. (cited on page 3)
- A. Brahme. Optimization of stationary and moving beam radiation therapy techniques. *Radiotherapy and Oncology*, 12(2):129–140, 1988. ISSN 0167-8140. DOI 10.1016/0167-8140(88)90167-3. (cited on pages 35 and 120)

- J. Chang, X. Zhang, X. Wang, Y. Kang, B. Riley, S. Bilton, R. Mohan, R. Komaki, and J. Cox. Significant reduction of normal tissue dose by proton radiotherapy compared with three-dimensional conformal or intensity-modulated radiation therapy in Stage I or Stage III non-small-cell lung cancer. *International Journal of Radiation Oncology*Biophysics*, 65(4):1087–1096, 2006. ISSN 0360-3016. DOI 10.1016/j.ijrobp.2006.01.052. (cited on page 4)
- C. Chung, T. Yock, K. Nelson, Y. Xu, N. Keating, and N. Tarbell. Incidence of second malignancies among patients treated with proton versus photon radiation. *International Journal of Radiation Oncology*Biophysics*, 87(1):46–52, 2013. ISSN 0360-3016. DOI 10.1016/j.ijrobp.2013.04.030. (cited on page 4)
- D. Convery and M. Rosenbloom. The generation of intensity-modulated fields for conformal radiotherapy by dynamic collimation. *Physics in Medicine and Biology*, 37(6):1359–1374, 1992. DOI 10.1088/0031-9155/37/6/012. (cited on pages 35 and 120)
- S. Dowdell, C. Grassberger, G. Sharp, and H. Paganetti. Interplay effects in proton scanning for lung: a 4D Monte Carlo study assessing the impact of tumor and beam delivery parameters. *Physics in Medicine and Biology*, 58(12):4137–4156, 2013. DOI 10.1088/0031-9155/58/12/4137. (cited on pages 9 and 88)
- J. Dueck, A.-C. Knopf, A. Lomax, F. Albertini, G. Persson, M. Josipovic, M. Aznar, D. Weber, and P. M. af Rosenschöld. Robustness of the voluntary breath-hold approach for the treatment of peripheral lung tumors using hypofractionated pencil beam scanning proton therapy. *International Journal of Radiation Oncology*Biophysics*, 95(1):534–541, 2016. ISSN 0360-3016. DOI 10.1016/j.ijrobp.2015.11.015. Particle Therapy Special Edition. (cited on page 7)
- M. Engelsman, M. Schwarz, and L. Dong. Physics controversies in proton therapy. *Seminars in Radiation Oncology*, 23(2):88–96, 2013. ISSN 1053-4296. DOI 10.1016/j.semradonc.2012.11.003. (cited on page 7)
- P. Evans. Anatomical imaging for radiotherapy. *Physics in Medicine and Biology*, 53(12):R151–R191, 2008. DOI 10.1088/0031-9155/53/12/R01. (cited on page 6)
- G. Fattori, G. Klimpki, S. Safai, D. Weber, A. Lomax, and S. Psoroulas. TH-CD-209-07: Preliminary experimental comparison of spot- and continuous line scanning with or without rescanning for gated proton therapy. *Medical Physics*, 43(6):3887–3887, 2016. DOI 10.1118/1.4958201. (cited on pages 2 and 10)
- G. Fattori, S. Safai, P. Carmona Fernández, M. Peroni, R. Perrin, D. Weber, and A. Lomax. Monitoring of breathing motion in image-guided PBS proton therapy: comparative analysis of optical and electromagnetic technologies. *Radiation Oncology*, 12(1):63–74, March 2017. ISSN 1748-717X. DOI 10.1186/s13014-017-0797-9. (cited on pages 32 and 96)

Bibliography

- J. Flanz. Particle beam scanning. In H. Paganetti, editor, *Proton Therapy Physics*, pages 157–190. CRC Press, 2011. ISBN 9781439836446. URL <http://www.crcpress.com/product/isbn/9781439836446>. (cited on pages 20 and 87)
- B. Fraass, M. Kessler, D. McShan, L. Marsh, B. Watson, W. Dusseau, A. Eisbruch, H. Sandler, and A. Lichter. Optimization and clinical use of multi-segment intensity-modulated radiation therapy for high-dose conformal therapy. *Seminars in Radiation Oncology*, 9(1):60–77, 1999. ISSN 1053-4296. DOI [https://doi.org/10.1016/S1053-4296\(99\)80055-1](https://doi.org/10.1016/S1053-4296(99)80055-1). (cited on page 120)
- French Nuclear Safety Authority. *Significant radiation protection events affecting patients in radiotherapy (criterion 2.1): Notification and ASN-SFRO scale rating*. French Nuclear Safety Authority, October 2010. URL <http://www.french-nuclear-safety.fr/References/ASN-Guides-non-binding/ASN-Guide-No.-16>. (cited on pages 38 and 109)
- T. Furukawa, T. Inaniwa, S. Sato, T. Tomitani, S. Minohara, K. Noda, and T. Kanai. Design study of a raster scanning system for moving target irradiation in heavy-ion radiotherapy. *Medical Physics*, 34(3):1085–1097, 2007. ISSN 2473-4209. DOI 10.1118/1.2558213. (cited on page 9)
- T. Furukawa, T. Inaniwa, S. Sato, T. Shirai, S. M. Mori, E. Takeshita, K. Mizushima, T. Himukai, and K. Noda. Moving target irradiation with fast rescanning and gating in particle therapy. *Medical Physics*, 37(9):4874–4879, 2010a. DOI 10.1118/1.3481512. (cited on pages 9 and 88)
- T. Furukawa, T. Inaniwa, S. Sato, T. Shirai, Y. Takei, E. Takeshita, K. Mizushima, Y. Iwata, T. Himukai, S. Mori, S. Fukuda, S. Minohara, E. Takada, T. Murakami, and K. Noda. Performance of the NIRS fast scanning system for heavy-ion radiotherapy. *Medical Physics*, 37(11):5672–5682, 2010b. DOI 10.1118/1.3501313. (cited on pages 51 and 87)
- A. Gabard, M. Negrazus, V. Vrankovic, and D. George. Magnetic measurements and commissioning of the fast ramped 90° bending magnet in the PROSCAN Gantry 2 project at PSI. *IEEE Transactions on Applied Superconductivity*, 20(3):794–797, 2010. ISSN 1051-8223. DOI 10.1109/TASC.2010.2040916. (cited on pages 18 and 112)
- S. Giordanengo, M. Donetti, M. Garella, F. Marchetto, G. Alampi, A. Ansarinejad, V. Monaco, M. Mucchi, I. Pecka, C. Peroni, R. Sacchi, M. Scalise, C. Tomba, and R. Cirio. Design and characterization of the beam monitor detectors of the Italian National Center of Oncological Hadrontherapy (CNAO). *Nuclear Instruments and Methods in Physics Research Section A: Accelerators, Spectrometers, Detectors and Associated Equipment*, 698:202–207, 2013. ISSN 0168-9002. DOI 10.1016/j.nima.2012.10.004. (cited on pages 51, 57, 70 and 106)

- S. Giordanengo, M. Garella, F. Marchetto, F. Bourhaleb, M. Ciocca, A. Mirandola, V. Monaco, M. Hosseini, C. Peroni, R. Sacchi, R. Cirio, and M. Donetti. The CNAO dose delivery system for modulated scanning ion beam radiotherapy. *Medical Physics*, 42(1):263–275, 2015. DOI 10.1118/1.4903276. (cited on page 87)
- C. Grassberger, S. Dowdell, A. Lomax, G. Sharp, J. Shackelford, N. Choi, H. Willers, and H. Paganetti. Motion interplay as a function of patient parameters and spot size in spot scanning proton therapy for lung cancer. *International Journal of Radiation Oncology*Biology*Physics*, 86(2):380–386, 2013. ISSN 0360-3016. DOI 10.1016/j.ijrobp.2013.01.024. (cited on pages 5, 9, 87 and 88)
- C. Grassberger, S. Dowdell, G. Sharp, and H. Paganetti. Motion mitigation for lung cancer patients treated with active scanning proton therapy. *Medical Physics*, 42(5):2462–2469, 2015. ISSN 2473-4209. DOI 10.1118/1.4916662. (cited on pages 9, 88, 101 and 102)
- S. Grözinger, C. Bert, T. Haberer, G. Kraft, and E. Rietzel. Motion compensation with a scanned ion beam: a technical feasibility study. *Radiation Oncology*, 3(1):34–41, 2008. ISSN 1748-717X. DOI 10.1186/1748-717X-3-34. (cited on page 8)
- T. Haberer, W. Becher, D. Schardt, and G. Kraft. Magnetic scanning system for heavy ion therapy. *Nuclear Instruments and Methods in Physics Research Section A: Accelerators, Spectrometers, Detectors and Associated Equipment*, 330(1–2):296–305, 1993. ISSN 0168-9002. DOI 10.1016/0168-9002(93)91335-K. (cited on pages 21, 57, 87 and 121)
- T. Haberer, J. Debus, H. Eickhoff, O. Jäkel, D. Schulz-Ertner, and U. Weber. The Heidelberg ion therapy center. *Radiotherapy and Oncology*, 73(Supplement 2):S186–S190, 2004. DOI 10.1016/S0167-8140(04)80046-X. Proceedings of the Heavy Charged Particles in Biology and Medicine. (cited on page 87)
- R. Hälgl, J. Besserer, M. Boschung, S. Mayer, A. Lomax, and U. Schneider. Measurements of the neutron dose equivalent for various radiation qualities, treatment machines and delivery techniques in radiation therapy. *Physics in Medicine and Biology*, 59(10):2457–2468, 2014. DOI 10.1088/0031-9155/59/10/2457. (cited on pages 4 and 121)
- J. Heinzerling, J. Anderson, L. Papiez, T. Boike, S. Chien, G. Zhang, R. Abdulrahman, and R. Timmerman. Four-dimensional computed tomography scan analysis of tumor and organ motion at varying levels of abdominal compression during stereotactic treatment of lung and liver. *International Journal of Radiation Oncology*Biology*Physics*, 70(5):1571–1578, 2008. ISSN 0360-3016. DOI 10.1016/j.ijrobp.2007.12.023. (cited on page 7)
- U. Hörrak, J. Salm, and H. Tammet. Statistical characterization of air ion mobility spectra at Tahkuse Observatory: Classification of air ions. *Journal of Geophys-*

Bibliography

- ical Research: Atmospheres*, 105(D7):9291–9302, 2000. ISSN 2156-2202. DOI 10.1029/1999JD901197. (cited on page 20)
- ICRP. 1990 Recommendations of the International Commission on Radiological Protection. *Annals of the ICRP*, 60(1–3), 1991. URL <http://www.icrp.org/publications.asp>. (cited on page 4)
- J. Inoue. Line scanning apparatus utilizing irradiation position and stationary time for scanning control. United States Patent no. 8890090, November 18 2014. URL <http://www.google.us/patents/US8890090>. SUMITOMO Heavy Industries, Ltd., Tokyo, Japan. (cited on pages 35, 51, 87 and 121)
- International Commission on Radiation Units and Measurements. Prescribing, Recording, and Reporting Proton-Beam Therapy – ICRU Report 78. *Journal of the ICRU*, 7(2):29–48, 2007. ISSN 1473-6691. DOI 10.1093/jicru/ndm026. (cited on pages 12, 35, 38, 57, 70, 75, 76, 94 and 108)
- International Electrotechnical Commission. Medical electrical equipment – part 2-64: Particular requirements for the basic safety and essential performance of light ion beam medical electrical equipment. IEC 60601-2-64:2014, International Electrotechnical Commission, Geneva, Switzerland, 2014. URL <https://webstore.iec.ch/publication/2680>. (cited on pages 2, 12, 35, 38, 57, 70, 75, 76 and 109)
- O. Jäkel, C. Jacob, D. Schardt, C. Karger, and G. Hartmann. Relation between carbon ion ranges and x-ray CT numbers. *Medical Physics*, 28(4):701–703, 2001. ISSN 2473-4209. DOI 10.1118/1.1357455. (cited on page 29)
- P. Keall, V. Kini, S. Vedam, and R. Mohan. Motion adaptive x-ray therapy: a feasibility study. *Physics in Medicine and Biology*, 46(1):1–10, 2001. DOI 10.1088/0031-9155/46/1/301. (cited on page 7)
- G. Klimpki, M. Eichin, C. Bula, U. Rechsteiner, S. Psoroulas, D. Weber, A. Lomax, and D. Meer. A real-time beam monitoring system for highly dynamic irradiations in scanned proton therapy: derivation of safety tolerances. In *Proceedings of ICALEPCS2017, Barcelona, Spain*, pages 1224–1228, 2017a. DOI 10.18429/JACoW-ICALEPCS2017-THCPA06. (cited on pages 61 and 109)
- G. Klimpki, S. Psoroulas, C. Bula, U. Rechsteiner, M. Eichin, D. Weber, A. Lomax, and D. Meer. A beam monitoring and validation system for continuous line scanning in proton therapy. *Physics in Medicine and Biology*, 62(15):6126–6143, 2017b. DOI 10.1088/1361-6560/aa772e. (cited on pages 58, 70 and 76)
- G. Klimpki, M. Eichin, C. Bula, U. Rechsteiner, S. Psoroulas, D. Weber, A. Lomax, and D. Meer. Real-time beam monitoring in scanned proton therapy. *Nuclear*

- Instruments and Methods in Physics Research Section A: Accelerators, Spectrometers, Detectors and Associated Equipment*, 891:62–67, 2018. ISSN 0168-9002. DOI 10.1016/j.nima.2018.02.107. (cited on pages 75, 76 and 82)
- A.-C. Knopf, D. Boye, A. Lomax, and S. Mori. Adequate margin definition for scanned particle therapy in the incidence of intrafractional motion. *Physics in Medicine and Biology*, 58(17):6079–6094, 2013. DOI 10.1088/0031-9155/58/17/6079. (cited on pages 6 and 90)
- A. Koehler, R. Schneider, and J. Sisterson. Flattening of proton dose distributions for large-field radiotherapy. *Medical Physics*, 4(4):297–301, 1977. DOI 10.1118/1.594317. (cited on pages 4 and 121)
- M. Krieger, G. Klimpki, G. Fattori, J. Hrbacek, D. Oxley, S. Safai, D. Weber, A. Lomax, and Z. Zhang. Experimental validation of a deforming grid 4D dose calculation for PBS proton therapy. *Physics in Medicine and Biology*, 63(5):055005–1–11, 2018. DOI 10.1088/1361-6560/aaad1e. (cited on pages 92, 94 and 96)
- C. Kwangzoo, H. Youngyih, K. Jinsung, A. Hwan, J. Gyu, J. Hoon, C. Yoonsun, C. Sungkoo, J. Kwanghyun, S. Hyuk, H. Chae-Seon, S. Suk, P. Seyjoon, K. Dae-Hyun, K. Young, L. Boram, S. Gantaro, N. Hideki, S. Kenzo, K. Yukio, C. Changhoon, H. Jae, A. Chan, P. Ryull, L. Hoon, P. Chul, P. Won, O. Ryul, N. Myung, Y. J. Il, S. Sanghyuk, L. Eun, L. Bomi, and C. Ho. The first private-hospital based proton therapy center in Korea; status of the Proton Therapy Center at Samsung Medical Center. *Radiation Oncology Journal*, 33(4):337–343, 2015. DOI 10.3857/roj.2015.33.4.337. (cited on page 87)
- A. La Rosa, M. Donetti, M. Borri, F. Rivero, A. Attili, F. Bourhaleb, R. Cirio, M. Garella, S. Giordanengo, N. Givehchi, G. Mazza, F. Marchetto, J. Pardo, A. Pecka, and C. Peroni. Characterization of a front-end electronics for the monitoring and control of hadrontherapy beams. *Nuclear Instruments and Methods in Physics Research Section A: Accelerators, Spectrometers, Detectors and Associated Equipment*, 586(2):270–275, 2008. ISSN 0168-9002. DOI 10.1016/j.nima.2007.12.012. (cited on pages 20 and 40)
- R. Leroy, N. Benahmed, F. Hulstaert, N. Van Damme, and D. De Ruyscher. Proton therapy in children: A systematic review of clinical effectiveness in 15 pediatric cancers. *International Journal of Radiation Oncology*Biophysics*Physics*, 95(1):267–278, 2016. ISSN 0360-3016. DOI 10.1016/j.ijrobp.2015.10.025. (cited on page 4)
- S. Lin, T. Boehringer, A. Coray, M. Grossmann, and E. Pedroni. More than 10 years experience of beam monitoring with the Gantry 1 spot scanning proton therapy facility at PSI. *Medical Physics*, 36(11):5331–5340, 2009. DOI 10.1118/1.3244034. (cited on pages 19, 40, 60 and 77)

Bibliography

- A. Lomax. Intensity modulation methods for proton radiotherapy. *Physics in Medicine and Biology*, 44(1):185–205, 1999. DOI 10.1088/0031-9155/44/1/014. (cited on pages 4 and 121)
- A. Lomax. Intensity modulated proton therapy and its sensitivity to treatment uncertainties 2: the potential effects of inter-fraction and inter-field motions. *Physics in Medicine and Biology*, 53(4):1043–1056, 2008. DOI 10.1088/0031-9155/53/4/015. (cited on page 5)
- A. Lomax. Towards daily adapted proton therapy. *Physica Medica*, 30:e3, 2014. ISSN 1120-1797. DOI 10.1016/j.ejmp.2014.07.017. (cited on page 6)
- A. Lomax, T. Bortfeld, G. Goitein, J. Debus, C. Dykstra, P.-A. Tercier, P. Coucke, and R. Mirimanoff. A treatment planning inter-comparison of proton and intensity modulated photon radiotherapy. *Radiotherapy and Oncology*, 51(3):257–271, 1999. ISSN 0167-8140. DOI 10.1016/S0167-8140(99)00036-5. (cited on page 4)
- T. LoSasso, C. Chui, G. Kutcher, S. Leibel, Z. Fuks, and C. Ling. The use of a multi-leaf collimator for conformal radiotherapy of carcinomas of the prostate and nasopharynx. *International Journal of Radiation Oncology*Biophysics*, 25(2):161–170, 1993. ISSN 0360-3016. DOI [https://doi.org/10.1016/0360-3016\(93\)90337-U](https://doi.org/10.1016/0360-3016(93)90337-U). (cited on page 120)
- A. Lourenço, D. Shipley, N. Wellock, R. Thomas, H. Bouchard, A. Kacperek, F. Fracchiolla, S. Lorentini, M. Schwarz, N. MacDougall, G. Royle, and H. Palmans. Evaluation of the water-equivalence of plastic materials in low- and high-energy clinical proton beams. *Physics in Medicine and Biology*, 62(10):3883–3901, 2017. DOI 10.1088/1361-6560/aa67d4. (cited on page 29)
- D. Low, W. Harms, S. Mutic, and J. Purdy. A technique for the quantitative evaluation of dose distributions. *Medical Physics*, 25(5):656–661, 1998. DOI 10.1118/1.598248. (cited on pages 32, 44 and 95)
- G. Mazza, R. Cirio, M. Donetti, A. L. Rosa, A. Luparia, F. Marchetto, and C. Peroni. A 64-channel wide dynamic range charge measurement ASIC for strip and pixel ionization detectors. *IEEE Transactions on Nuclear Science*, 52(4):847–853, 2005. DOI 10.1109/TNS.2005.852702. (cited on pages 20 and 40)
- D. Meer and S. Psoroulas. Gantries and dose delivery systems. *Modern Physics Letters A*, 30(17):1540021, 2015. DOI 10.1142/S0217732315400210. (cited on pages 35, 87 and 121)
- G. Meier, R. Besson, A. Nanz, S. Safai, and A. Lomax. Independent dose calculations for commissioning, quality assurance and dose reconstruction of PBS proton therapy. *Physics in Medicine and Biology*, 60(7):2819–2836, 2015. DOI 10.1088/0031-9155/60/7/2819. (cited on page 118)

- G. Meier, D. Leiser, R. Besson, A. Mayor, S. Safai, D. Weber, and A. Lomax. Contour scanning for penumbra improvement in pencil beam scanned proton therapy. *Physics in Medicine and Biology*, 62(6):2398–2416, 2017. DOI 10.1088/1361-6560/aa5dde. (cited on page 121)
- R. Miralbell, A. Lomax, L. Cella, and U. Schneider. Potential reduction of the incidence of radiation-induced second cancers by using proton beams in the treatment of pediatric tumors. *International Journal of Radiation Oncology*Biological*Physics*, 54(3):824–829, 2002. ISSN 0360-3016. DOI 10.1016/S0360-3016(02)02982-6. (cited on page 4)
- A. Monat, J. Averill, and R. Lazarus. Anticipatory stress and coping reactions under various conditions of uncertainty. *Journal of Personality and Social Psychology*, 24(2):237–253, 1972. DOI 10.1037/h0033297. (cited on page 1)
- S. Mori, J. Wolfgang, H.-M. Lu, R. Schneider, N. Choi, and G. Chen. Quantitative assessment of range fluctuations in charged particle lung irradiation. *International Journal of Radiation Oncology*Biological*Physics*, 70(1):253–261, 2008. ISSN 0360-3016. DOI 10.1016/j.ijrobp.2007.08.049. (cited on page 5)
- S. Mori, T. Inaniwa, T. Furukawa, W. Takahashi, M. Nakajima, T. Shirai, K. Noda, S. Yasuda, and N. Yamamoto. Amplitude-based gated phase-controlled rescanning in carbon-ion scanning beam treatment planning under irregular breathing conditions using lung and liver 4DCTs. *Journal of Radiation Research*, 55(5):948–958, 2014a. DOI 10.1093/jrr/rru032. (cited on pages 9 and 88)
- S. Mori, S. Zenklusen, T. Inaniwa, T. Furukawa, H. Imada, T. Shirai, K. Noda, and S. Yasuda. Conformity and robustness of gated rescanned carbon ion pencil beam scanning of liver tumors at NIRS. *Radiotherapy and Oncology*, 111(3):431–436, 2014b. ISSN 0167-8140. DOI 10.1016/j.radonc.2014.03.009. (cited on pages 9 and 88)
- MATLAB. *version 8.6.0 (R2015b)*. The MathWorks Inc., Natick, Massachusetts, 2015. URL <http://www.mathworks.com/products/matlab/>. (cited on pages 32 and 45)
- G. Nicolini, A. Fogliata, and L. Cozzi. IMRT with the sliding window: Comparison of the static and dynamic methods. Dosimetric and spectral analysis. *Radiotherapy and Oncology*, 75(1):112–119, 2005. ISSN 0167-8140. DOI 10.1016/j.radonc.2005.03.009. (cited on page 120)
- K. Ohara, T. Okumura, M. Akisada, T. Inada, T. Mori, H. Yokota, and M. Calaguas. Irradiation synchronized with respiration gate. *International Journal of Radiation Oncology*Biological*Physics*, 17(4):853–857, 1989. ISSN 0360-3016. DOI 10.1016/0360-3016(89)90078-3. (cited on page 7)

Bibliography

- D. Papp and J. Unkelbach. Direct leaf trajectory optimization for volumetric modulated arc therapy planning with sliding window delivery. *Medical Physics*, 41(1):011701–1–10, 2014. ISSN 2473-4209. DOI 10.1118/1.4835435. (cited on page 114)
- Particle Therapy Co-Operative Group. Statistics of patients treated in particle therapy facilities worldwide, 2016. URL <http://www.ptcog.ch/index.php/ptcog-patient-statistics>. (cited on page 4)
- E. Pedroni, R. Bacher, H. Blattmann, T. Böhringer, A. Coray, A. Lomax, S. Lin, G. Munkel, S. Scheib, U. Schneider, and A. Tourovsky. The 200-MeV proton therapy project at the Paul Scherrer Institute: Conceptual design and practical realization. *Medical Physics*, 22(1):37–53, 1995. DOI 10.1118/1.597522. (cited on pages 16, 21, 35, 57, 87 and 121)
- E. Pedroni, R. Bearpark, T. Böhringer, A. Coray, J. Duppich, S. Forss, D. George, M. Grossmann, G. Goitein, C. Hilbes, M. Jermann, S. Lin, A. Lomax, M. Negrazus, M. Schippers, and G. Kotrle. The PSI Gantry 2: A second generation proton scanning gantry. *Zeitschrift für medizinische Physik*, 14(1):25–34, 2004. DOI 10.1078/0939-3889-00194. (cited on page 11)
- E. Pedroni, S. Scheib, T. Böhringer, A. Coray, M. Grossmann, S. Lin, and A. Lomax. Experimental characterization and physical modelling of the dose distribution of scanned proton pencil beams. *Physics in Medicine and Biology*, 50(3):541–561, 2005. DOI 10.1088/0031-9155/50/3/011. (cited on pages 32, 77 and 94)
- E. Pedroni, D. Meer, C. Bula, S. Safai, and S. Zenklusen. Pencil beam characteristics of the next-generation proton scanning gantry of PSI: Design issues and initial commissioning results. *The European Physical Journal Plus*, 126(7):66, 2011. DOI 10.1140/epjp/i2011-11066-0. (cited on pages 11, 16, 17, 35, 57, 58, 75, 112 and 121)
- J. Perl, J. Shin, J. Schümann, B. Faddegon, and H. Paganetti. TOPAS: An innovative proton Monte Carlo platform for research and clinical applications. *Medical Physics*, 39(11):6818–6837, 2012. ISSN 2473-4209. DOI 10.1118/1.4758060. (cited on page 77)
- M. Phillips, E. Pedroni, H. Blattmann, T. Böhringer, A. Coray, and S. Scheib. Effects of respiratory motion on dose uniformity with a charged particle scanning method. *Physics in Medicine and Biology*, 37(1):223–234, 1992. DOI 10.1088/0031-9155/37/1/016. (cited on pages 5, 8, 35 and 87)
- S. Psoroulas, P. Fernandez, G. Klimpki, C. Bula, D. Meer, and D. Weber. Challenges in fast beam current control inside the cyclotron for fast beam delivery in proton therapy. In *Proceedings of CYCLOTRONS 2016, Zurich, Switzerland*, pages 1–4, 2016a. DOI 10.18429/JACoW-Cyclotrons2016-TUA02. (cited on page 17)

- S. Psoroulas, G. Klimpki, P. F. Carmona, C. Bula, D. Weber, and D. Meer. P116: Feasibility study of IMPT-like delivery with continuous line scanning of protons. In I. J. of Particle Therapy, editor, *Proceedings to the 55th Annual Meeting for the Particle Therapy Cooperative Group (PTCOG)*, volume 3, pages 164–165, 2016b. DOI doi.org/10.14338/IJPT.16-PTCOG-1.1. (cited on page 2)
- T. Renner, W. Chu, B. Ludewigt, J. Halliwell, M. Nyman, R. Singh, G. Stover, and R. Stradtner. Preliminary results of a raster scanning beam delivery system. In *Particle Accelerator Conference, 1989. Accelerator Science and Technology. Proceedings of the 1989 IEEE*, volume 1, pages 672–674, 1989. DOI 10.1109/PAC.1989.73218. (cited on pages 4 and 121)
- M. Riboldi, R. Orecchia, and G. Baroni. Real-time tumour tracking in particle therapy: technological developments and future perspectives. *The Lancet Oncology*, 13(9):e383–e391, 2012. ISSN 1470-2045. DOI 10.1016/S1470-2045(12)70243-7. (cited on pages 8 and 87)
- E. Rietzel and C. Bert. Respiratory motion management in particle therapy. *Medical Physics*, 37(2):449–460, 2010. ISSN 2473-4209. DOI 10.1118/1.3250856. (cited on page 9)
- E. Rietzel, G. Chen, N. Choi, and C. Willet. Four-dimensional image-based treatment planning: Target volume segmentation and dose calculation in the presence of respiratory motion. *International Journal of Radiation Oncology*Biophysics*, 61(5):1535–1550, 2005. ISSN 0360-3016. DOI 10.1016/j.ijrobp.2004.11.037. (cited on page 8)
- V. Rizzoglio, A. Adelman, C. Baumgarten, M. Frey, A. Gerbershagen, D. Meer, and J. Schippers. Evolution of a beam dynamics model for the transport line in a proton therapy facility. *Phys. Rev. Accel. Beams*, 20:124702–1–12, 2017. DOI 10.1103/PhysRevAccelBeams.20.124702. (cited on page 112)
- Y. Rottenstreich and C. Hsee. Money, kisses, and electric shocks: on the affective psychology of risk. *Psychological Science*, 12(3):185–190, 2001. DOI 10.1111/1467-9280.00334. (cited on page 1)
- S. Safai, C. Bula, D. Meer, and E. Pedroni. Improving the precision and performance of proton pencil beam scanning. *Translational Cancer Research*, 1(3):196–206, 2012. ISSN 2218-676X. DOI 10.3978/j.issn.2218-676X.2012.10.08. (cited on pages 11, 16, 35, 57 and 75)
- D. Scandurra, F. Albertini, R. van der Meer, G. Meier, D. Weber, A. Bolsi, and A. Lomax. Assessing the quality of proton PBS treatment delivery using machine log files: Comprehensive analysis of clinical treatments delivered at PSI Gantry 2. *Physics in Medicine and Biology*, 61(3):1171–1181, 2016. DOI 10.1088/0031-9155/61/3/1171. (cited on pages 48 and 118)

Bibliography

- A. Schätti, M. Zakova, D. Meer, and A. Lomax. Experimental verification of motion mitigation of discrete proton spot scanning by re-scanning. *Physics in Medicine and Biology*, 58(23):8555–8572, 2013. DOI 10.1088/0031-9155/58/23/8555. (cited on pages 9, 15, 27, 45, 87, 88, 94, 101, 102, 110 and 111)
- A. Schätti, D. Meer, and A. Lomax. First experimental results of motion mitigation by continuous line scanning of protons. *Physics in Medicine and Biology*, 59(19):5707–5723, 2014. DOI 10.1088/0031-9155/59/19/5707. (cited on pages 2, 9, 10, 11, 88, 101, 110 and 121)
- J. Schippers, R. Dölling, J. Duppich, G. Goitein, M. Jermann, A. Mezger, E. Pedroni, H. Reist, and V. Vrankovic. The SC cyclotron and beam lines of PSI’s new protontherapy facility PROSCAN. *Nuclear Instruments and Methods in Physics Research Section B: Beam Interactions with Materials and Atoms*, 261(1–2):773–776, 2007a. ISSN 0168-583X. DOI 10.1016/j.nimb.2007.04.052. (cited on pages 17, 58 and 75)
- J. Schippers, D. Meer, and E. Pedroni. Fast scanning techniques for cancer therapy with hadrons: A domain of cyclotrons. In *Proceedings of CYCLOTRONS 2010, Lanzhou, China*, pages 410–415, 2010. URL <https://accelconf.web.cern.ch/accelconf/Cyclotrons2010/papers/frm1cio04.pdf>. (cited on page 117)
- M. Schippers, D. Anicic, R. Dölling, A. Mezger, E. Pedroni, and L. Stamsnijder. Beam intensity stability of a 250 MeV SC cyclotron equipped with an internal cold-cathode ion source. In *Proceedings of CYCLOTRONS 2007, Giardini-Naxos, Italy*, pages 300–302, 2007b. URL <http://accelconf.web.cern.ch/AccelConf/c07/PAPERS/300.PDF>. (cited on page 17)
- C. Schneider, W. Rasband, and K. Eliceiri. NIH Image to ImageJ: 25 years of image analysis. *Nature Methods*, 9(7):671–675, 2012. ISSN 1548-7091. DOI 10.1038/nmeth.2089. (cited on page 45)
- E. Schneider, B. Streicher, E. Lermer, R. Sachs, and D. Frey. Measuring the zero-risk bias. *Zeitschrift für Psychologie*, 225(1):31–44, 2017. DOI 10.1027/2151-2604/a000284. (cited on page 1)
- J. Seco, P. Evans, and S. Webb. Analysis of the effects of the delivery technique on an IMRT plan: comparison for multiple static field, dynamic and NOMOS MIMiC collimation. *Physics in Medicine and Biology*, 46(12):3073–3087, 2001. DOI 10.1088/0031-9155/46/12/301. (cited on page 120)
- J. Seco, D. Robertson, A. Trofimov, and H. Paganetti. Breathing interplay effects during proton beam scanning: Simulation and statistical analysis. *Physics in Medicine and Biology*, 54(14):N283–N294, 2009. DOI 10.1088/0031-9155/54/14/N01. (cited on pages 5, 102 and 111)

- P. Slovic. Perception of risk. *Science*, 236:280–285, 1987. DOI 10.1126/science.3563507. (cited on page 1)
- A. Smith, M. Gillin, M. Bues, X. Zhu, K. Suzuki, R. Mohan, S. Woo, A. Lee, R. Komaki, J. Cox, K. Hiramoto, H. Akiyama, T. Ishida, T. Sasak, and K. Matsuda. The M. D. Anderson proton therapy system. *Medical Physics*, 36(9):4068–4083, 2009. DOI 10.1118/1.3187229. (cited on pages 50, 83, 87 and 109)
- M. Stenecker, A. Lomax, and U. Schneider. Intensity modulated photon and proton therapy for the treatment of head and neck tumors. *Radiotherapy and Oncology*, 80(2):263–267, 2006. ISSN 0167-8140. DOI 10.1016/j.radonc.2006.07.025. (cited on page 4)
- R. Suter, T. Pachur, and R. Hertwig. How affect shapes risky choice: Distorted probability weighting versus probability neglect. *Journal of Behavioral Decision Making*, 29(4):437–449, 2016. ISSN 1099-0771. DOI 10.1002/bdm.1888. (cited on page 1)
- A. Trofimov and T. Bortfeld. Beam delivery sequencing for intensity modulated proton therapy. *Physics in Medicine and Biology*, 48(10):1321–1331, 2003. DOI 10.1088/0031-9155/48/10/306. (cited on page 41)
- J. Unkelbach, T. Bortfeld, B. Martin, and M. Soukup. Reducing the sensitivity of IMPT treatment plans to setup errors and range uncertainties via probabilistic treatment planning. *Medical Physics*, 36(1):149–163, 2009. ISSN 2473-4209. DOI 10.1118/1.3021139. (cited on page 6)
- J. Unkelbach, T. Bortfeld, D. Craft, M. Alber, M. Bangert, R. Bokrantz, D. Chen, R. Li, L. Xing, C. Men, S. Nill, D. Papp, E. Romeijn, and E. Salari. Optimization approaches to volumetric modulated arc therapy planning. *Medical Physics*, 42(3):1367–1377, 2015. ISSN 2473-4209. DOI 10.1118/1.4908224. (cited on pages 114 and 121)
- M. Urie and M. Goitein. Variable versus fixed modulation of proton beams for treatments in the cranium. *Medical Physics*, 16(4):593–601, 1989. ISSN 2473-4209. DOI 10.1118/1.596428. (cited on page 4)
- S. Vijayakumar and G. Chen. Implementation of three dimensional conformal radiation therapy: Prospects, opportunities, and challenges. *International Journal of Radiation Oncology*Biophysics*Physics*, 33(5):979–983, 1995. ISSN 0360-3016. DOI 10.1016/0360-3016(95)02060-8. (cited on page 120)
- W. Viscusi, W. Magat, and J. Huber. An investigation of the rationality of consumer valuation of multiple health risks. *The RAND Journal of Economics*, 18(4):465–479, 1987. ISSN 07416261. URL <http://www.jstor.org/stable/2555636>. (cited on page 1)

Bibliography

- S. Webb. Optimisation of conformal radiotherapy dose distribution by simulated annealing. *Physics in Medicine and Biology*, 34(10):1349–1370, 1989. DOI 10.1088/0031-9155/34/10/002. (cited on page 120)
- C. Yu. Intensity-modulated arc therapy with dynamic multileaf collimation: an alternative to tomotherapy. *Physics in Medicine and Biology*, 40(9):1435–1449, 1995. DOI 10.1088/0031-9155/40/9/004. (cited on page 120)
- S. Zenklusen, E. Pedroni, and D. Meer. A study on repainting strategies for treating moderately moving targets with proton pencil beam scanning at the new Gantry 2 at PSI. *Physics in Medicine and Biology*, 55(17):5103–5121, 2010. DOI 10.1088/0031-9155/55/17/014. (cited on pages 2, 9, 11, 16, 21, 35, 57, 75, 87, 88 and 101)
- Y. Zhang, D. Boye, C. Tanner, A. Lomax, and A. Knopf. Respiratory liver motion estimation and its effect on scanned proton beam therapy. *Physics in Medicine and Biology*, 57(7):1779–1795, 2012. DOI 10.1088/0031-9155/57/7/1779. (cited on pages 5, 9 and 88)
- Y. Zhang, I. Huth, M. Wegner, D. Weber, and A. Lomax. An evaluation of rescanning technique for liver tumour treatments using a commercial PBS proton therapy system. *Radiotherapy and Oncology*, 121(2):281–287, 2016. ISSN 0167-8140. DOI 10.1016/j.radonc.2016.09.011. (cited on pages 9, 89, 101, 102, 110 and 111)

Curriculum vitae

Grischa Klimpki

born on May 28, 1989
in Hamburg, Germany
citizen of Germany

<https://orcid.org/0000-0001-7646-6200>

Education

2008 Abitur at the Gymnasium Neu Wulmstorf, Germany
2009 – 2012 B.Sc. in Physics at the University of Heidelberg, Germany
2012 – 2014 M.Sc. in Physics at the University of Heidelberg, Germany
since 2014 Ph.D. in Physics at ETH Zurich, Switzerland

Talks

03/2014 Annual spring meeting of the DPG in Mainz, Germany
06/2014 53rd scientific meeting of the PTCOG in Shanghai, China
09/2014 8th European Conference on Medical Physics in Athens, Greece
02/2016 ICTR-PHE in Geneva, Switzerland
02/2017 EuCARD² workshop in Torino, Italy
10/2017 16th ICALEPCS in Barcelona, Spain

Publications

09/2013 Klimpki et al. *Radiat. Meas.* **56** 342–346
01/2016 Klimpki et al. *Med. Phys. Biol.* **61** 1021–1040
07/2017 Klimpki et al. *Med. Phys. Biol.* **62** 6126–6143
02/2018 Klimpki et al. *Nucl. Instrum. Meth. A* **891** 62–67

